AD-A068 594 MCDONNELL AIRCRAFT CO ST LOUIS MO F/G 17/5
INFRARED NON-LINEAR LENS.(U)
DEC 78 R W FISHER, R D HELMICK, R A KUPFERER F33615-77-C-1113
UNCLASSIFIED AFAL-TR-78-204 NL

LEVEL II

AFAL-TR-78-204

INFRARED NON-LINEAR LENS

Prepared by
R.W. Fisher, R. Holmick, R.A. Kupferer

McDonnell Aircraft Company
McDonnell Douglas Corporation
P.O. Box 516
St. Louis, Missouri 63166

TECHNICAL REPORT AFAL-TR-78-204
December 1978

Contract F33615-77-C-1113
Final Report FOR PERIOD - OCTOBER 1977 - AUGUST 1978

AIR FORCE AVIONICS LABORATORY
AIR FORCE WRIGHT AERONAUTICAL LABORATORIES
AIR FORCE SYSTEMS COMMAND
WRIGHT-PATTERSON AIR FORCE BASE

NOTICE

When Government drawings, specifications, or other data are used for any purpose other than in connection with a definitely related Government procurement operation, the United States Government thereby incurs no responsibility nor any obligation whatsoever; and the fact that the government may have formulated, furnished, or in any way supplied the said drawings, specifications, or other data, is not to be regarded by implication or otherwise as in any manner licensing the holder or any other person or corporation, or conveying any rights or permission to manufacture, use, or sell any patented invention that may in any way be related thereto.

This technical report has been reviewed and is approved for publication.

WILLIAM R. PERSHING, Proj Engr
Electro-Optical Sensor Science
and Engineering Group

HAROLD E. GELTMACHER, Chief
EO Sen Science & Engring Group
Electro-Optics & Recon Branch

FOR THE COMMANDER:

GALE D. URBAN, Chief
EO & Reconnaissance Branch
Recon & Weapon Delivery Division

"If your address has changed, if you wish to be removed from our mailing list, or if the addressee is no longer employed by your organization please notify AFAL/RWI-3 ,W-P AFB, OH 45433 to help us maintain a current mailing list".

Copies of this report should not be returned unless return is required by security considerations, contractual obligations, or notice on a specific document.

AIR FORCE/56780/1 May 1979 — 100

UNCLASSIFIED

SECURITY CLASSIFICATION OF THIS PAGE (When Data Entered)

REPORT DOCUMENTATION PAGE

READ INSTRUCTIONS BEFORE COMPLETING FORM

1. REPORT NUMBER: AFAL-TR-78-204	2. GOVT ACCESSION NO.
3. RECIPIENT'S CATALOG NUMBER	
4. TITLE (and Subtitle): INFRARED NON-LINEAR LENS	5. TYPE OF REPORT & PERIOD COVERED: Final Report Oct 1977 - August 1978
6. PERFORMING ORG. REPORT NUMBER	
7. AUTHOR(s): Ralph W. Fisher, Roger D. Helmick, Richard A. Kupferer	8. CONTRACT OR GRANT NUMBER(s): F33615-77-C-1113
9. PERFORMING ORGANIZATION NAME AND ADDRESS: McDonnell Aircraft Company, McDonnell Douglas Corporation, P.O. Box 516, St. Louis, MO 63166	10. PROGRAM ELEMENT, PROJECT, TASK AREA & WORK UNIT NUMBERS: 2004 76-32
11. CONTROLLING OFFICE NAME AND ADDRESS: Air Force Avionics Laboratory (RWI), Air Force Systems Command, United States AF, WPAFB, OH 45433	12. REPORT DATE: December 1978 13. NUMBER OF PAGES: 96
14. MONITORING AGENCY NAME & ADDRESS (if different from Controlling Office)	15. SECURITY CLASS. (of this report): Unclassified 15a. DECLASSIFICATION/DOWNGRADING SCHEDULE

16. DISTRIBUTION STATEMENT (of this Report)

Approved for public release; distribution unlimited.

17. DISTRIBUTION STATEMENT (of the abstract entered in Block 20, if different from Report)

18. SUPPLEMENTARY NOTES

19. KEY WORDS (Continue on reverse side if necessary and identify by block number)

Variable Acuity	Displays	Optical Detection
Optics	Remote Sensing	Infrared Detection
Vision	Television System	

20. ABSTRACT (Continue on reverse side if necessary and identify by block number)

A dynamic target acquisition analytic model for a Variable Acuity Remote Viewing System (VARVS) was developed and experimentally verified. The model was then used to compute target acquisition capability of an infrared version of the VARVS and conventional linear FLIR's with various fields of view. Results indicated that the VARVS, as presently configured, has a target acquisition effectiveness of about 80% of the best linear sensor. The study indicated VARVS performance could be improved by broadening the high acuity central → next page

DD FORM 1 JAN 73 1473

UNCLASSIFIED

SECURITY CLASSIFICATION OF THIS PAGE (When Data Entered)

20. Abstract - Continued

cont→

portion of the distortion function or by reducing slew time, However, it never exceeds the performance of the linear sensor with the proper field of view. While it can be concluded that the VARVS concept offers no improvement over conventional linear sensor, the limitations of the theory and experiment must be recognized. They represent acquisition of a fixed target from a stable platform. If the vehicle is maneuvering or if cues such as motion or glints exist, the wide field of the VARVS may play an important role in supporting the cognitive factors that are little understood in target acquisition. Secondary objectives were to determine the feasibility of a common aperture narrow field high resolution capability for the sensor. The design effort could not achieve the required performance over the 2 degree narrow field of view. However, no technical constraints could be identified which make such a design not feasible.

FOREWORD

This is the final report of contract F33615-77-C-1113. The primary objectives of this effort were to establish the effectiveness of a Variable Acuity Remote Viewing System (VARVS) for reconnaissance and weapons delivery applications. Secondary objectives were to establish optimum parameters for the VARVS and determine the feasibility of adding a common aperture narrow field high resolution capability to the sensor.

The contributions, expert technical guidance, and suggestions of Mr. William R. Pershing, Project Engineer are gratefully acknowledged. His understanding and aid alleviated many of the problems encountered during this study. The technical contribution of Mr. George Licis and Mr. Bernard Weber for the design and construction of the laboratory equipment are especially acknowledged. Special thanks also goes to Mr. Alfred Rosenfeld for his valuable comments and editing of the technical data and of this text.

TABLE OF CONTENTS

LIST OF ILLUSTRATIONS

LIST OF ILLUSTRATIONS - (Continued)

LIST OF ILLUSTRATIONS - (Continued)

SECTION I

INTRODUCTION AND SUMMARY

The objective of this effort was to document the performance capabilities of an Infrared Variable Acuity Remote Viewing System (VARVS) and to optimize its parameters. In addition, the feasibility of adding a common aperture narrow field-of-view, high resolution optical system to the wide angle VARVS was to be determined.

This turned out to be a far more ambitious program than we originally anticipated. An entirely new observer dynamic model had to be developed because no existing model could properly handle the large field-of-view of the VARVS system. The next difficulty arose when we decided that the only meaningful way to present VARVS capabilities was on a comparative basis with conventional linear sensors. This required that we develop a model for the linear sensor along lines identical to the VARVS, so common inputs/outputs, etc. would exist. This in turn required that we validate both models experimentally. When we considered that a minimum of three fields-of-view are required to validate the linear sensor model and the one field-of-view of the VARVS, the experimental effort expanded by a factor of four. Fortunately much of the extra experimental work was able to make use of test facilities developed for validation of electro-optic sensor models that were part of an on-going Independent Research and Development (IRAD) effort. As a result, the contract objectives were met within available funding levels, but a slip in schedule necessarily occurred.

The results of this study were somewhat negative. The Infrared VARVS target detection performance was found to be at best only 80% as effective as the conventional linear sensor. The limiting factor is the VARVS slew time. It becomes dominant because its optical axis must be slewed for each cue before the acuity is sufficient for target detection. Conversely, the linear sensor's uniform resolution supports search and detection throughout its field-of-view. The major portion of visual search can then be accomplished by visual glimpses with sensor slewing only occassionally dictated by lateral coverage requirements. VARVS performance can be improved either by reducing its slew time and including control by eye position or by increasing its region of high acuity. The latter approach results in continual improvement until the entire field is uniform where it then becomes a linear sensor with about 20° field-of-view.

An obvious question at this point is, "Why use the VARVS when a linear sensor works better?". For target acquisition this is clearly the case. It was shown both experimentally and theoretically in this effort. Why then is VARVS display so appealing when viewing real world scenes? This is especially true when video tapes made in flight are viewed but also exists to a lesser degree when viewing from a laboratory rooftop. The answers probably lie in the cognitive factors involved in the visual process that are not defined or well understood. These include peripheral cueing due to motion or glints. Others may be the instantaneous recognition of relative vehicle, sensor, real world orientation that is possible with a wide field display. This may be especially valuable when the vehicle is maneuvering and/or flight control and navigation must be performed simultaneously with target acquisition. We believe therefore, that neither the theory or experiment show the true value of the VARVS. It is becoming increasingly clear that only a flight evaluation can prove or disapprove the value of the VARVS.

One significant technical output of this contract is the new observer dynamic model. This model synthesizes human vision much more accurately than existing models. The primary difference is shown in Figure 1. This new model when applied to conventional sensors can be used to properly evaluate advanced wide angle display concepts whereas the existing models are only verified for 10° to 20° display angles.

The feasibility of a dual field VARVS could not be positively established during this study. However, results were encouraging enough that we intend to continue this effort independently.

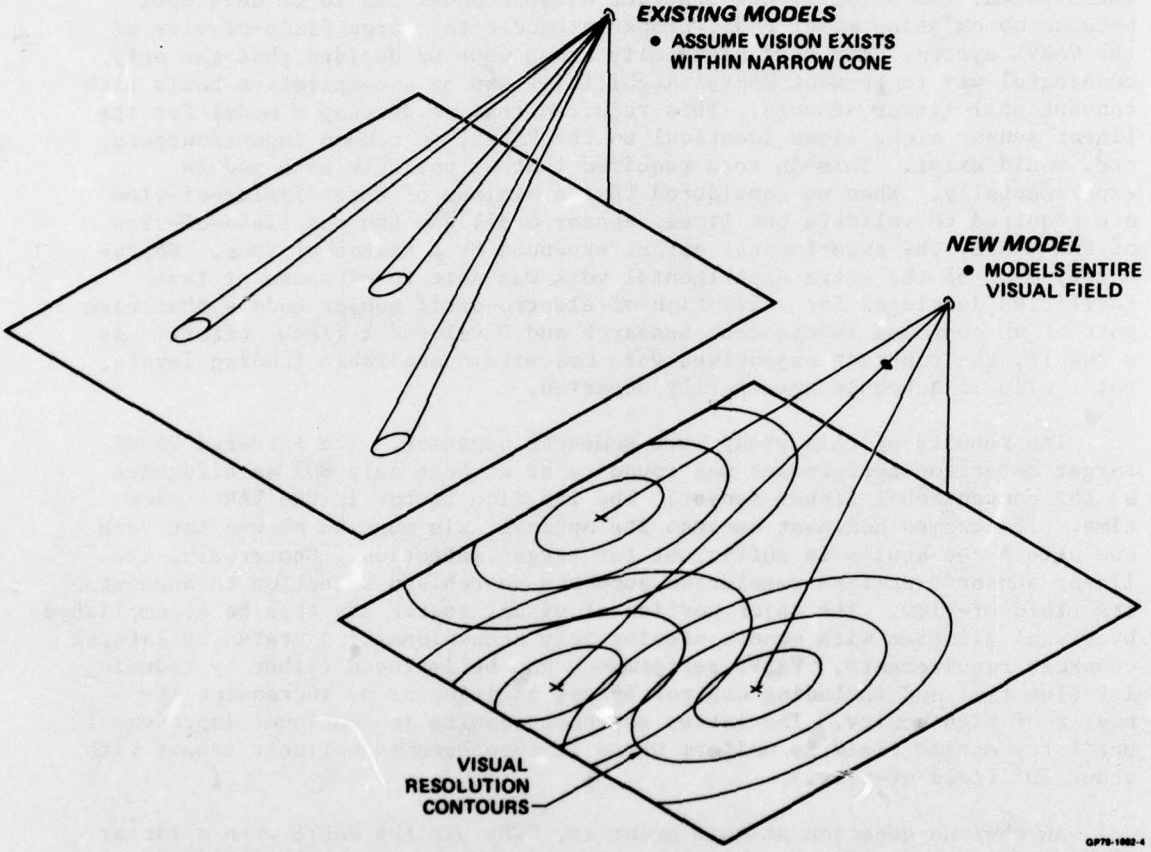

Figure 1 Visual model rationale

SECTION II

APPROACH

The study was divided into two phases. The primary objective of Phase I was to develop an experimentally validated analytic model of the VARVS concept and to use this model to predict target acquisition performance of an infrared VARVS. The secondary objective was to determine the amount of variation that could be made in the VARVS design parameters that would yield improved performance. In Phase II, the feasibility of the improved VARVS was to be established. As the study progressed, it became clear that the VARVS model development, its experimental validation, and its application to the IR VARVS would occupy most of the effort. This occurred because all existing sensor dynamic models were not useable with the VARVS because they are developed around linear sensor and display geometries. Furthermore, to avoid the pitfalls of predicting absolute performance of the VARVS, we elected to show performance relative to a conventional linear sensor. This required a parallel development of a linear sensor model based on the same philosophy as the VARVS model so that it would employ the same inputs and outputs. This linear model has been developed and experimentally validated under a related IRAD effort, see Reference 1, and could be used for this purpose.

The actual approach used for Phase I is shown in Figure 2. As shown on the figure, the study began with an effort to improve the VARVS static model, using as a base, the experience gained during the development of the Office of Naval Research (ONR) brassboard system. More specifically, the acuity function and optical quality inputs to the VARVS model were updated to reflect actual performance of the ONR brassboard equipment that was to be used for the validation experiment. The major effort was directed to the inclusion of the human observer performance to create the dynamic model for the VARVS. This effort is described in detail in Section III. In parallel with this task but funded by a related IRAD, was the development of a conventional sensor model along identical lines. The design of the experimental equipment was also accomplished at this point in the study which consisted of a treadmill and drive system to simulate relative forward vehicle motion. Details of this development are also discussed in Section III. The next step, the analytic model validation, was accomplished by inputting a set of flight conditions into the model and comparing the predicted performance with actual results from the experiment for the same simulated flight conditions. Correlation of theory and experiment led to several iterations of the theoretical model before agreement was achieved.

For the parametric analyses discussed in Section IV, both conventional and VARVS models were shifted to the 8-14μ infrared spectrum so that performance on an Infrared VARVS (IR VARVS) could be compared directly to a FLIR with conventional optics. Both IR VARVS and FLIR performance were computed as functions of the mission parameters of altitude, velocity, minimum acquisition range (for weapon delivery considerations), and lateral coverage. In addition, the effect of the IR VARVS slew time and FLIR field-of-view performance were determined. Slew time was included because it has the greatest effect of any parameter on the VARVS performance. A separate offshoot of this parametric analysis was a study of the internal structure of the VARVS model to see if an alternate distortion function would yield better

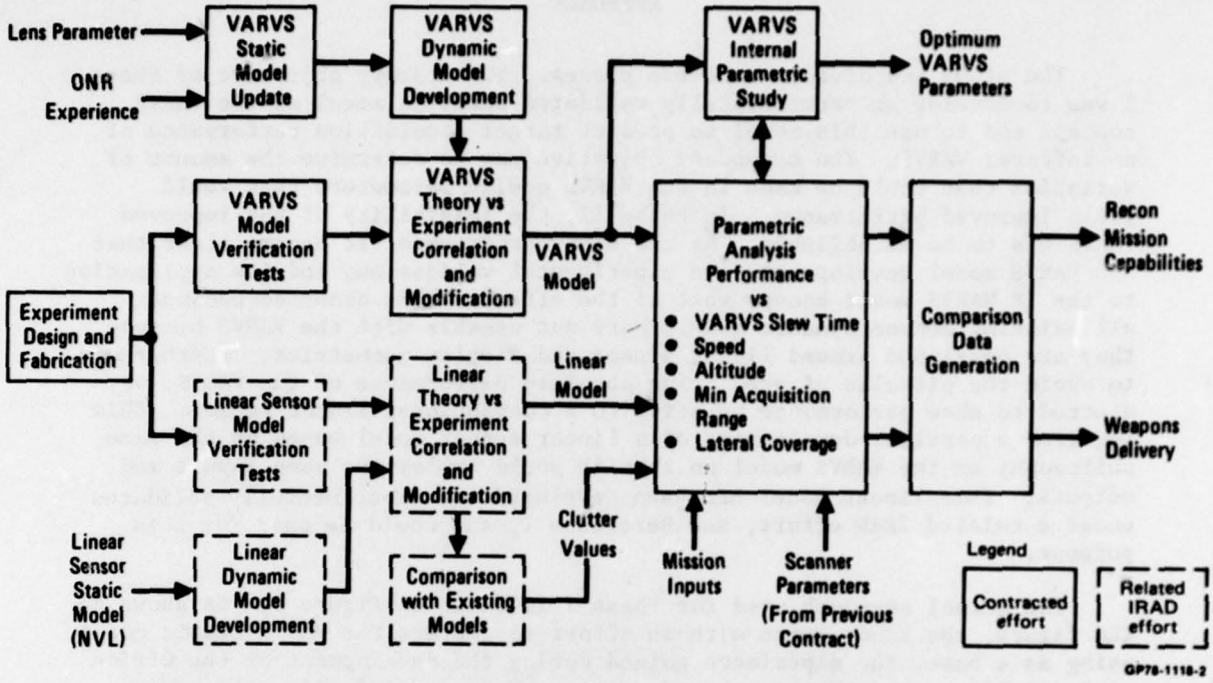

Figure 2 Phase I approach

performance. This study is discussed in Section V while details of the IR VARVS/FLIR parametric study are presented in Section IV.

Rationale' used for performance comparisons of the IR VARVS to FLIR is shown in Figure 3. First, the probability of target detection was computed and plotted as a function of offset for all parameter combinations. Next, the lateral coverage where the probability of detection (P_d) is 90% was read from each curve. From this point, the approach depends upon the type of mission. For a reconnaissance mission, the 90% P_d lateral coverage was plotted as a function of depression angle for each parameter set. For weapon delivery, the 90% P_d lateral coverage was plotted against the minimum range boundary of the downrange search area. For reconnaissance, the maximum lateral coverage was selected from each curve. A ratio was then computed of IR VARVS and 10°, 20°, and 40° field-of-view FLIR lateral coverage for identical parameter sets. These data were plotted against the remaining parameters which are VARVS slew time, clutter factor, altitude, and velocity. This technique of presentation was selected to show instantly the relative performance of sensor types and sensitivities to design and mission parameters. Similar curves were plotted for weapons delivery except in this case the product of lateral coverage at maximum acquisition range times maximum acquisition range was plotted as the dependent variable.

Originally, we intended to plot the ratio of IR VARVS to FLIR maximum acquisition ranges for a specific lateral coverage as a figure of merit. This proved to be uninformative because the ratios were simply those imposed by the resolution limits of the sensors until the lateral coverage caused a dynamic search limitation which then caused the ratio to drop abruptly to zero. For these reasons, the range lateral coverage product was selected as an independent variable for weapons delivery plots.

In Phase II the feasibility of an improved IR VARVS is considered by showing how an on-axis target recognition capability can be added to the VARVS. Details are presented in Section VI.

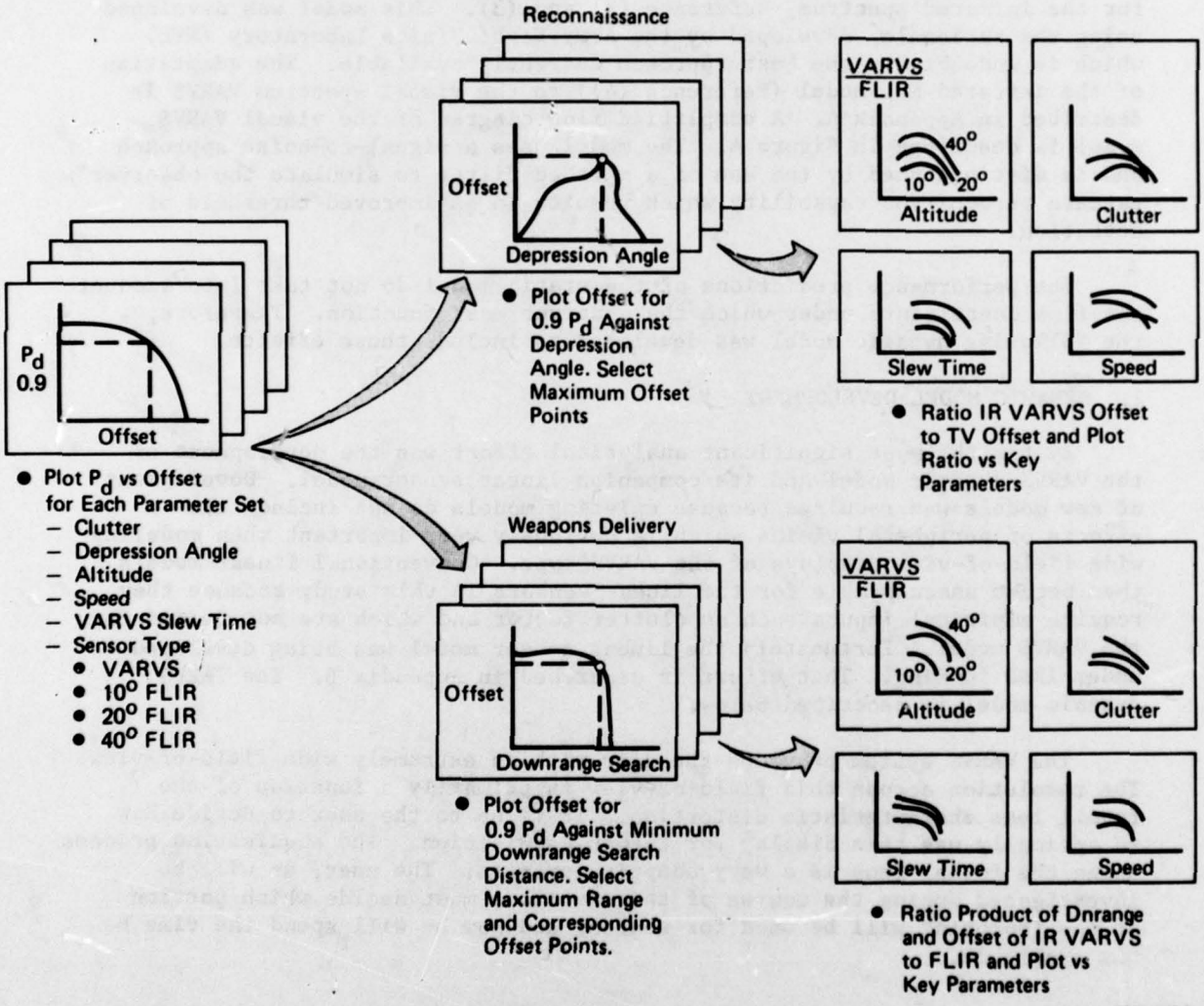

Figure 3 Performance comparison rationale

SECTION III

ANALYTIC MODEL DEVELOPMENT AND VALIDATION

In this section the development of the analytic models is described and their experimental validation is presented. Since validation will be accomplished with the ONR brassboard equipment, the model is first developed for visual spectrum operation. Its conversion to the infrared is described in Section IV.

1. STATIC MODEL DEVELOPMENT

A static model for the VARVS has been developed in previous efforts for the infrared spectrum, Reference (2) and (3). This model was developed using the rationale developed by the Army Night Vision Laboratory (NVL) which is undoubtedly the best approach currently available. The adaptation of the infrared NVL model (Reference (4)) to the visual spectrum VARVS is described in Appendix A. A simplified flow diagram of the visual VARVS model is described in Figure 4. The model uses a signal-to-noise approach and is distinguished by the use of a matched filter to simulate the observer's pattern recognition capability which results in an improved threshold of detection.

The performance predictions of the static model do not take into account the time constraints under which the observer must function. Therefore, the following dynamic model was developed to include these effects.

2. DYNAMIC MODEL DEVELOPMENT

By far the most significant analytical effort was the development of the VARVS dynamic model and its companion linear sensor model. Development of new models was required because existing models do not include the effects of peripheral vision which is obviously very important when modeling wide field-of-view displays of the VARVS type. Conventional linear models then become unacceptable for the linear sensors in this study because they require empirical inputs such as clutter factor and which are not needed for the VARVS model. Fortunately the linear sensor model was being developed under IRAD funding. That effort is described in Appendix B. The VARVS dynamic model is described below.

The VARVS system provides the user with an extremely wide field-of-view. The resolution across this field-of-view is primarily a function of the foveal lens characteristic distortion. It is up to the user to decide how to optimally use this display for target acquisition. The acquisition process using the foveal lens is a very adaptive process. The user, as will be investigated during the course of this section, must decide which portion of the footprint will be used for search, and how he will spend the time he has available.

The following is a description of the VARVS target acquisition model. The first part is concerned with a general description of the VARVS ground coverage and how its characteristics affect the way it is used. The second part describes the exponential equations used to define the condit-

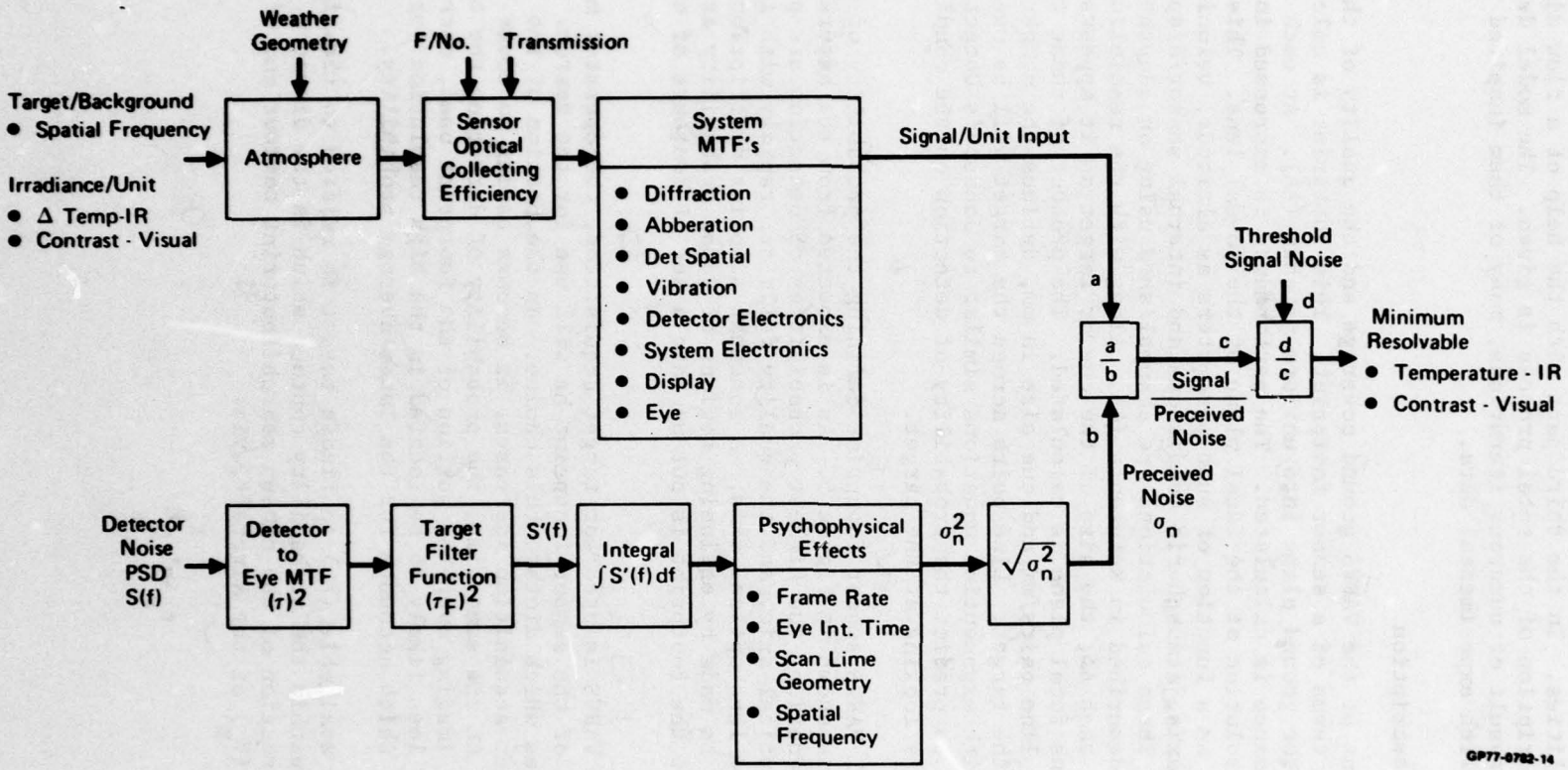

Figure 4 Static performance model

ional probabilities. In the third part with the help of a flow diagram, a general description of the total process is given. The model described below is the result of numerous iterations, many of them inspired by lack of agreement with experimental data.

a. General Description

The extent of the VARVS ground coverage and the quality of the coverage is defined in terms of a sensor footprint. This footprint is calculated by partitioning the ground plane into uniform patches (ΔA). At each ΔA, sensor performance is calculated. The performance is expressed in terms of spatial resolution at the focal plane of the foveal lens. This resolution is calculated as a function of such parameters as altitude, velocity, angle from optical axis, atmospheric conditions and internal sensor/display characteristics. These calculations are accomplished using an adaptation of the NVL model as described in Reference (4). Along with the resolution calculations made at each ΔA, the size of the cue or target as it appears on the non-linear lens focal plane is calculated. The product of these two terms, resolution in line pairs/mm and cue size in mm, defines the number of line pairs across the target. Line pairs across the target will be used in conjunction with exponential equations similar to Johnson's Detection Criteria, Reference (5) to predict the probability of detection on the condition that the observer is looking at the target.

A typical VARVS sensor footprint defining the probability of detecting a 60 ft. cue is shown in Figure 5. As is expected from the nature of the lens acuity function, the highest probabilities of detection are present on or near the optical axis, and the quality falls off rapidly with increasing angle from the lens optical axis. A somewhat simplier description of the footprint can be made by enclosing regions of equal probability as shown in Figure 6 where the footprint is cut up into a set of contours of equal probability.

When the VARVS is used for target acquisition, the operator must pick which portion of the sensor footprint he will use for the search. There are two main forces which dictate this choice. As the portion of the footprint used for target acquisition increases, it becomes easier to cover the total search area. At the same time, the probability of detecting the target determined by imaging over the portion of the footprint used, decreases. The target is less likely to be located in the high resolution portion of the footprint which accounts for the lower average probability.

The time available (t_a) to find a target is related to the time a target stays within the probability contour which is the distance (X_p) along the flight direction of the chosen search footprint contour and divided by the velocity (V_x) of the aircraft, viz:

$$t_a = \frac{X_p}{V_x} \qquad (1)$$

Centerline
(Optical Axis)

0.00	0.00	0.00	0.00	0.00	0.08	0.00	0.00	0.00	0.00	0.00
0.00	0.00	0.00	0.00	0.09	0.10	0.09	0.00	0.00	0.00	0.00
0.00	0.00	0.00	0.09	0.11	0.12	0.11	0.09	0.00	0.00	0.00
0.00	0.00	0.09	0.11	0.13	0.14	0.13	0.11	0.09	0.00	0.00
0.00	0.08	0.10	0.13	0.16	0.17	0.16	0.13	0.10	0.08	0.00
0.00	0.09	0.12	0.15	0.19	0.20	0.19	0.15	0.12	0.09	0.00
0.00	0.09	0.14	0.18	0.22	0.24	0.22	0.18	0.14	0.09	0.00
0.00	0.09	0.17	0.21	0.26	0.29	0.26	0.21	0.17	0.09	0.00
0.00	0.10	0.19	0.25	0.32	0.35	0.32	0.25	0.19	0.10	0.00
0.04	0.10	0.23	0.30	0.37	0.42	0.37	0.30	0.23	0.10	0.04
0.00	0.10	0.24	0.35	0.44	0.49	0.44	0.35	0.24	0.10	0.00
0.00	0.09	0.25	0.40	0.52	0.58	0.52	0.40	0.25	0.09	0.00
0.00	0.09	0.26	0.47	0.60	0.67	0.60	0.47	0.26	0.09	0.00
0.00	0.09	0.25	0.54	0.68	0.75	0.68	0.54	0.25	0.09	0.00
0.00	0.09	0.25	0.61	0.76	0.82	0.76	0.61	0.25	0.09	0.00
0.00	0.08	0.24	0.64	0.83	0.87	0.83	0.64	0.24	0.08	0.00
0.00	0.06	0.23	0.65	0.89	0.91	0.89	0.65	0.23	0.06	0.00
0.00	0.04	0.21	0.63	0.93	0.94	0.93	0.63	0.21	0.04	0.00
0.00	0.05	0.17	0.57	0.97	0.97	0.97	0.57	0.17	0.05	0.00
0.00	0.02	0.13	0.43	0.99	0.99	0.99	0.43	0.13	0.02	0.00
0.00	0.00	0.06	0.36	0.98	1.00	0.98	0.36	0.06	0.00	0.00
0.00	0.00	0.00	0.04	0.61	1.00	0.61	0.04	0.00	0.00	0.00
0.00	0.00	0.00	0.04	0.23	0.65	0.23	0.04	0.00	0.00	0.00
0.00	0.00	0.00	0.03	0.11	0.23	0.11	0.03	0.00	0.00	0.00
0.00	0.00	0.00	0.00	0.00	0.04	0.00	0.00	0.00	0.00	0.00

Downrange ↓

Crossrange →

Note: Probability points represent points on ground spaced 2000 ft apart

GP78-1118-4

Figure 5 Typical probability footprint

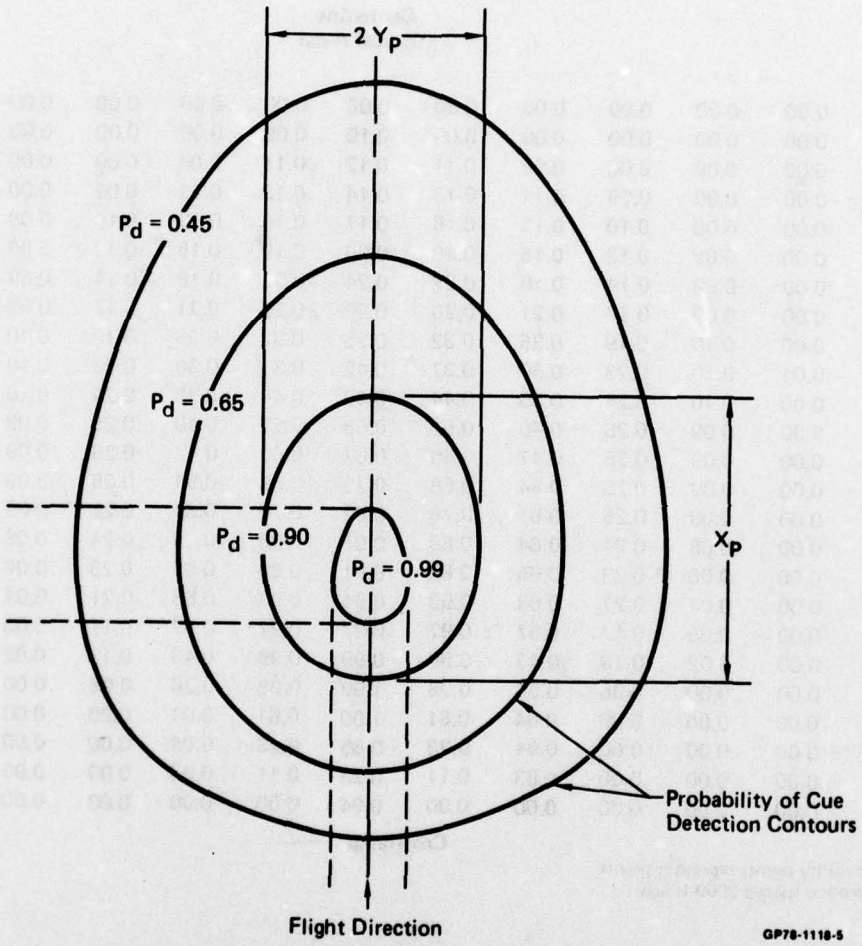

Figure 6 Probability contours of VARVS footprint

In order to conduct an effective search the operator must cover as much of the search area as possible. This may be accomplished by slewing the sensor from side to side in a systematic fashion, taking care not to spend too much or too little time at each slew position. Both slewing the sensor and searching the display take time. Specifically, let t_{sl} be defined as the average time it takes to slew the sensor and let it settle to its steady state, and t_g be the time related to a glimpse at the display. The time per glimpse has been measured to be about 0.25 to 0.3 seconds.

The operator can optimize his search process by properly adjusting the allocation of time to sensor slewing and the time spent searching the display between slews. The total time (t_a') required for search is calculated in Equation (2).

$$t_a' = ((n_g \cdot t_g) + t_{sl}) \cdot n_{sl} \tag{2}$$

where n_g defines the number of glimpses per slew and n_{sl} is the number of slews that will be made during the time the sensor platform travels a distance X_p. Under the assumptions of a nominally constant depression angle

$$t_a' \leq t_a \tag{3}$$

Thus:

$$t_a' = ((n_g \cdot t_g) + t_{sl}) \cdot n_{sl} \leq t_a \tag{4}$$

The upper bound on t_a' further defines the restrictions of choices of n_g and n_{sl} chosen for optimal results.

b. Probability Calculations

The total target acquisition probability (P_T) can be modeled as the product of four probabilities, viz:

$$P_T = P_c \cdot P_d \cdot P_r \cdot P_s \tag{5}$$

where P_c is the probability of detecting the true cue given the cue is within the FOV of the sensor, P_d is the probability that the observer will detect the target if he is looking at the cue, and P_r is the probability that the observer will recognize the target if he is looking at the target. Finally, P_s is the probability that the true cue falls within the chosen probability contour during the search process. The probabilities P_c, P_d and P_r are functions of line pairs across the target or cue.

Now we will define the probability of detecting the cue, given the observer is looking at the cue (P_c'). The prime indicates that this probability does not take into account multiple glimpse and multiple cue possibilities. This conditional probability of cue detection (P_c') is modeled using the form,

$$P_c' = 1 - \exp\left[-(a\,N_c + b)^2\right] \tag{6}$$

where N_c is the number of resolution elements across the cue averaged over the portion of the footprint used. N_c has units of line pairs. One resolution element across the cue is generally accepted as the threshold for 90% probability of target detection. It has also been found that the probability of detection goes to zero somewhere in the range of 1/7 to 1/8 line pairs across the cue. The constants a and b are evaluated such that

$$P_c' = 0.9 \text{ for } N_c = 1.0 \tag{7}$$

$$P_c' = 0.0 \text{ for } N_c = 0.13$$

Using Equation (7) to define a and b in Equation (6) results in

$$P_c' = 1. - \exp\left[-(1.75\,N_c - .23)^2\right] \tag{8}$$

Now the conditional probability of target detection (P_d) will be defined. It is similar to P_c' except that instead of the number of resolution elements across the cue, the number of resolution of elements across the target (N_t) is used. Thus,

$$P_d = 1 - \exp\left(-(1.75\,N_t - .23)^2\right) \tag{9}$$

The third probability of the target recognition from Bailey (6) is:

$$P_r = 1 - \exp\left(-\left(\frac{N_t}{2} - 1\right)^2\right) \tag{10}$$

A $P_r = 0.90$ corresponds to five line pairs across the target.

If a large portion of the display is used for search, the observer would probably have very little difficulty in covering the total search area but the average value of N_c would be low. At the other extreme, if only the area of the display near the optical axis is used for search, the observer would be hard pressed to adequately cover the total search area but the average value of N_c calculated would be larger than in the first case.

The effects of multiple glimpses and multiple targets was studied in detail before deciding on the type of model to be used. The performance of the observer can best be analyzed by answering the question, "What is the probability P(K) of finding exactly K targets in N glimpses?". This probability is usually associated with Binomial Distribution and is defined by:

$$P(K) = \binom{N}{K} p^K (1 - p)^{N-K}, \tag{11}$$

where

$$\binom{N}{K} = \frac{N!}{(N-K\,!)K!}$$

In the multiple cue acquisition case, the probability of finding a cue is a function of the number of unfound cues in the display; therefore, as the observer detects cues, the probability of finding another cue changes. The equation which relates the probability of finding a cue per glimpse for one cue contained within the display (P_c') to the probability (P(NT)) of finding a cue where multiple independent (NT) cues exist is:

$$P(NT) = 1 - (1 - P_c')^{NT} \tag{12}$$

As the observer detects and responds to possible cues, P(NT) decreases because the number of unfound cues is decreasing. Due to this non-stationary characteristic of P(NT), the expected number of cues found during K glimpses E(NT) cannot be calculated using compact methods such as Bernoulli trials (a form of the Binomial expansion). Therefore in the next paragraphs the probability density functions to cover this case will be developed.

The probability density function must define the probability of finding K cues in n_g glimpses for constant n_g and for all K such that K is an integer where

$$0 \leq K \leq n_g$$

Then one must determine all possible ways to detect K cues in n_g glimpses (all permutations), find the probability associated with each permutation, and sum these probabilities. This process is simplified by using a digital computer and its memory capabilities.

Consider the state diagram in Figure 7. The circles represents specific states as defined by the two axes, number of glimpses made (trials) and cues detected (successful results). Each state has associated with it the probability of being in that state. The probability of traveling from one state to another state is denoted by the flag on the arrow joining the two states. Each node defines the discrete density probability function of finding exactly K cues in n_g glimpses.

To determine the probability associated with any specific state, $P_c(n_g,K)$ one must determine all possible paths from state (0,0) to the state in question. The probability of traveling down a specific path is the product of all the flags along that path. The summation of the probabilities associated with all possible pathways defines $P_c(n_g,K)$. The probability of being in state (0,0) is

$$P(0,0) = 1$$

The calculations required to generate the density distribution can be simplified if one makes the observation that each state $P_c(n_g,K)$ is a function of at most two previous states. For example:

$$P_c(3,2) = P_c(2,2) \cdot \bar{p}(K - 2) + P_c(2,1) \cdot p(K - 1) \tag{13}$$

or alternately

$$P_c(1,0) = P_c(0,0) \cdot \bar{p}(K) \tag{14}$$

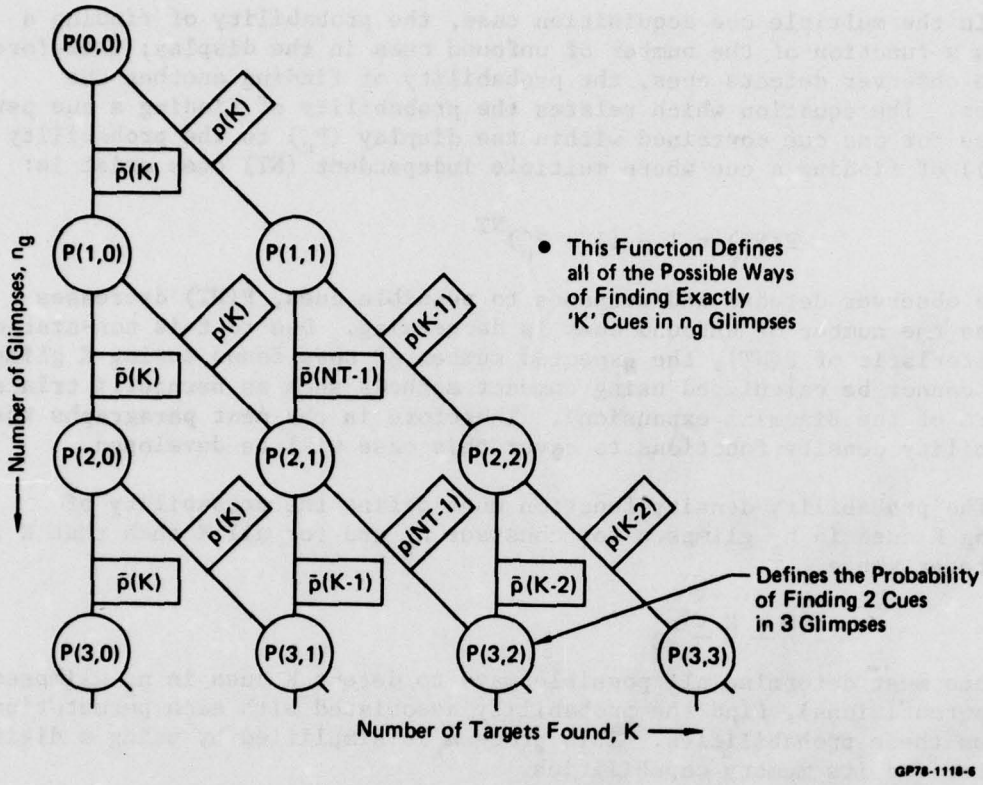

Figure 7 Acquisition probability density function

The expected number of possible cues found ($E[K(n_g)]$ is defined by

$$E[K(n_g)] \triangleq \int_{-\infty}^{\infty} K \cdot P(n_g) \cdot dK \tag{15}$$

The discrete nature of this function allows the process of integration to be performed by summation. Thus,

$$E[K(n_g)] = \sum_{i=1}^{n_g} i \cdot P(n_g, i) \tag{16}$$

If all possible cues have equal probability of being the true cue, the probability of finding the right cue P_c is simply

$$P_c = \frac{E[K(n_g)]}{NT} \tag{17}$$

The number of glimpses the user is able to make is a function of the average glimpse rate, $(1/t_g)$, the sensor slew period (t_{sl}) and the number of cues within the display (n_{td}). The targets found within a particular display are calculated in terms of cue density. Cue density in an input to the program and has units cues per nautical mile squared. Therefore, the maximum number of glimpses N_g the operator has time to make is:

$$N_g = \frac{t_a}{t_g + (\frac{t_{sl}}{n_{td}})} \tag{18}$$

The term $\frac{t_{sl}}{n_{td}}$ takes into account that n_{td} targets can be examined without requiring the user to slew the sensor.

The final probability (P_s) to be calculated is the probability that the target is within the sensor field of view. If the cues are uniformly distributed throughout the search area, P_s can be calculated as:

$$P_s = \frac{\text{Area covered by the useable footprint}}{\text{Total search area}} \tag{19}$$

The area covered in an efficient systematic search (A_c) is proportional to the total number of slews (N_{sl}^T) and the area of the footprint determined useable for search (A_{fp}).

$$A_c = N_{sl}^T A_{fp} \tag{20}$$

The total search area (A_T) is assumed to be a rectangle of length X_T along the flight path and width $2 \cdot Y_T$. The total search area is defined:

$$A_T = 2 \cdot Y_T \cdot X_T \tag{21}$$

The number of slews the operator is able to make during the total search process is defined in terms of the platform velocity, search area length, and the amount of time spent during each sensor slew. Thus,

$$N_{sl}^T = \frac{X_T}{V_x(t_{sl} + n_g \cdot t_g)} \tag{22}$$

Substituting Equations (20), (21) and (22) into (19) results in

$$P_s = \frac{A_{fp}}{2 \cdot V_x \cdot (t_{sl} + n_g \cdot t_g) \cdot Y_T} \tag{23}$$

Equation (23) shows that under the assumption of systematic search with a constant depression angle, the length of the search area X_T has no effect on the optimum search results. The search area width on the otherhand has a direct effect on search performance.

In a specific mission with constant n_g glimpses per slew, P_s will decrease as Y_T increases. This decrease in P_s may be offset by decreasing n_g. This also has the effect of decreasing P_c, but has an overall positive effect. For light user load situations, for example low aircraft velocity and a "fast" slew time, the upper bound of Y_T may be the geometric cross-range capability of the sensor rather than the observers bandwidth.

c. VARVS Search Model Evolution

The VARVS search model has gone through a series of revisions in order to assure compliance with experimental data and to comply with our understanding of the search process. Special attention was taken in order to assure that arbitrary fudge factors were not introduced into the model during these revisions. The major revisions to the model will be discussed in the order they were implemented. In each case the problem encountered will be explained in terms of the model and a brief description of or reference to the final model will be made.

The problems and changes are:

1) The original model was unable to take into account multiple cues and the non-replacement nature of cue detection. The model only used the binomial distribution to calculate the probability that at least one cue would be found in n_g glimpses.

$$P_c(n_g,1) = 1 - (1 - P_g)^{n_g} \tag{24}$$

This problem was corrected by implementing the target acquisition function described by Figure 7 which takes into account both multiple glimpses and the effects of more than one cue on the display.

2) In the original model the maximum number (N_g) of glimpses allowed per sensor position was determined based on the premise that, if at all possible, the total search area would be covered. The lower limit of n_g in this case was one. While this assumption is sometimes true, it is not always the case. To assure optimum use of time, the process described by Equation (2) was implemented.

3) Upon comparing experimental data with calculated results, it was found that the calculated prediction for high cue densities were substantially lower than experimental results. Additional comprehension of the acquisition process indicated that the observer was satisfied to use the lower resolution of the off-axis portion of the display in order to save time and at the same time apparently increase his performance.

To take this into account 1) an average value of resolution across the target was calculated rather than the use of the on-axis value, 2) the actual probability contour used to describe the useable footprint was determined by an optimization routine and 3) the size of the useable footprint was used to determine n_{td} used in Equation (18).

The VARVS search model then under went a series of implementation streamlining to cut costs and allow a finer portion of the footprint (ΔA) description. The added data points calculated helped give a better estimation of the effects of lens distortion.

d. Flow Diagram

A simple flow chart showing the implementation of the model is shown in Figure 8, and will be briefly reviewed.

First the ground footprint is calculated using an adaptation of the NVL model. The footprint is evaluated and the portion of the footprint to be used for search is chosen. This augmented footprint is characterized in terms of length, width, and average number of line pairs across the target. These characteristics are used to calculate the time available for search (t_a), and the probability of detecting the cue in a single glimpse given there is a single cue and the observer is looking at the cue (P_c').

The first optimization to be made is to allocate the time available between pure display search and slew time. If the user spends too much time looking at one portion of the total search area he is apt to leave large portions of the search area unsearched. Alternatively, if the observer wastes too much time slewing the sensor, he cuts down on the amount of time he has for search. The indicated target acquisition function (TAF) loop determines the optimum combination of glimpses per slew and area coverage as it pertains to each situation.

When an optimum solution is found, the probabilities of target detection (P_d) and recognition (P_r) are calculated. The probability of mission success is evaluated in terms of the probability of detecting the target (P_{DET})

$$P_{DET} = P_c \cdot P_d \cdot P_s \tag{25}$$

and the probability of recognizing the target (P_T)

$$P_T = P_{DET} \cdot P_r \tag{26}$$

The probabilities of mission success are evaluated and a new strategy of search may be chosen if the possibility of better results is indicated. A new strategy may either increase or decrease the size of the useable footprint. For example, decreasing the useable footprint size will increase P_T and force the product of P_c and P_s to decrease. When an adjustment is made in the size of the footprint, the time allocation optimization must be

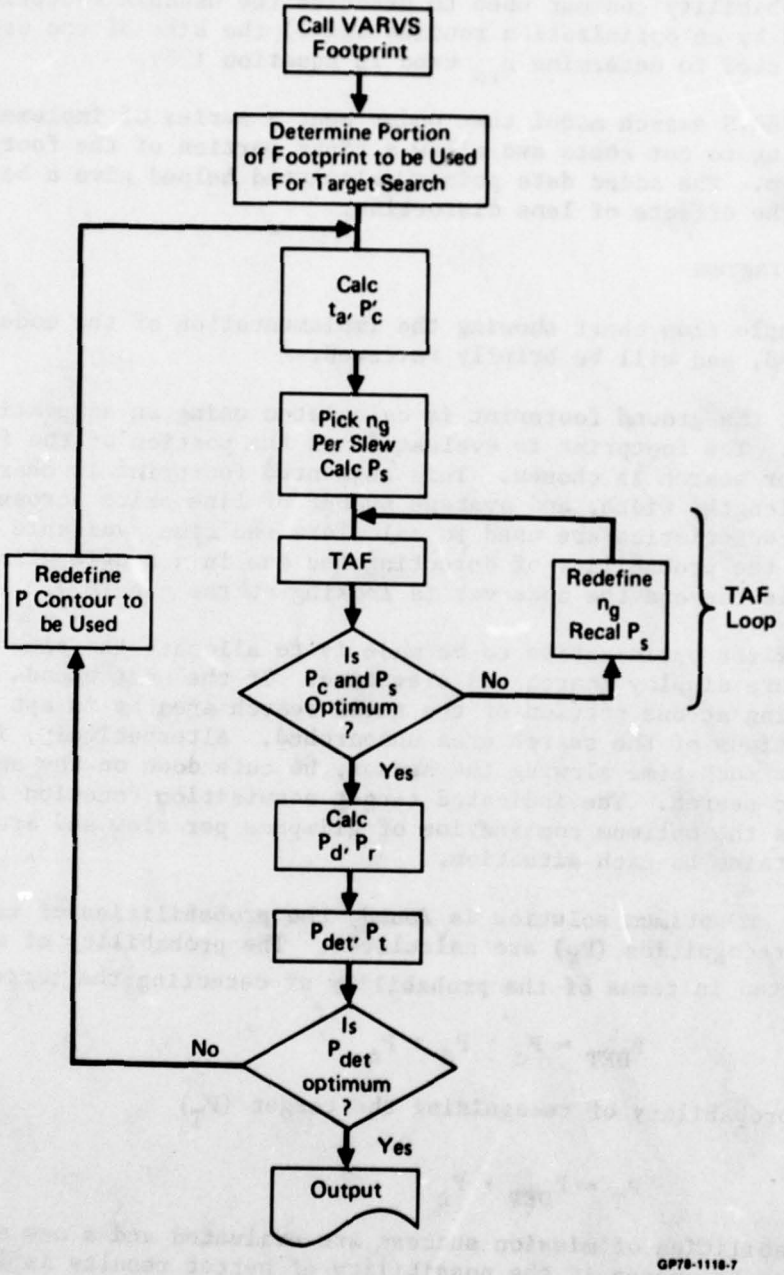

Figure 8 Computer flow diagram

reevaluated and then P_{DET} and P_r are recalculated. The loop continues until the model operator determines that the optimum has been found. This shows the adaptiveness that must be present in the model and in real search to arrive at optimum results.

The TAF loop is implemented on a digital computer while the decision to try a different portion of the footprint is left to the program operator. The major cost in computer time is spent in the generation of the ground footprint. Because of the lens distortion function a new footprint must be generated at each depression angle, altitude or velocity. This cost in computer time to generate new footprints becomes the limiting factor as far as cost is concerned.

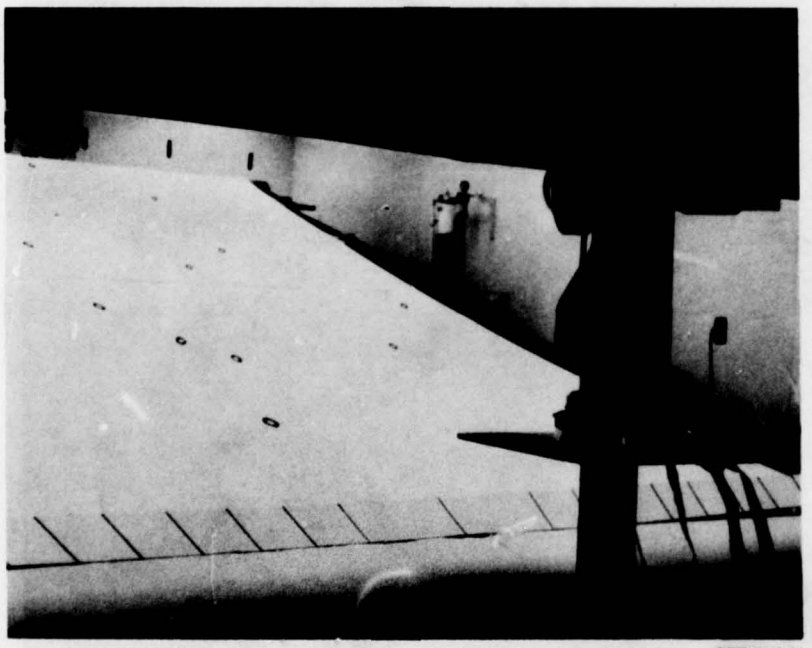

GP78-1118-51

Figure 9 Moving terrain test apparatus

3. EXPERIMENT DEVELOPMENT

The experiment consisted of a 10 ft. x 20 ft. treadmill which gave a 10 ft. by 40 ft. simulated terrain map, a camera, and remote display stations. The treadmill and camera are shown in Figures 9 and 10. A 600/1 scale was selected. This provided useable coverage area of 6000 ft. by 24,000 ft. (4 sq. miles). At a simulated velocity of 1,000 ft/sec. the mission time is 24 seconds. The camera's optical axis was located 3.5 ft. above the terrain map which represents a scale altitude of 2,100 ft. Thus the sensor could operate over scale slant ranges varying from 12,800 ft. to about 2,200 ft. when the sensor is located one foot from the treadmill.

Two areas of difficulty were encountered with the experiment. The first was in getting the terrain map of the treadmill to run straight and true. This was corrected by installing a center spreader between the rollers of the treadmill. This caused the rollers to bow outwards at their center while maintaining the constant linear surface velocity that is necessary to prevent wrinkles from forming in the map (this is also the reason the conventional solution to belt tracking problems, domed rollers, could not be used). The other problem area was in selecting the best type of cues and targets for the experiment. Since the analytic model is based on the observer visually examining a number of cues to determine which one contains the target, we decided the cues could be identical. Since many cues were required, this greatly reduced the effort required to fabricate the map. We found it very difficult, however, to find a cue which did not reveal the target because of contrast variation. For example, the target

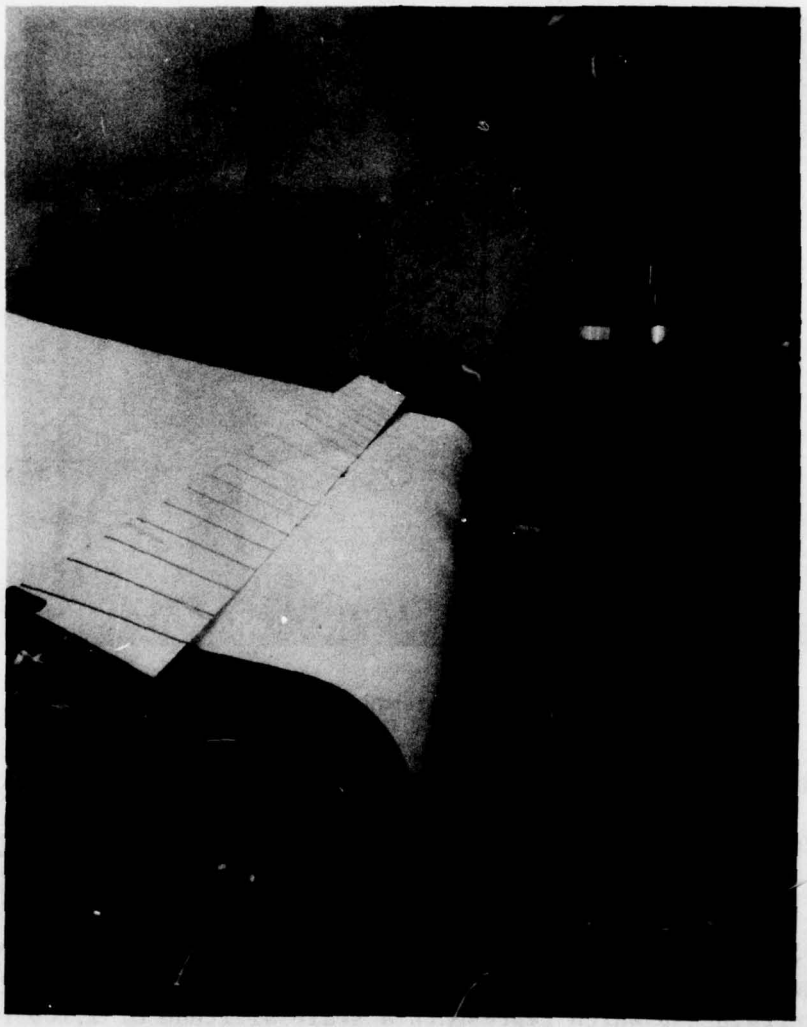

GP78-1110-52

Figure 10 Camera tracking targets on terrain

must have a critical dimension of 1/5 the cue dimension. If one uses a square or circle as a cue with a smaller contrasting square or circle as a target, the fact that the cue contains a target is instantly visible because this cue now has a noticeably lower contrast than the other cues. This led us to use Landholt C ring as cues and targets. The Landholt C ring shown in Figure 11, is well accepted for acquisition studies. In our experiment solid rings were used except for cues with a gap which represent the target. The gap occupies a very small portion of the ring and therefore produces no noticeable contrast loss.

Implementing the C ring for our experiment proved much more difficult than anticipated. A circle on the terrain map appears as an ellipse on the viewing surface. This makes the gap have variable angular subtense depending on its location on the C ring and the viewing geometry. We corrected this problem by locating the gap on a side of the ring and by making the gap three dimensional. This created another problem, however. Due to shading of the ring by the 3D gap, a noticeable contrast variation in the target ring relative to the closed rings were created. To correct this, the C rings were made elliptical and oriented so that they appear circular and have uniform crossection on the viewing screen. Since the viewing geometry continually varies over the terrain map we chose to optimize geometry for what we thought to be the nominal acquisition distance-between 6,000 and 8,000 ft. downrange. This ring configuration is shown in Figure 12. We determined experimentally that this ring worked quite well over the entire 12,000 x 6,000 scale feet viewing area. At short ranges the elliptical shape was apparent but the rings occupied so large an angular subtense that it caused no distraction.

Since the threshold resolution of the VARVS is in the area of one milliradian, we decided to scale the C rings to provide a one milliradian target subtense at the maximum slant range. This would make target detection possible anywhere on the map and make search dynamics the dominant factor. For convenience in fabrication, a 0.25 inch target dimension was chosen. This yields an angular subtense of 0.99 mr at the maximum slant range. The other ring dimensions were scaled from Figure 12.

In the actual experiment the solid cues (rings) were placed randomly on the map with the required average cue density as shown in Figure 13. The cue containing the target was placed on the map randomly at the start of each mission. The observer's task was therefore to find the target before it was overflown. The exact procedures will be discussed later.

Another detail that had to be worked out before the experiment could proceed was the number of runs or missions required to establish the statistical significance of the experiment data. An analysis was run using the Chebyshev Inequality. This analysis, presented in Appendix C yielded the equation:

$$n \geq \frac{p(1-p)}{\gamma \cdot \varepsilon^2} \tag{27}$$

where

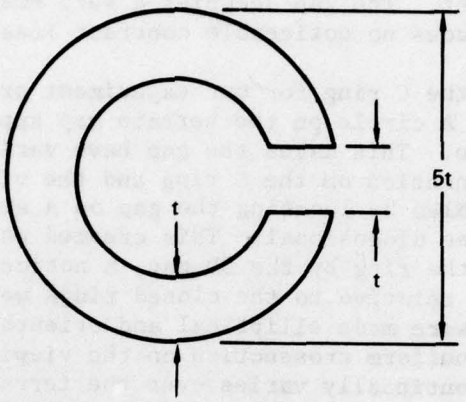

Figure 11 Landholt c-ring

Figure 12 Modified c-ring

QP78-1226-9

Cue Density on Ground (Cues/nm^2)	Cue Density on Treadmill (Cues/ft^2)	Total Cues on Treadmill
10	0.1	40
20	0.2	80
40	0.4	160

GP78-1118-10

Figure 13 Cue density scaling

n is the number of data points required
p is the average probability of detection expected
ε is the desired tolerance interval
γ is the probability data points will fall out of the tolerance band $\pm\varepsilon$

This equation is plotted on Figure 14 for 10% and 5% tolerance levels. For the target scenario chosen, the preliminary performance analysis indicated about 80% probability of target detection should be expected. Figure 14 shows about 100 data points would be required to establish P_d within 10% while 400 points would be required to establish P_d within 5%. Considering the great number of conditions that must be run, we elected to use the 10% tolerance level.

Since many data points must be collected for each set of input parameters, an accurate estimate of the parameter ranges to be studied was required. As a minimum we felt we should run four depression angles, three speeds, two cue densities, and two offsets for each of the four sensor types. In addition we wanted to run the VARVS with both hand and head control using the ONR dome projection system and hand control with the USAF direct view display. Altitude was not included because of the difficulty of implementing changes to the test set-up and these effects would be purely geometrical and are easily predicted. The actual test plan is shown in Figure 15.

The actual test was run as follows. A test conductor was stationed at the lower end of the treadmill adjacent to the camera as shown in Figure 16. The test conductor had a two way communication link with the observer who was at the display station in another room. A third man, the map controller was located under the treadmill as shown in Figure 16. The map controller's job is to continually move the cues and targets on the map so the observer does not memorize the pattern. The test director tells the observer what depression angle to use and checks visually to see that the camera is properly oriented downrange. He then gives a start command to the map controller. After a variable time delay (0 to 15 sec.) the controller places a cue on the map which contains the target. Meanwhile the observer searches the map for the target. If the observer finds the target, he

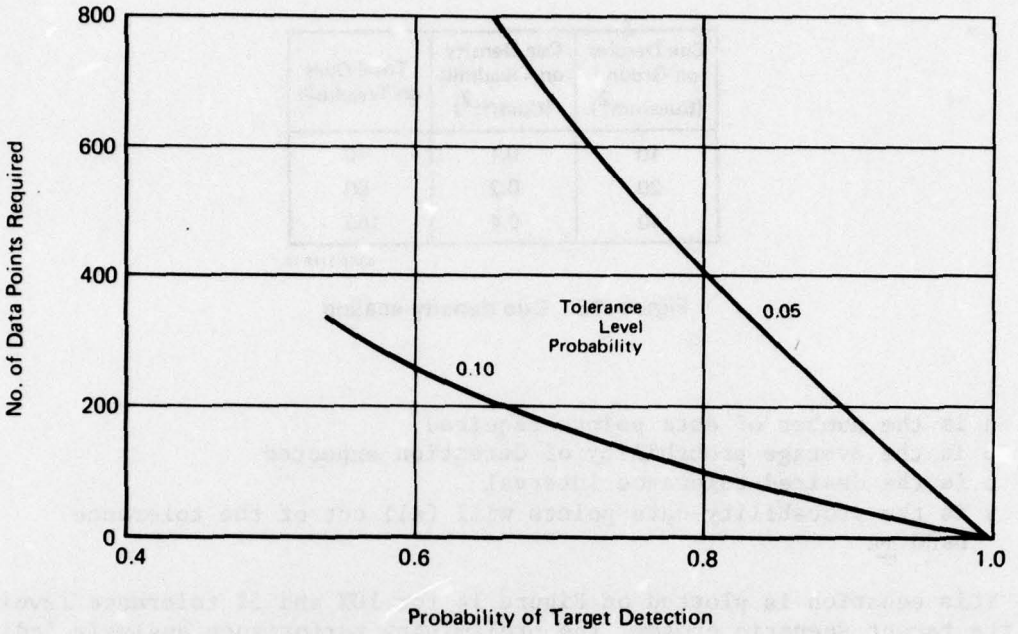

Figure 14 Statistical significance curves for 95% confidence level

Test	System	Display	Control Type	Altitude (1000 ft)	Speed (ft/sec)	Lateral Coverage (1000 ft)	Cue Density ($cues/nm^2$)	Downrange Position (1000 ft)	Total Data Sets
1	VARVS	Dome	Hand	2.1	840	6	10	4,6,8,10	4
2	VARVS	Dome	Head	2.1	840	6	10	4,6	2
3	VARVS	Direct View	Hand	2.1	840	6	10	6	1
4	VARVS	Dome	Hand	2.1	1200	6	10	4,6	2
5	VARVS	Dome	Hand	2.1	840	3	10	4,6	2
6	VARVS	Dome	Hand	2.1	840	6	20	6,8	2
7	20^0TV	CRT	Hand	2.1	840	6	10	4,6,8,10	4
8	20^0TV	CRT	Hand	2.1	1200	6	10	4,6	2
9	20^0TV	CRT	Hand	2.1	840	3	10	4,6	2
10	20^0TV	CRT	Hand	2.1	840	6	20	4,6	2
11	10^0TV	CRT	Hand	2.1	840	6	10	6,8,10	3
12	35.5^0 TV	CRT	Hand	2.1	840	6	10	4,6,8,10	4
									30

GP78-1118-12

Figure 15 Test plan

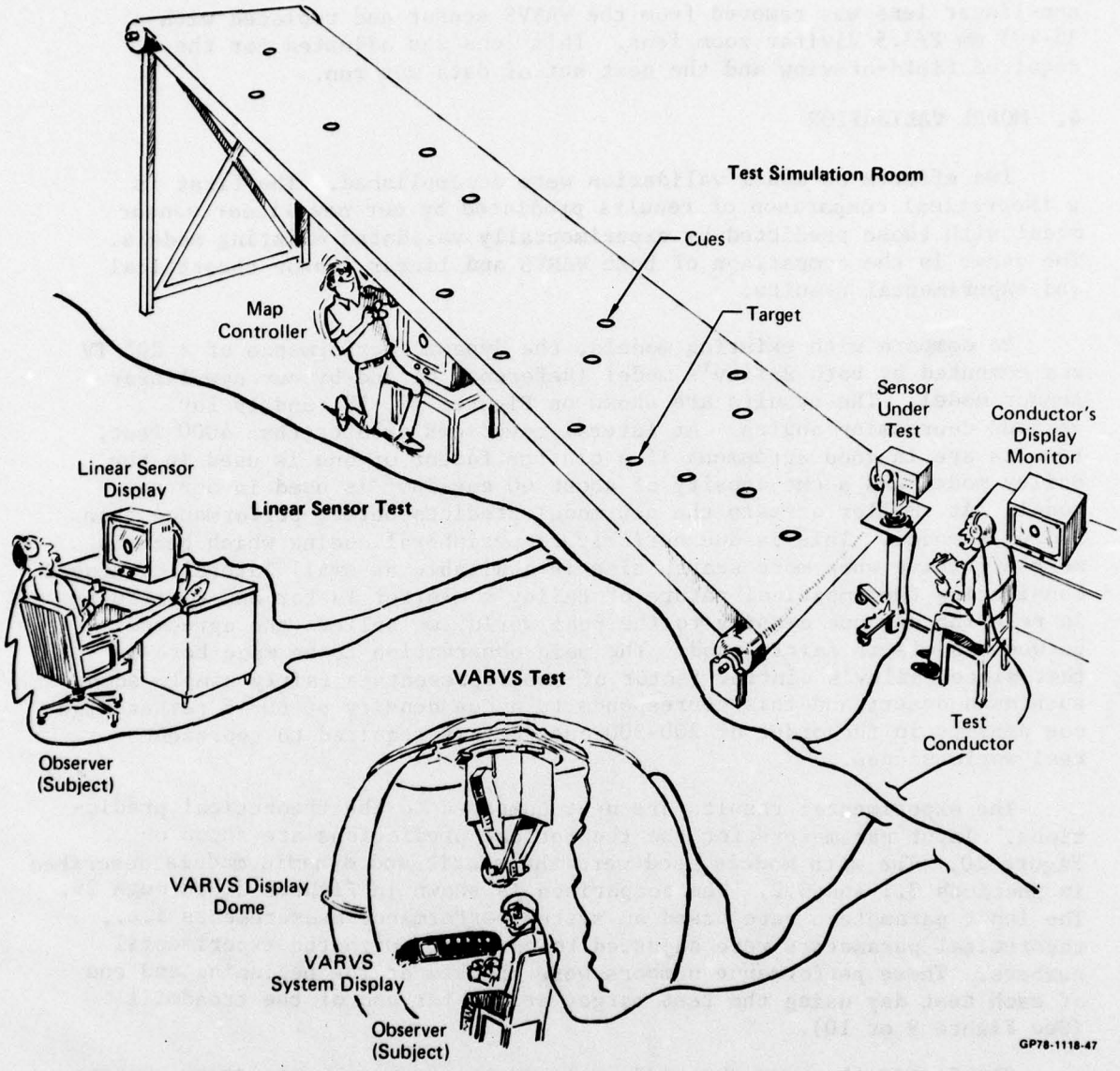

Figure 16 Experimental test setup

notifies the test conductor who checks the camera orientation and auxiliary monitor to see that it is truly pointing at the target. If it is a valid acquisition the test is terminated. Otherwise the test continues until the conductor sees the target has been overflown. Generally ten missions were run before the observer is given a rest. Observers were changed after four sets of ten missions each. After all missions were completed with one type of sensor, the sensor was converted to another type. In order to keep all system parameters constant, only the sensor lens was changed. For the VARVS, the non-linear lens was used. For linear sensor tests, the

non-linear lens was removed from the VARVS sensor and replaced with a 35-105 mm F/3.5 Vivitar zoom lens. This lens was adjusted for the required field-of-view and the next set of data was run.

4. MODEL VALIDATION

Two efforts on model validation were accomplished. The first is a theoretical comparison of results predicted by our new linear sensor model with those predicted by experimentally validated existing models. The other is the comparison of both VARVS and linear sensor theoretical and experimental results.

To compare with existing models, the dynamic performance of a 20° TV was computed by both Bailey's model (Reference 6) and by our new linear sensor model. The results are shown on Figures 17, 18, and 19 for various depression angles. At lateral coverages greater than 4000 feet, results are in good agreement if a clutter factor of one is used in the Bailey model and a cue density of about 60 cues/nm^2 is used in our new model. At smaller offsets the new model predicts better performance than Bailey's model. This is due entirely to peripheral cueing which becomes more effective when more search time is available at small lateral coverages. Considering the empirical nature of Bailey's clutter factor and difficulty in relating our cue density to the real world, we believe the agreement between models is fairly good. The main observation to be made here is that since Bailey's clutter factor of one represents a fairly simple scene such as a desert and this corresponds to a cue density of 60, a rather high cue density in the order of 200-300 cues/nm^2 is required to represent real world scenes.

The experimental results are next compared to the theoretical predictions. Input parameters for the theoretical predictions are shown on Figure 20. The math models used were the static and dynamic models described in Sections 3.1 and 3.2. The comparison is shown in Figures 21 through 29. The input parameters were based on system performance measurements i.e., theoretical parameters were adjusted to correlate with the experimental numbers. These performance numbers were checked at the beginning and end of each test day using the test target at the far end of the treadmill (See Figure 9 or 10).

One factor that was observed early in the experimental effort was that a large difference exists between resolving C ring targets and the 3 bar test targets. In order to study this, a C ring test target was placed next to the 3 bar target - See Figure 9 or 10. The system was defocused until a C ring was just resolved. Then the frequency of the 3 bar pattern that was also just resolved was noted. Regardless of the C ring size, we found that the 3 bar pattern having one half bar width equal to the C ring gap could be resolved also. Since the model was developed and adjusted to predict 3 bar resolution, we had to use a target scale size of 25 ft. to predict experimental results which used a C ring gap of scale 12.5 ft. Figures 21 through 24 show comparisons for the four system types, the VARVS and linear sensor with three fields-of-view. On each of these curves the theoretical prediction from the new model are plotted as solid lines. The experimental points are shown as averages of the 100 data points and the associated standard deviation in the data. In general one will observe

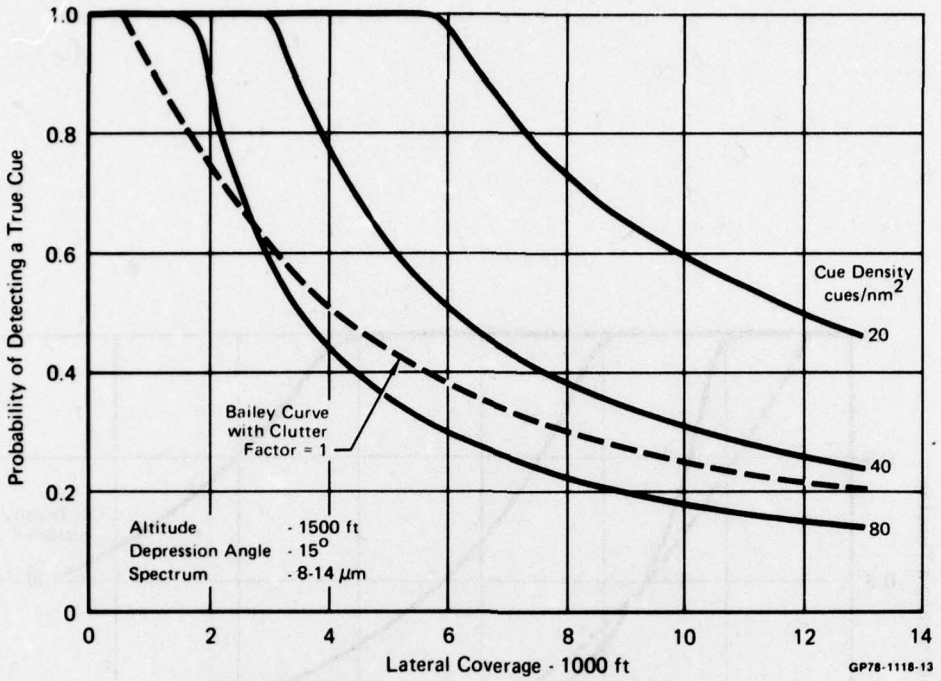

Figure 17 Probability of detection of TV with 20° FOV

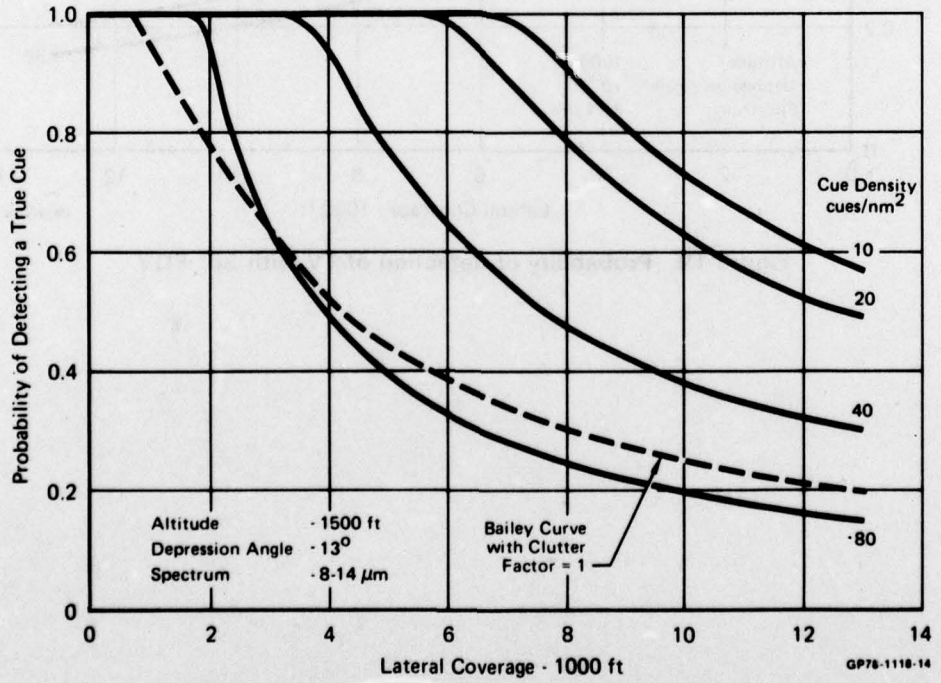

Figure 18 Probability of detection of TV with 20° FOV

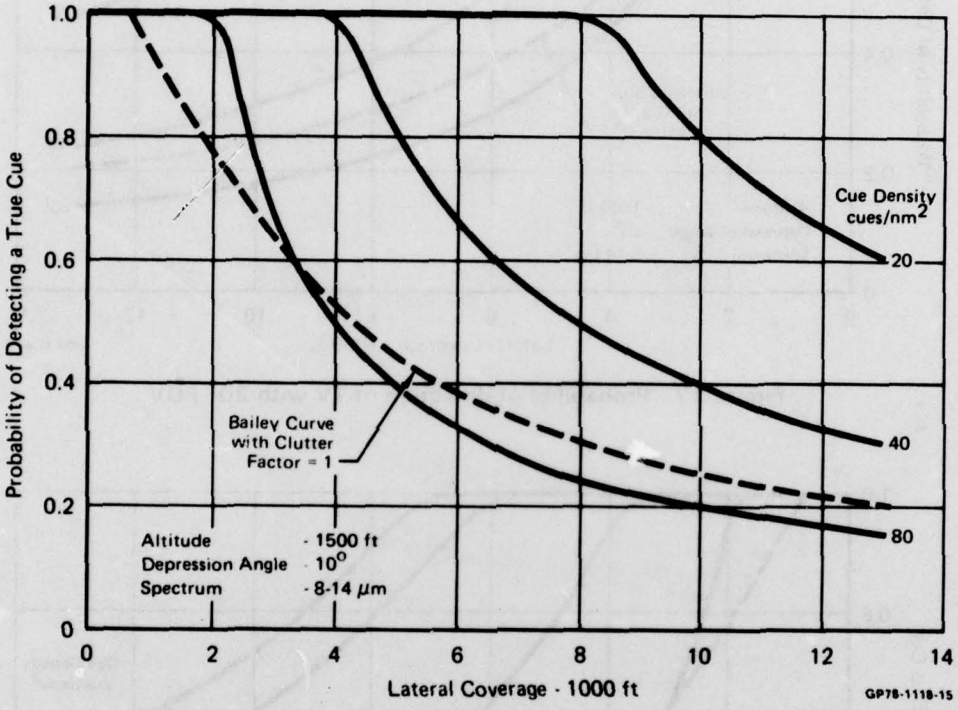

Figure 19 Probability of detection of TV with 20° FOV

Parameter	Units	Value	
		TV	RVS
Number of Scan Lines		525	525
Light Level	fL	1	1
Lens Blur	μ	50	45
Display Blur	μ	105	105
Bandwidth	Mc	4	4
F/No.		5.6	5.6
Altitude	ft	2100	2100
Offset	ft	3000	3000
Velocity	ft/sec	840	840
Slew Period (Nom)	sec^{-1}	0.6	0.5
Glimpse Time	sec	0.25	0.25
Resolution	mr/cy	10^{o} FOV - 0.469 28^{o} FOV - 0.945 35.5^{o} FOV - 1.72	0.928
Focal Length	mm	10^{o} FOV - 104.5 28^{o} FOV - 51.8 35.5^{o} FOV - 28.5	50.8

GP78-1118-25

Figure 20 NVL model input parameter values

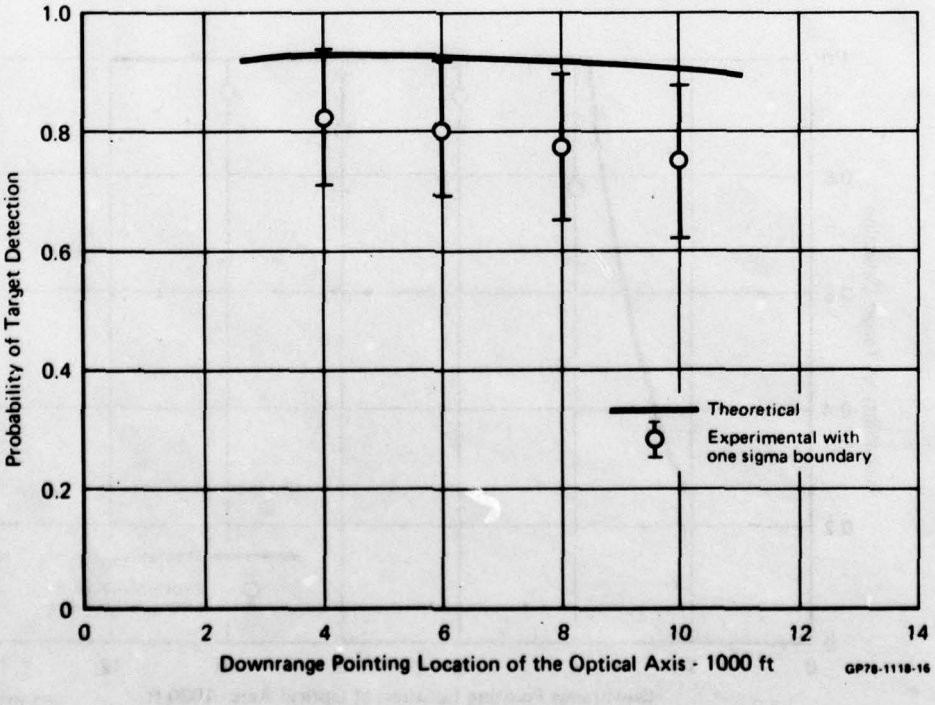

Figure 21 Comparison of VARVS theoretical to experimental data

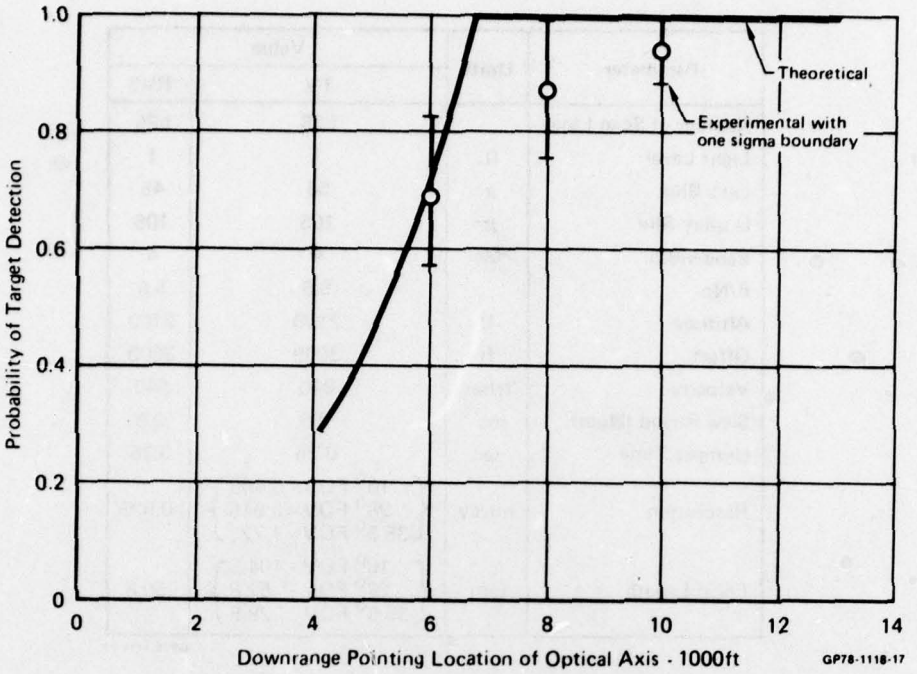

Figure 22 Comparison of 10° FOV TV experimental to theoretical data

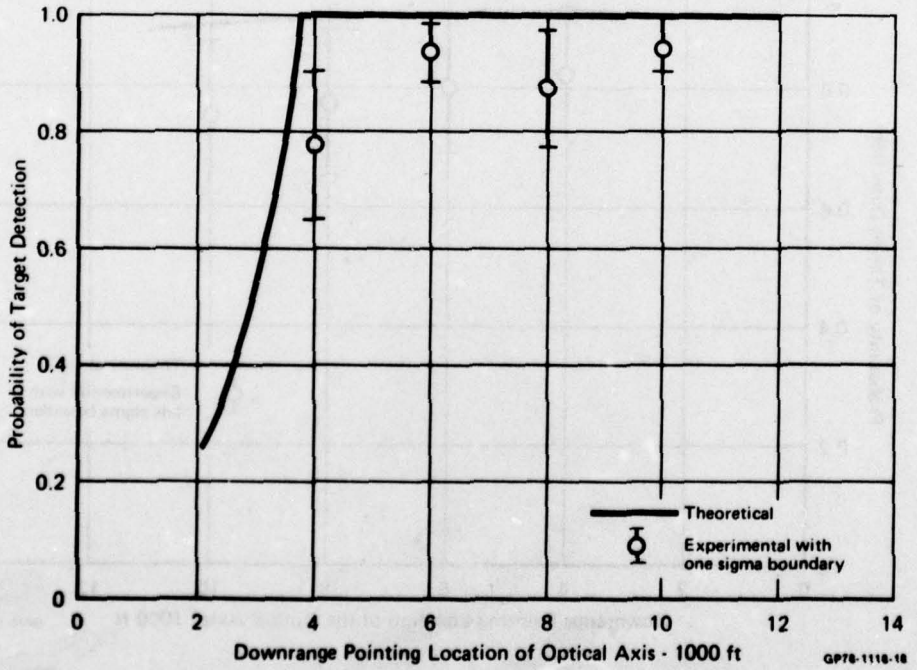

Figure 23 Comparison of 20° FOV TV experimental to theoretical data

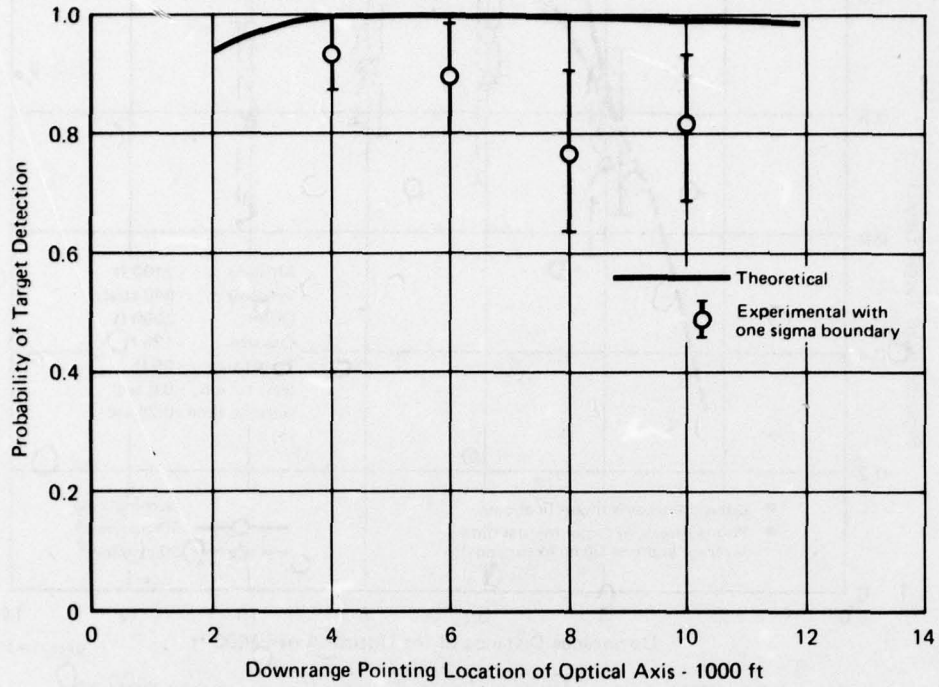

Figure 24 Comparison of 35.5° FOV TV experimental to theotetical data

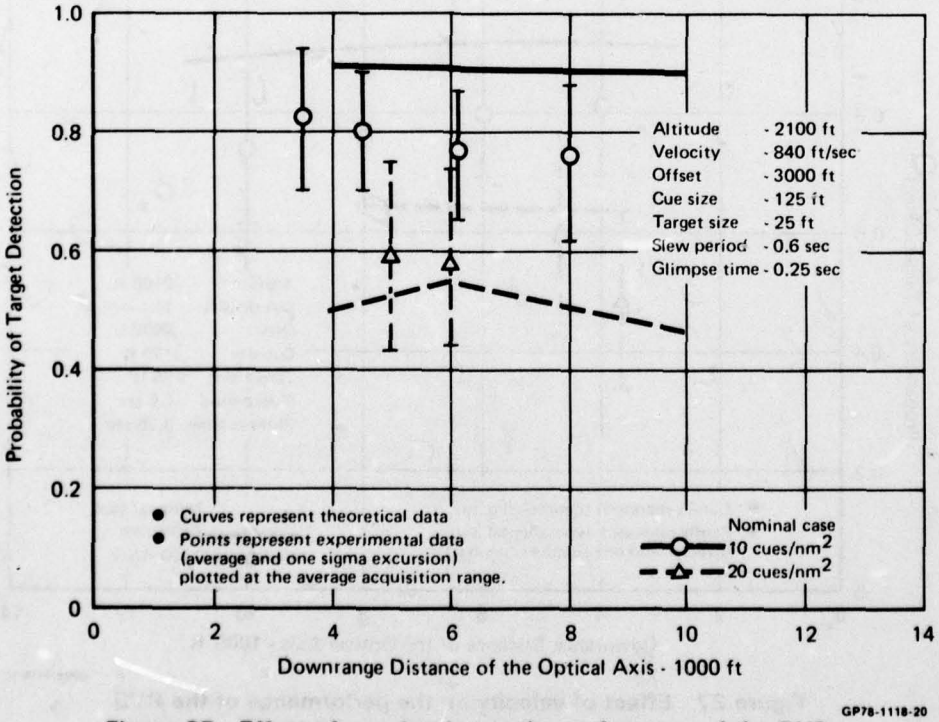

Figure 25 Effect of cue density on the perfomance of the RVS

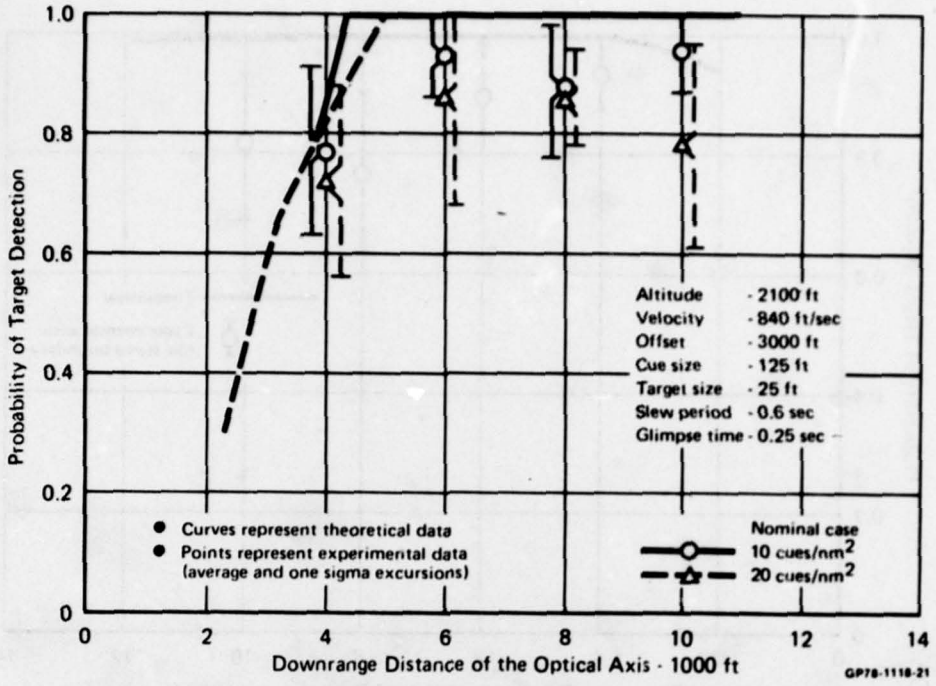

Figure 26 Effect of cue density on the performance of 20° FOV TV

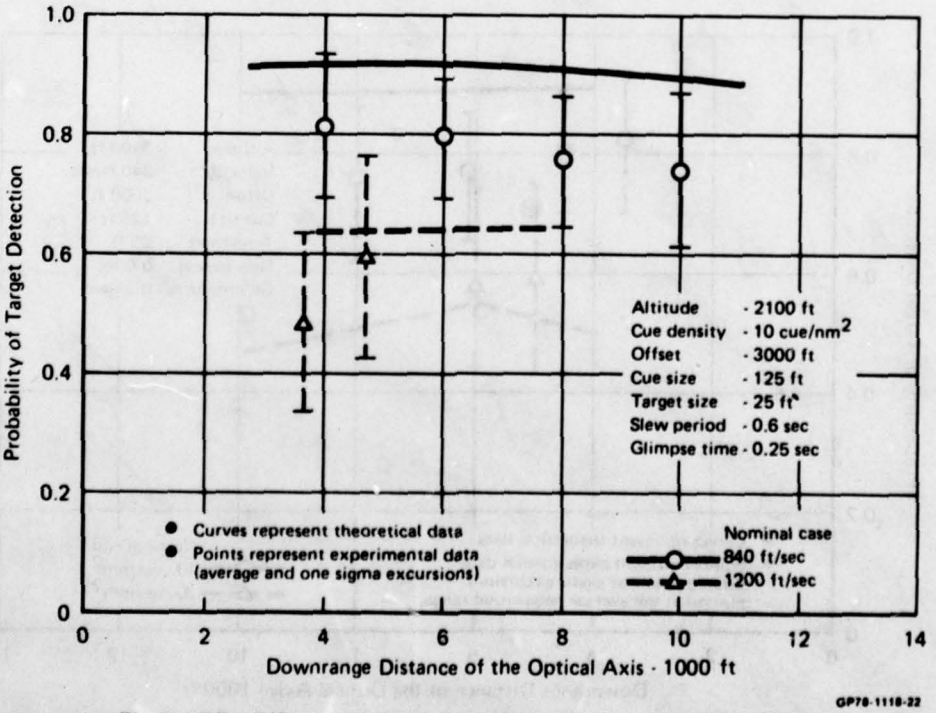

Figure 27 Effect of velocity on the performance of the RVS

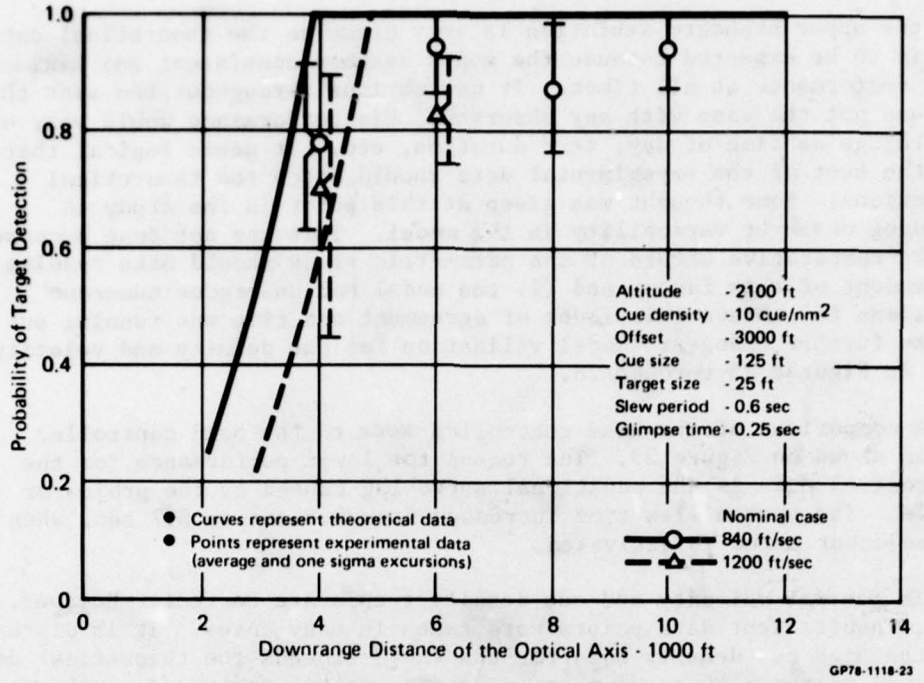

Figure 28 Effect of velocity on the performance of the 20° FOV TV

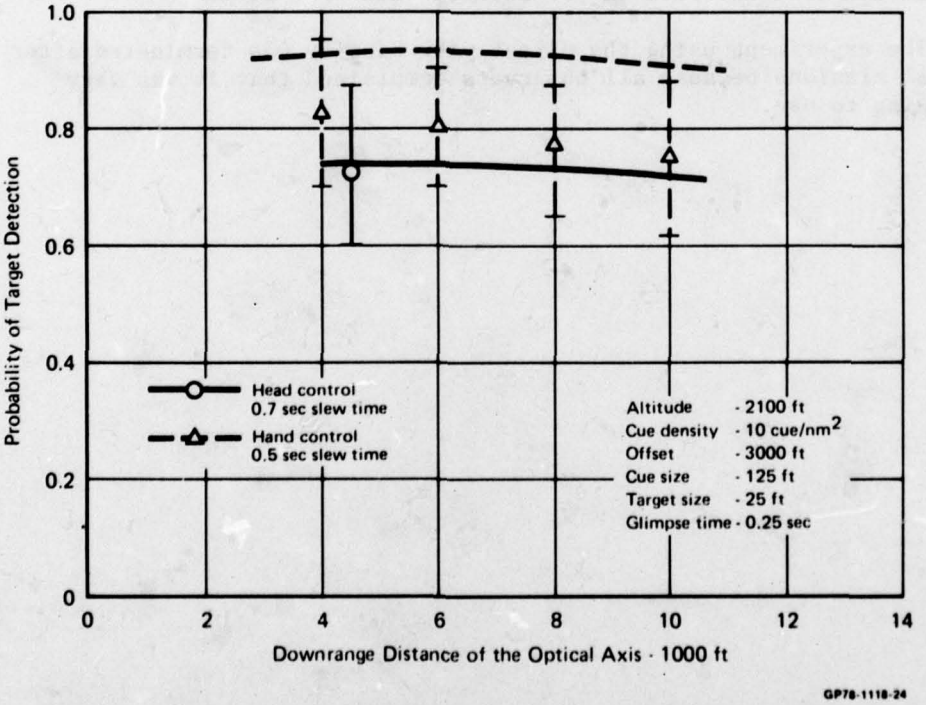

Figure 29 Performance comparison of head control to hand control

that the upper standard deviation is very close to the theoretical data. This is to be expected because the model assumes consistent and maximum human performance at all times. It was obvious throughout the test that this was not the case with any observer. His performance would vary with such things as time of day, test duration, etc. It seems logical therefore that the best of the experimental data should match the theoretical predictions. Some thought was given at this point in the study to including observer variability in the model. This was not done because, (1) the comparative nature of the parametric study should make results independent of this factor and (2) the model had undergone numerous iterations to achieve this level of agreement and time was running out to make further changes. Model validation for cue density and velocity are given in Figures 25 through 28.

A comparison of the hand controlled mode to the head controlled mode is shown on Figure 29. The reason for lower performance for the head control mode is the additional servo lag caused by the projector gimbals. The system slew time increases from 0.5 sec to 0.7 sec. when the projector servo is activated.

In general velocity and cue density trends are correct. However, as noted, insufficient data points were taken in many cases. It is disturbing that the high cue density data for the VARVS exceeds the theoretical data. We wanted to run a 40 cue/nm^2 experiment to see if the trend continues but time did not permit this. No data for lateral coverage is presented because for the range of coverages possible with the test setup (0-1500 feet) experimental and theoretical probability data were 100%.

The experiment using the direct view display was terminated after several missions because all observers complained that it was very fatiguing to use.

SECTION IV

PARAMETRIC ANALYSIS

In this section the performance of the IR VARVS is compared to a conventional IR TV system using the analysis models developed and identified earlier. Parameters of cue density, altitude, velocity and target offset from the flight path are pertubated to measure the effectiveness of the two systems. This effectiveness then can be related to the particular mission type best suited for the sensor. It was determined that in addition to the above parameters, the IR VARVS was sensitive to slew time so this was also retained in the parametric analysis.

The infrared target acquisition models consists of two static sensor performance models and a dynamic model. The static models are the NVL model (Reference 4) for the linear sensor and the MCAIR IR VARVS model which is an adaptation of the NVL model. This model was developed in prior efforts (Reference 2 and 3) and is included as Appendix D. System parameters used in modeling the IR VARVS and three conventional FLIRS are shown in Figure 30. The FLIR scanners are second generation types with 488 resolution elements, parallel array with a nine element Time Delay Integration (TDI) which was shown in the Reference 2 report to be optimum for the IR VARVS. The optical quality for the non-linear lens was also taken from that study. Display quality for the IR VARVS in the model is based on state of the art in optical fabrication and is somewhat better than the experimental equipment (50 μ blur compared to 105 μ). FLIR system parameters are believed to be representative of second generation state of the art systems.

The approach and data reduction techniques used in parametric analysis were described in Section II. A typical sequence in data reduction for the reconnaissance mission is presented below. The IR VARVS and 20° FLIR cases for the nominal parameters will be used for this purpose.

Parameter		IR VARVS	10° FLIR	20° FLIR	40° FLIR
Number of Scan Lines		525	525	525	525
Light Level	(fL)	10	10	10	10
Lens Blur	(microns)	16	16	16	16
Display Blur	(microns)	50	50	50	50
Detector Size	(in.)	0.001	0.001	0.001	0.001
Bandwidth	(Mc)	–	–	–	–
F/No.		2.0	2.0	2.0	2.0
Altitude (Nominal)	(ft)	1500	1500	1500	1500
Velocity (Nominal)	(ft/sec)	840	840	840	840
Slew Period (Nominal)	(sec^{-1})	0.3	0.3	0.3	0.3
Glimpse Time	(sec)	0.25	0.25	0.25	0.25
Resolution	(mr/cycle)	0.925	0.436	0.877	1.81
Focal Length	(mm)	50.8	101.6	50.4	74.4

GP78-1118-1

Figure 30 System parameters

On Figure 31 the model probability of detection outputs are plotted as a function of the lateral coverage for various cue densities. Lateral coverage values for 90% probability of detection are extracted. These plus those from similar plots for other depression angles are used to plot Figure 32. Using this curve, optimum depression angle can be determined based on lateral coverage. In the sample case the optimum depression angle is about 14°. The lateral coverage at this depression angle will be used as a figure of merit of the system. For the conventional FLIR a similar procedure is used except the computer selects the 90% probability automatically. Therefore, the first step is to make a depression angle plot shown in Figure 33. Here some explanation of the shape of this plot is in order. First one must remember that the depression angle is depression of the sensor's optical axis and bears no strict relationship to the actual range where the observer elects to search. As discussed in Appendix C, the observer will use only the portion of the display that presents suitable quality to insure a reasonable probability of target acquisition. It is therefore possible that the same "useable" footprint will be available to the observer over a range of depression angles. When the depression angle outside of the optimum range is chosen, the useable search area will be cut off by the sensor format edge. This explains the sudden rise and drop in performance at both low and high depression angles. The performance curves indicate a subtle increase in acquisition performance as the depression angle goes from 20° to 3°. This trend is especially apparent for the lower target densities. The increase in

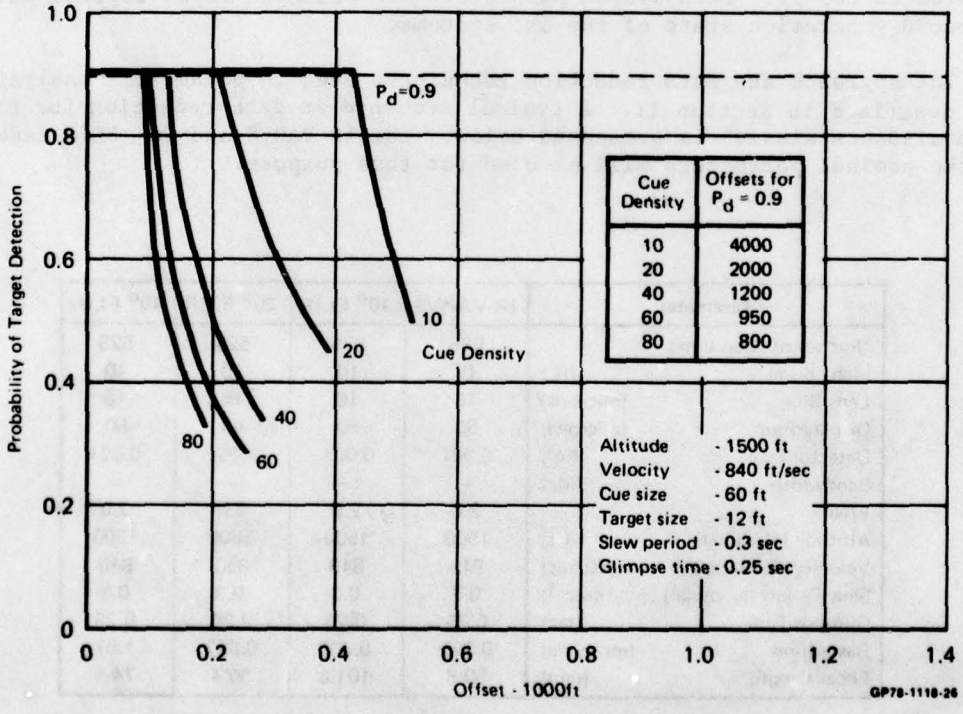

Figure 31 IR VARVS probability of detection for 14° depression angle

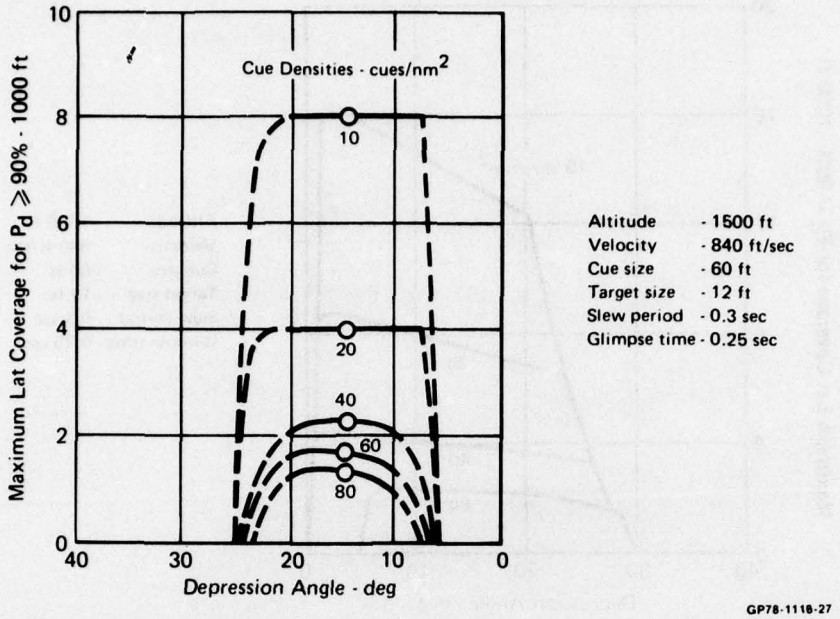

Figure 32 IR VARVS dynamic coverage capability vs depression angle

performance with shallower depression angles is primarily a function of the increased sensor ground coverage. The larger footprint size increases the time available for search and results in less sensor slewing. The longer slant range will tend to decrease ground resolution but in the 20° FOV FLIR case shown, the net effect results in an increase in the performance measure. This phenomenon will be used later to select the minimum weapons delivery range. The effect of depression angle is not as pronounced as the field-of-view gets wider.

As with the IR VARVS, the peak lateral coverage is selected from Figure 33 and used as the figure of merit of the conventional FLIR. The relative performance plots are then made by dividing the VARVS peak lateral coverage by the peak FLIR lateral coverage. The results for the sample case is shown on Figure 34. If the ordinate goes above one, the IR VARVS is better than the FLIR.

The weapon delivery plots require some additional effort. Here the figure of merit is peak downrange acquisition distance and lateral coverage product. With the VARVS, the search process is forced to be near the optical axis because of acuity fall-off. Therefore the acquisition range is very near the range given by the depression angle. The actual weapons delivery range can be anywhere within the probability contour chosen for search. This contour is described in Section 2 and has nominally been found to be the 90% target detection contour. The minimum weapons delivery range therefore corresponds to the downrange distance to the aft edge of the 90% contour. Since Figure 32 shows that lateral coverage is essentially constant for the

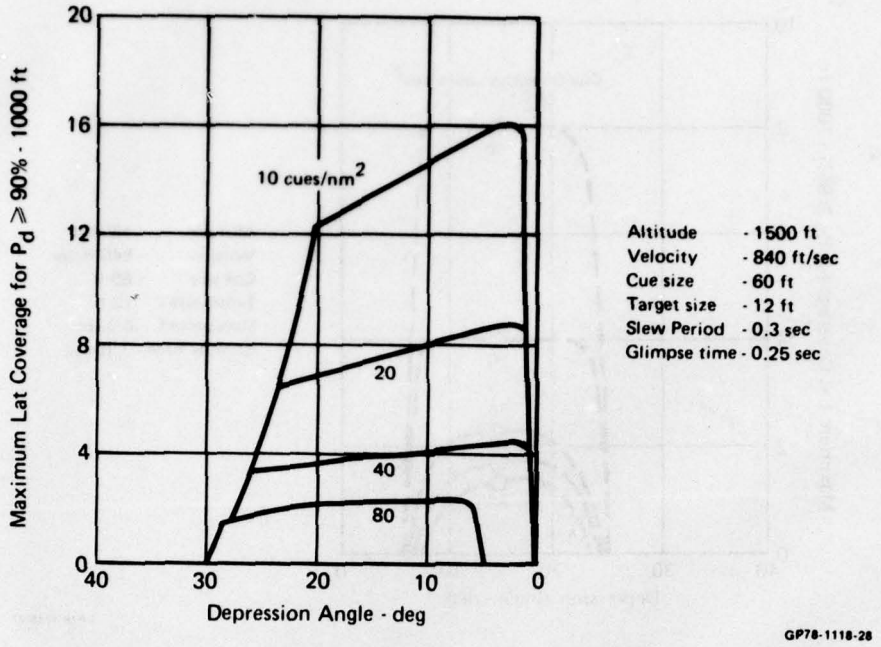

Figure 33 20° FLIR dynamic coverage capability vs depression angle

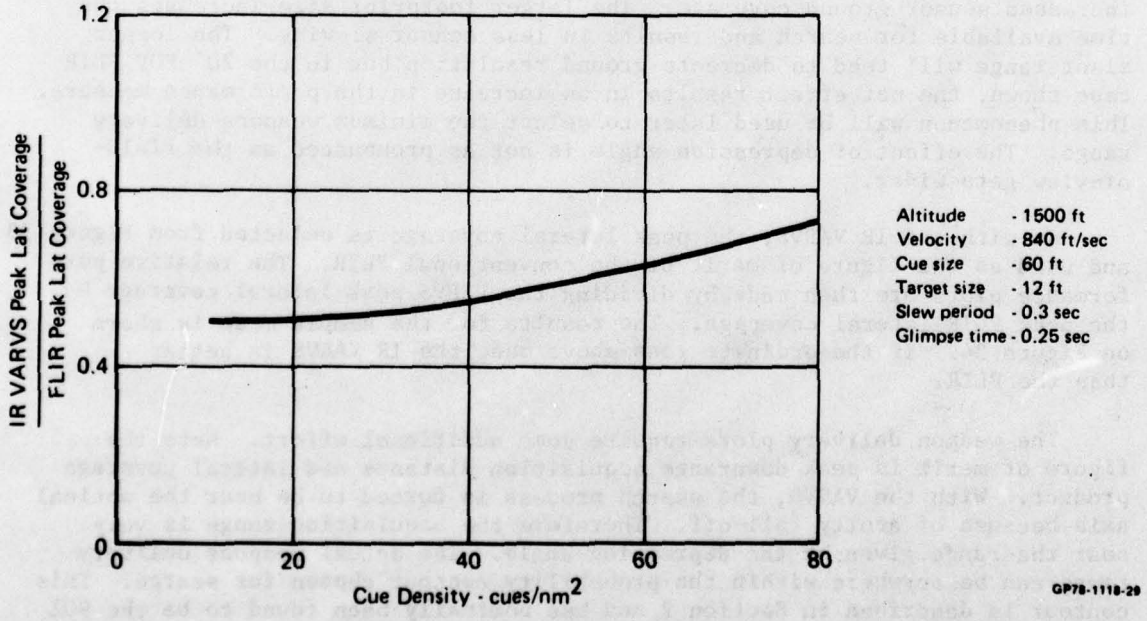

Figure 34 Relative lateral coverage performance of VARVS and 20° FOV FLIR for reconnaissance, sample case

IR VARVS, the greatest range and lateral coverage product will be at the minimum useable depression angle. The distance calculated from this angle and adjusted to correspond to the aft edge of the footprint, multiplied by the lateral coverage is the figure of merit of the IR VARVS sensor.

For the conventional FLIR, calculation of acquisition range is somewhat more difficult because lateral coverage is a function of depression angle. Fortunately, the peak lateral coverage always occurs at minimum depression angle. The maximum acquisition range is the downrange distance of the aft edge of the useable footprint at minimum depression angle. This also corresponds to maximum lateral coverage. To be compatible with the IR VARVS' figure of merit, the product of this range and the lateral coverage is defined as the figure of merit of the FLIR. For the sample case, the values are as shown in Figure 35. Figure 36 shows the curve for the sample case.

1. RESULTS

The results comparing IR VARVS to the three FLIR configurations are shown in Figures 37-44. It should be noted that all results of the parametric analyses are at the target detection level rather than recognition. This is because recognition was found to be either impossible due to lack of resolution or not practical because of the short range required. All of the systems studied would need auxiliary optics to achieve a good recognition capability. The linear FLIRs would require a narrower field-of-view or zoom optics while the VARVS would need an auxiliary optical system with five to ten times more magnification. Such a system is discussed in Section 6.

Sensor	Depression Angle (deg)	Optical Axis Range (ft)	Acquisition Range (ft)
IR VARVS	20.5	4,000	3,500
	14.0	6,000	5,100
	10.6	8,000	7,200
	8.5	10,000	9,300
20^{o} FLIR	20.5	4,000	3,370
	8.5	10,000	5,230
	4.1	21,000	7,060
	2.0	43,000	8,510
	1.0	85,000	9,470

GP78-1118-30

Figure 35 Maximum acquisition range for weapons delivery

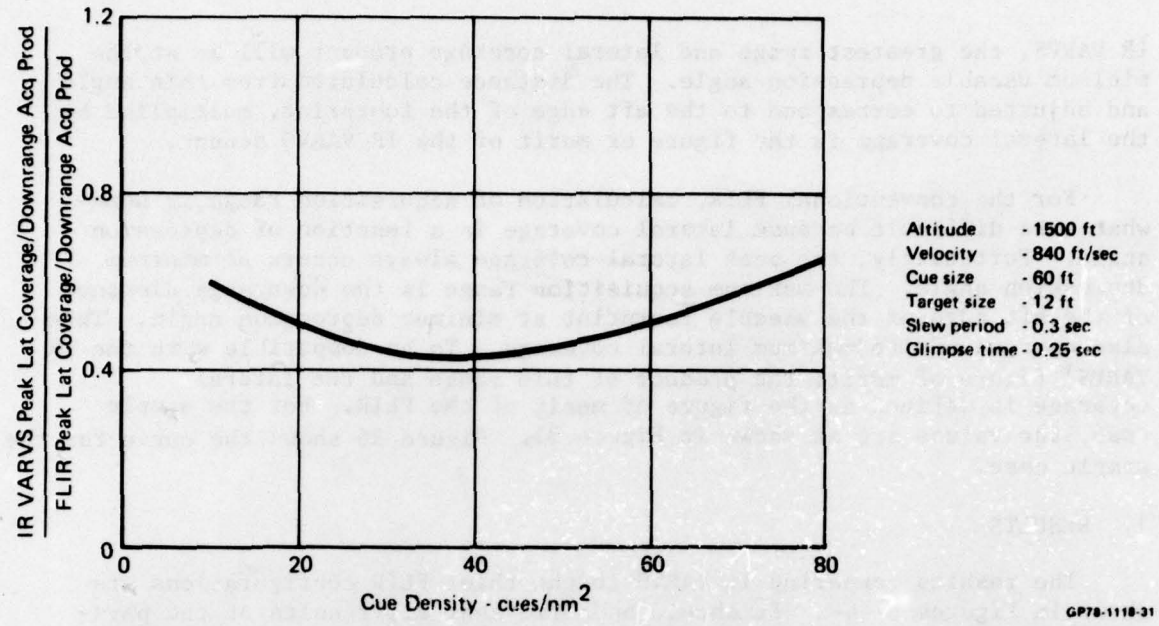

Figure 36 Relative performance of IR VARVS and 20° FOV FLIR for weapons delivery, sample case

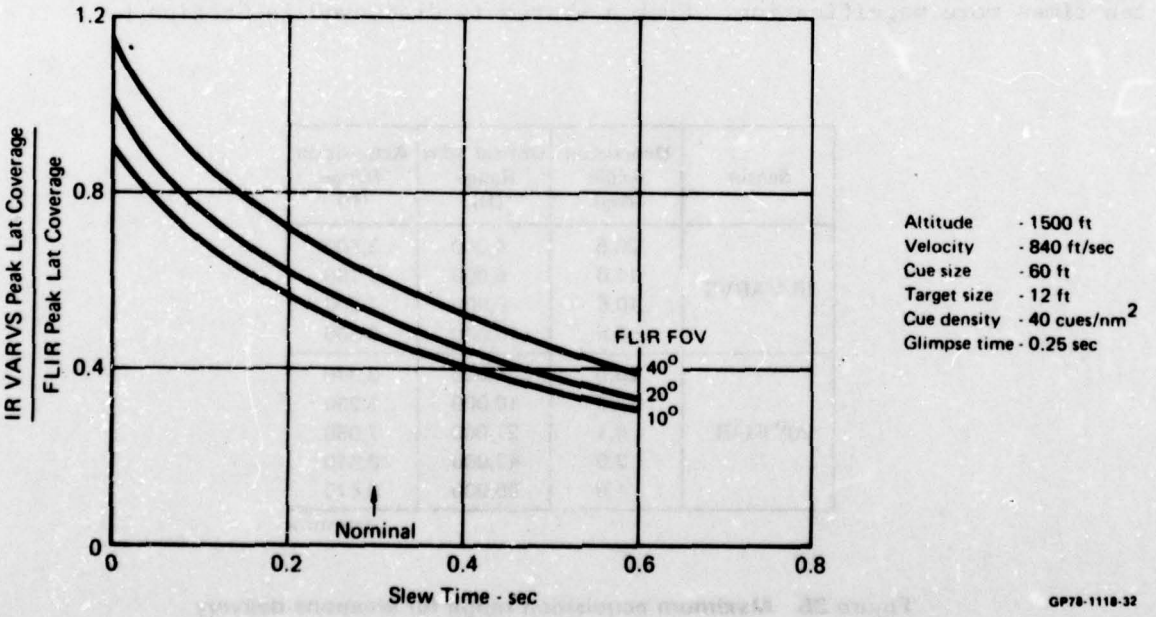

Figure 37 Relative lateral coverage performance of IR VARVS and FLIR for reconnaissance showing sensitivity to slew time

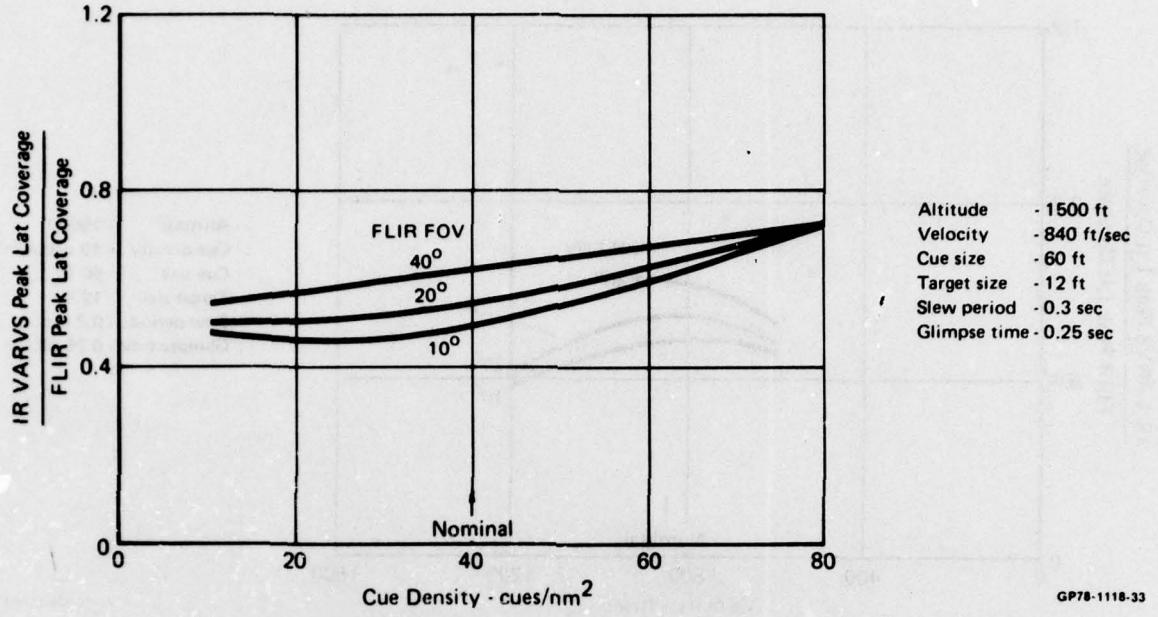

Figure 38 Relative lateral coverage performance of IR VARVS and FLIR for reconnaissance showing sensitivity to cue density

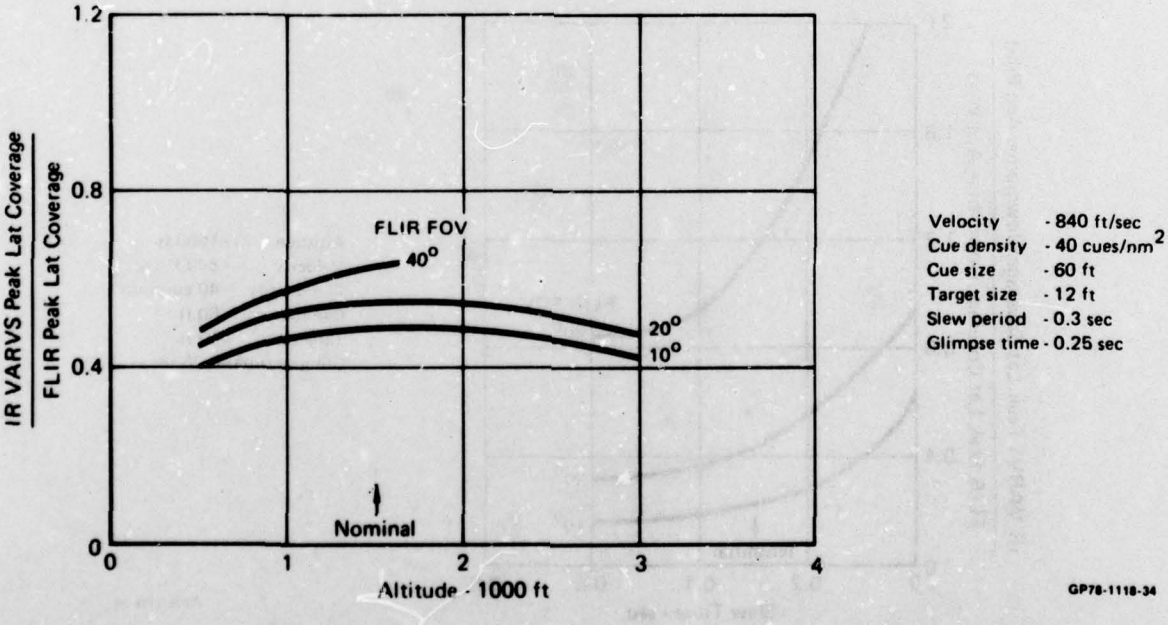

Figure 39 Relative lateral coverage performance of IR VARVS and FLIR for reconnaissance showing sensitivity to altitude

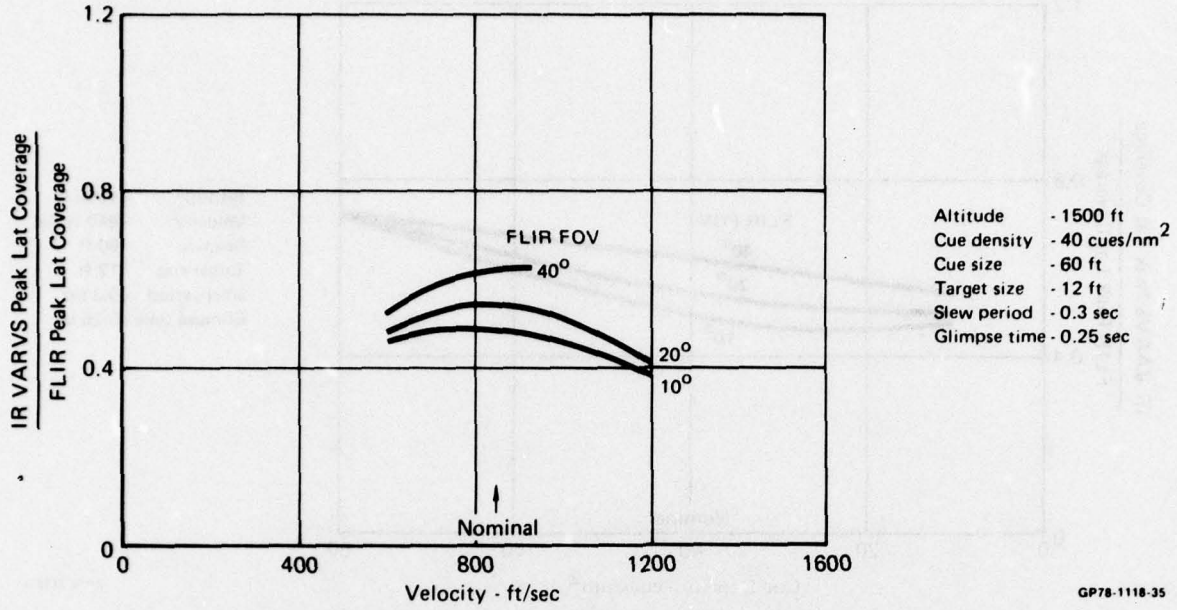

Figure 40 Relative lateral coverage of IR VARVS and FLIR for reconnaissance showing sensitivity to velocity

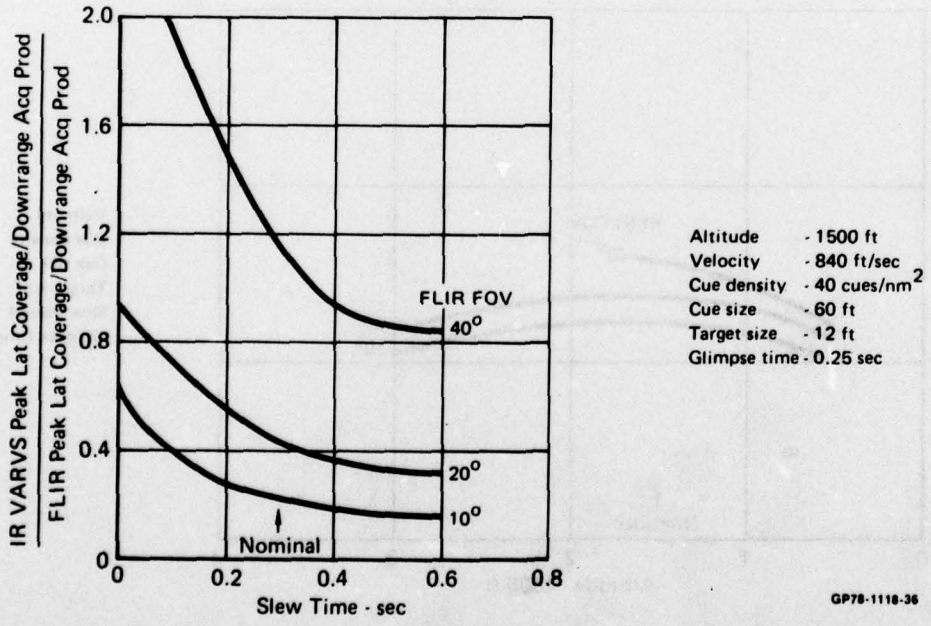

Figure 41 Relative performance of IR VARVS and FLIR for weapons delivery showing sensitivity to slew time

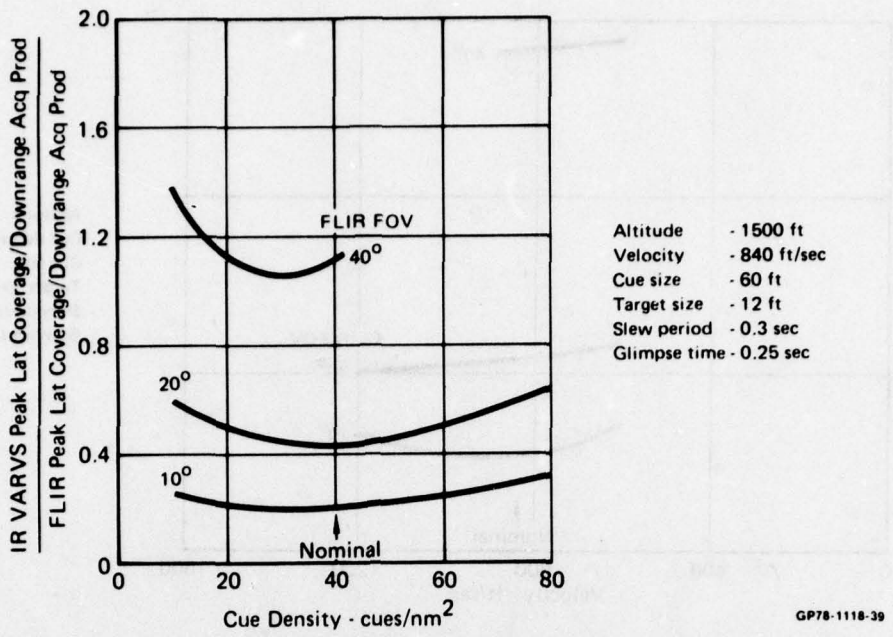

Figure 42 Relative performance of IR VARVS and FLIR for weapons delivery showing sensitivity to cue density

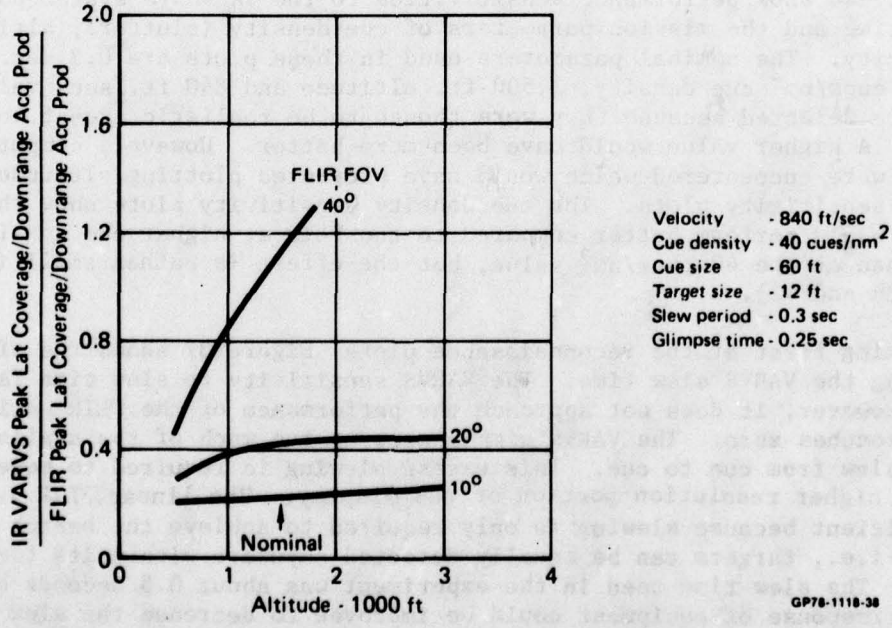

Figure 43 Relative performance of IR VARVS and FLIR for weapons delivery showing sensitivity to altitude

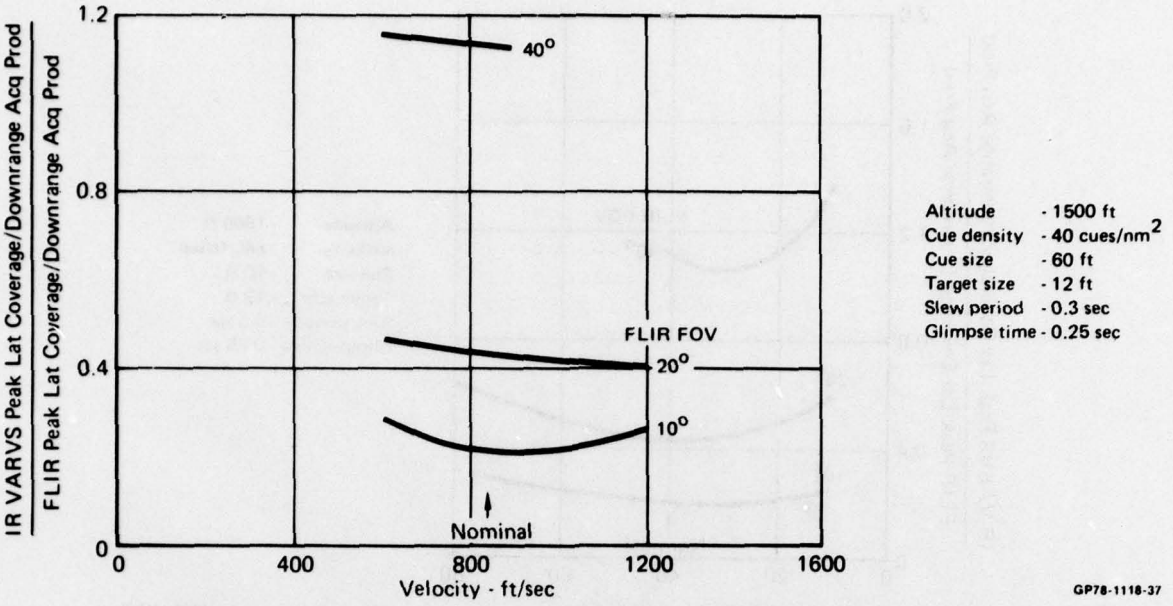

Figure 44 Relative performance of IR VARVS and FLIR for weapons delivery showing sensitivity to velocity

Figures 37-44 show performance sensitivities to the IR VARVS system parameter of slew time and the mission parameters of cue density (clutter), altitude, and velocity. The nominal parameters used in these plots are 0.3 sec. slew time, 40 cues/nm^2 cue density, 1,500 ft. altitude and 840 ft./sec. velocity. These were selected because they were though to be realistic except for cue density. A higher value would have been more better. However, computational problems were encountered which would have prevented plotting altitude and velocity sensitivity plots. The cue density sensitivity plots show that the IR VARVS would perform better compared to the FLIR at higher cue density values than at the 40 cues/nm^2 value, but the effect is rather small (Figures 34, 36, 38 and 42).

Looking first at the reconnaissance plots, Figure 37 shows the effect of varying the VARVS slew time. The VARVS sensitivity to slew time is very great. However, it does not approach the performance of the FLIR until slew time approaches zero. The VARVS simply uses up too much of the available time to slew from cue to cue. This excess slewing is required to move cues into the higher resolution portion of the display. The linear FLIR is more time efficient because slewing is only required to achieve the search area coverage i.e., targets can be equally detected anywhere within its field-of-view. The slew time used in the experiment was about 0.5 seconds but the time response of equipment could be improved to decrease the slew time to 0.3 seconds, this value was used as nominal for the parametric analyses. Theoretically, slew time could be further reduced to 0.1 or 0.05 seconds. However, eye control rather than head control would be required to realize the benefits of this improvement.

From the data of Figure 37, one can conclude that the basic head controlled IR VARVS is limited to 50-80% of conventional linear FLIR performance. With eye control this could be improved to the 80 to 100% range.

The remainder of the reconnaissance plots, Figures 38, 39 and 40 show sensitivities of the comparison to mission parameters. The cue density data, Figure 38, shows that the IR VARVS performance improves relative to the FLIR as cue density or clutter is increased. This trend occurs because at higher cue densities, multiple cues appear within the portion of the IR VARVS footprint where target detection is likely. This means that more cues can be inspected for the target without slewing the sensor. The altitude and velocity plots, Figure 39 and 40, respectively, show that the nominal parameters of 1,500 ft. and 840 ft/sec. are very near the optimum and that the IR VARVS performance reduction on either side of these points are small but significant.

The weapon delivery plots, Figures 41, 42, 43 and 44, show how the product of downrange acquisition distance and lateral coverage vary with the same sensor and mission parameters that were used on the reconnaissance curves. Here the results are somewhat different. The performance for weapon's delivery are more dependent on sensor field-of-view as shown because the curves for the 10°, 20°, and 40° systems are more widely spaced. This is a direct result of the FLIR resolution capability which affects the probable target acquisition range. In the weapon delivery case, the IR VARVS performance exceeds that of the 40° FLIR for the nominal mission parameters. On the other hand, the VARVS has only 40% of the performance of a 20° FLIR which has similar resolution capability. The VARVS is even less effective than a 10° FLIR. This is because lateral coverage capabilities are comparable (Figure 37-40) while the acquisition range is much greater for the higher resolution 10° TV.

SECTION V

OPTIMUM PARAMETER DISCUSSION

The thorough knowledge of the VARVS gained from the theoretical and experimental studies described herein makes the path clear to achieve optimum performance from the system. The rationale develops as follows.

The analyses shows that two routes exist to improve VARVS performance, by reducing slew time and/or increasing the size of the high resolution area of the final displayed image. Decreasing slew time will make search more efficient by making more slews possible while increasing the high acuity area requires fewer slews. There appears to be a tradeoff here. However, reference to the parametric analysis, Section 3, provides some interesting observations. By reducing the slew time to zero, Figures 37 and 41 show that VARVS performance equals the 20° linear sensor. When one realizes both sensor types have identical on-axis resolution performance, broadening the on-axis acuity will increase performance until the point of uniform acuity across the entire visual field is reached. We would then have a conventional linear sensor. If a linear sensor has target acquisition performance equal to the VARVS, then the VARVS advantage must lie elsewhere, perhaps for flight control and navigation where the advantages of a wide field-of-view is clear.

If one accepts the value of the wide field, the alternate route of improving target acquisition performance of the VARVS must be persued. The data shows that slew time must be reduced to a fraction of the glimpse time in order to achieve performance comparable to a conventional linear sensor. Slew times on the order of 0.01 to 0.03 sec. would be required by eye control to achieve the required performance. This would be a major technical task. Perhaps a better way, made possible by advancements in solid state array technology, would be to use a wide field linear lens with a focal plane array capable of supporting high resolution anywhere within its field-of-view. The variable acuity would then be obtained electronically by sampling the array in the proper manner. The high speed eye controlled slewing could then be handled electronically in a field time of 0.017 sec. With this capability, the mechanical sensor slewing would then only have to follow much slower head motion. The focal plane array required by this approach would be about 10000 x 10000 elements. Detector elements would have to be very small, no more than 0.0003 inches to produce a reasonable array size of 3 inches square. The display would require similar performance (10,000 lines) and be helmet mounted to support this approach. Such a system must await sensing and emitting array state of the art advancements.

SECTION VI

DUAL FIELD FEASIBILITY STUDY

Analyses of Section V have documented IR VARVS performance to be in the 0.8-1.0 milliradian area. This is suitable for target detection but is unuseable for target recognition tasks. For the recognition task, according to the Johnson Criteria, about 5x magnification would be required so that the target subtends an adequate number of lines.

Since the wide angle optical quality is not sufficient to support this performance, a separate optical system must be considered. Such an approach that uses a common aperture is shown in Figure 45. Here the front element of the wide angle lens is common with narrow field-of-view high resolution optical system. The wide field optical system is that described in Reference 2 which is believed to be the optimum design for an IR VARVS. The low optical power of the large front element to nearly paraxial rays makes possible its use as the first element of a long focal length high resolution optical system, providing that the small optical deviations introduced by the aspheric element can be corrected outside of the optical path occupied by the wide angle optical system. This is the function of the corrector element shown on Figure 45. The feasibility of this corrector and remainder of the narrow field optical system is described below.

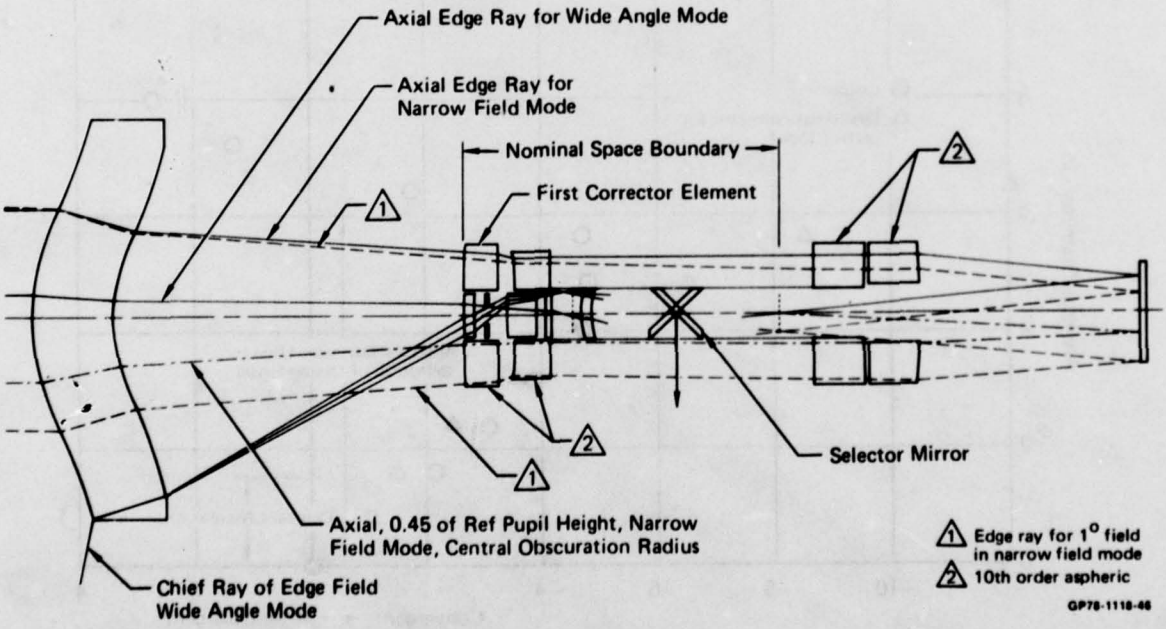

Figure 45 Common aperture VARVS

1. INPUT PARAMETERS

The first step to establish the feasibility of a narrow field optical system for the VARVS is to quantify the angular distortions introduced by the front element. From this data the useable aperture can be determined which in turn establishes the theoretical resolution limit of the narrow field systems. To accomplish this, a paraxial meridional ray fan covering the entire lens clear aperture was traced through the front element of the IR VARVS lens.

The angular deviation of the ray fan is plotted in Figure 46 and are denoted by circles. Note that the optical power is convergent out to about 7 inches of clear aperture. Theoretically this should be correctable. However, the reversal in ray angle that occurs at about 5 inches clear aperture diameter would probably create serious optical aberrations. For this reason we chose a maximum aperture of 5.5 inch. In order to gain some insight into the practicability of correcting the deviations shown in Figure 46, the angular deviation required at the corrector surface to produce perfect focus at the desired focal length were computed and are plotted in Figure 46 against the aperture diameter where the rays originate. These are denoted by the triangles. These data show the corrector shape to be easily realizable over the desired aperture. This aperture theoretically established a diffraction limit on resolution of about 0.1 milliradian. The desired resolution is 5 times better than the wide field system. In

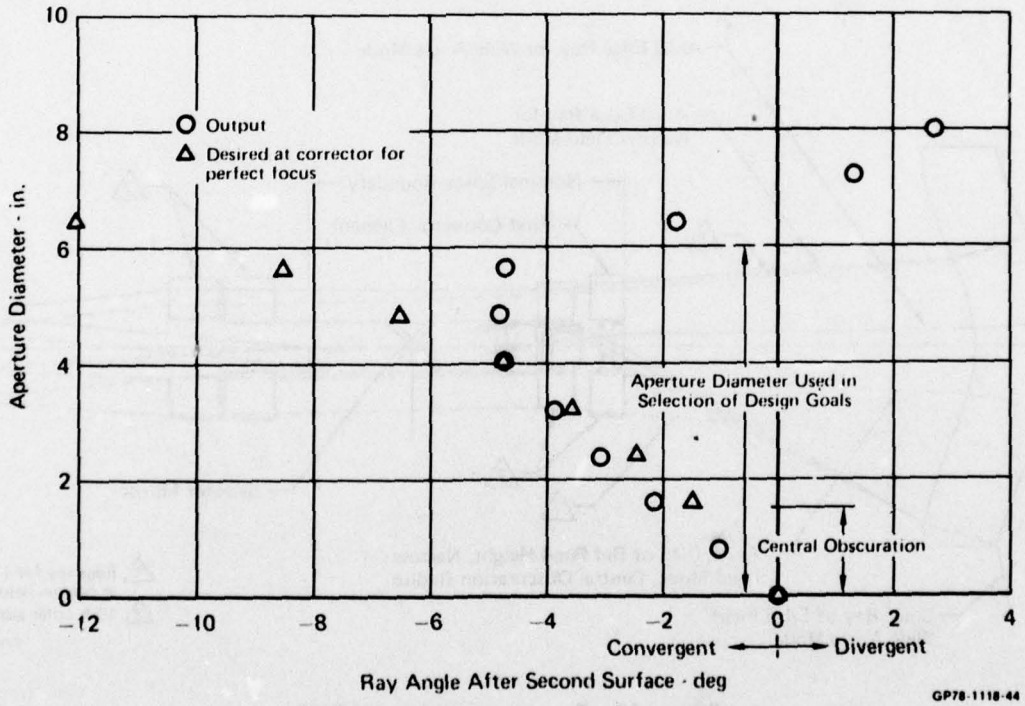

Figure 46 Optical characteristics of the front element for paraxial rays

Section V the wide field system yielded a threshold resolution of about 1 cycle/milliradian which represents a discrete angular resolution of approximately 0.6 milliradian. The desired narrow field resolution is therefore about 0.12 milliradian. This value is compatible with the aperture diameter limit discussed above. Using 0.12 milliradian as a resolution goal, the field-of-view and focal length requirements can be calculated if image size is defined. In order to use a common scanner for both wide and narrow fields-of-view, both image sizes must be identical. This size has been established in the study of Reference 2 is 0.72 inches. The field-of-view and focal length are calculated as follows: If 0.12 milliradian resolution is desired, the detectors must have an angular separation(α) of less than about

$$\alpha = \frac{\text{Resolution Desired}}{\text{Kell Factor}} = \frac{0.12}{1.4} = 0.086 \text{ mr} \tag{28}$$

If 488 effective scan lines are available, the field-of-view (θ) will be

$$\theta = .086 \times 488 = 42 \text{ mr}$$
$$\theta = 2.4°$$

The focal length (f) is therefore

$$f = \frac{\text{Image Size}}{\text{Field-of-view}} = \frac{0.72}{0.042} = 17.14 \text{ inches} \tag{29}$$

In order to allow some margin for error, this was increased to 20 inches which yields a 2° field-of-view.

Another requirement for the common aperture system is that the optical output be compatible with common modular scanners. Again utilizing experience gained in the wide field feasibility study (Reference 2), space must be provided identical to that optical system and is as shown in Figure 45.

2. OPTICAL DESIGN

Having looked at the wavefront exiting from the first element, the initial design approach was centered on the concept of correcting the errors introduced by the first element with another spline element (called a corrector) which would collimate the energy, and then to focus this recollimated wavefront with a classical NFOV IR design. Initially a 20 inch focal length parabola was used for the latter. Some work on this approach made it evident that the corrector power required to recollimate the wavefront was a detriment to performance. The paraxial focal length of the first element is 21.68 inches. Because this power is similar to that expected of the final design, the initial approach using a parabolic reflector was discontinued, the reflector was removed from the lens prescription and optimization continued using the first element for power and the corrector as a zero power component functioning to "clean-up" the wavefront.

While working with this two element configuration and optimizing the corrector, relationships began to be established between angular resolution, aperture diameter and corrector complexity (i.e., number of splines per surface). These relationships are shown in Figure 47. These data show on-axis resolution of 0.16 milliradians was obtainable out to a 3.5 inch aperture. At 5 inches of aperture, resolution degraded to 0.47 milliradians. Figure 46 shows a rapid change to front element angular error in the 4-5 inch aperture region. Therefore, it is very possible that not enough splines were used in this region. Five splines per surface are the maximum available in our design program.

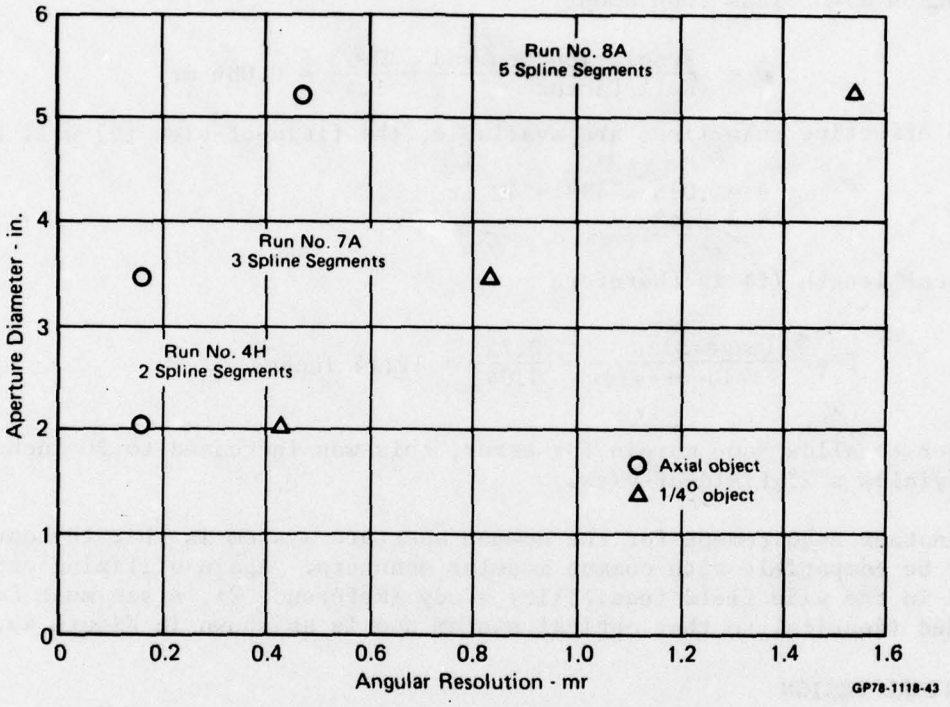

Figure 47 Optical performance of early design long focal length lens

We verified this by using another commercial optical design program (ACCOS V) which is not limited to number of splines per surface. This program was able to correct a 5.5 inch aperture. However, the program had continuity control problems when operating in the optimization mode. It only worked properly for rays passing through the center portion of the splines and not the end points. For this reason we abandoned ACCOS V for spline corrector element design. Figure 48 shows a significant resolution drop with field angle. This indicates that a more complex optical design will be required. To study this, lens elements were added after the corrector and the field-of-view increased to 2 degrees for optimization of off-axis imagery. The starting design after reoptimizing the axial blur is noted as RN11 on Figure 48. The angular blur or resolu-

tion of this configuration operating with a 5.5 inch aperture is shown in Figure 48 for zero and 1° field angles. The points designated as RN19 are the result of several design runs for optimization of the off-axis blur. RN26 is the result of further work with the prescription directed at reduction of the size of the central obscuration.

To gain more correction, lenses were added in the region of the image plane, resulting in the design which has produced the greatest overall resolution (RN27). However, this design as it now stands, requires an increase in track length between corrector and image to provide adequate room for folding. Also the focal length of this design is 10.57 inches which is too short for a field-of-view of 2°. Further work is being done to increase the track length and the focal length. The aperture ratio will be approximately 4.0 when the desired focal length is obtained.

The ACCOS V lens design program was used in a parallel optimization effort. The first element (common to the wide angle system) is entered in the prescription as a spline and is not a variable. As long as the spline is not varied, ACCOS V does not have the continuity control problems mentioned earlier. The best design from ACCOS V as of this report is SPL 25. This design is the narrow field-of-view system shown in Figure 45. All eight surfaces in the relay system are aspheric, four carrying deformation coefficients. The performance data on this design for comparison with the spline corrector system is plotted in Figure 48. This design at

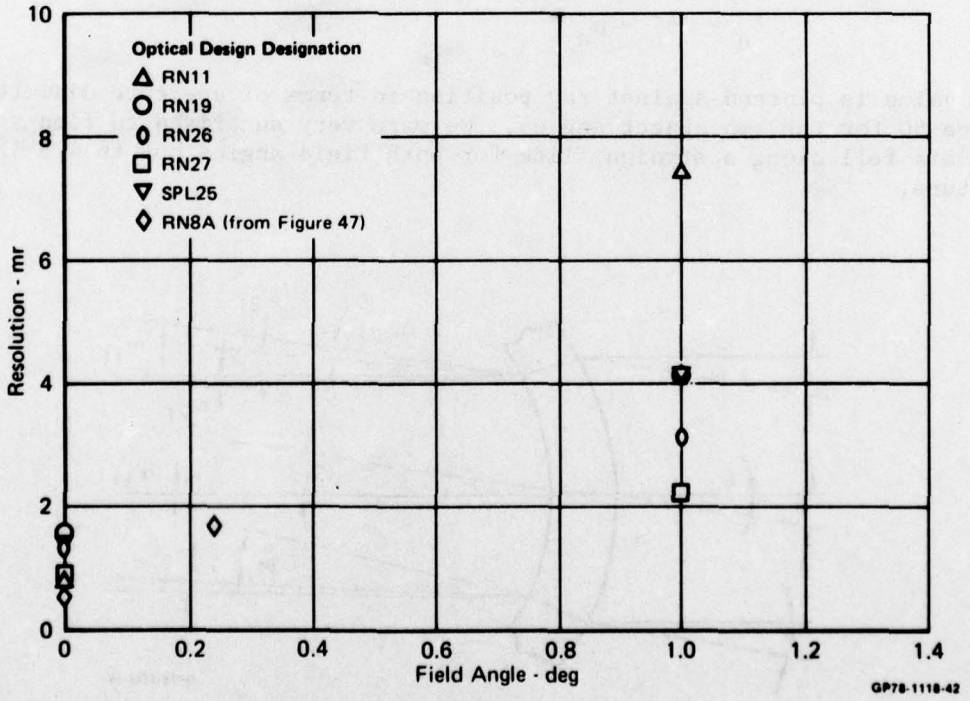

Figure 48 Comparison of optical designs

present is monochromatic at 12 microns. Spectral correction is not expected to be a problem based on the work with the spline program. The central obscuration diameter of this design is 2.5 inches and is defined by the lens element nearest the folding mirror. The aperture stop needs to be moved inside the first element and located at the first corrector surface.

By plotting the data of Figure 47 for the same aperture (RN8A) on Figure 48 it is clear that optimizing for the 1° field angle has reduced on-axis performance well below our requirements. Furthermore, any optimization effort aimed at improving off-axis performance causes a corresponding reduction of on-axis performance and vice versa. For this reason, the design work was terminated and an investigation was begun to find the reason for the low performance. The source of the problem was found to be the wavefront aberrations introduced by the spline surfaces of the first element. The corrector can accurately correct these for one object angle but some compromise must be made for other object angles. It is clear that either aperture diameter or field angle must be reduced to obtain satisfactory performance. To study this the angular relationships introduced by the first element were determined for on-axis and off-axis conditions. This was accomplished by tracing collimated meridional ray fans each containing 21 rays through the element at 0, 1/4° and 1° object field angles as shown for greatly exaggerated angles on Figure 49. These data were used to compute the amount an off-axis ray is deviated relative to the same ray on-axis. For any ray n:

$$\delta_n = \Delta\theta'_n - \alpha'_n \tag{30}$$

This value is plotted against ray position in terms of aperture diameter in Figure 50 for the two object angles. We were very surprised to find that the data fell along a straight line for both field angles out to 4.8 inch aperture.

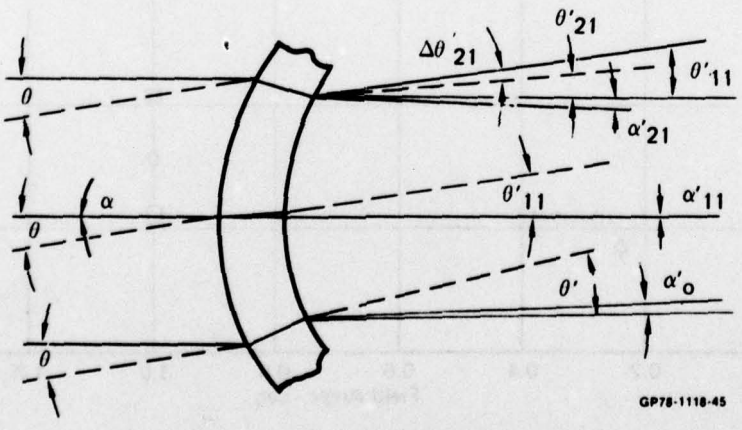

Figure 49 Exaggerated first element ray trace

Had the points deviated from a smooth curve by an amount exceeding the system angular resolution requirement corrected for the effects of the down-stream optical elements required to give the correct focal length, optical design would be clearly impossible. The adjusted tolerance is shown on Figure 50. All points fall within the tolerance out to 4.8 inch aperture. While the linear buildup in ray deviation with aperture is encouraging, this does not necessarily mean design is possible.

The slope of the curves on Figure 50 are an indication of the degree of aberration produced by the optical element. An aberration free 2° field-of-view optical element would produce the nearly vertical dashed line on Figure 50. The difference between this and our lens is very large. This indicates very large aberrations and is probably the source of our design difficulty. Nevertheless we feel the linear build-up in aberrations with aperture diameter should make them correctable. As an example, rays through a meniscus lens with the same focal length as our lens are shown on Figure 50 for a 1° field angle. This curve compensates with conventional spherical optics.

However, because of time constraints we had to terminate the effort at this point and intend to continue this independently.

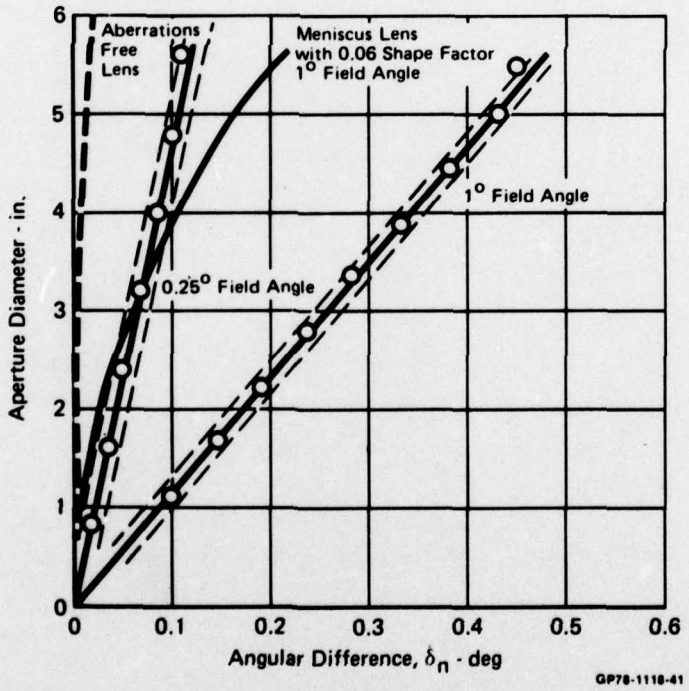

Figure 50 Optical errors for 0.25° and 1.0° rays

3. SUMMARY

As of this report, we have not been able to obtain an optimized design for the narrow field-of-view case which meets the resolution goals. However, considerable insight has been gained into the design problems and we are reasonably confident that a narrow field optical system can be added to the VARVS. However, aperture constraints will probably limit its resolution to approximately 0.2 milliradians.

APPENDIX A

APPLICATION OF THE NIGHT VISION LABORATORY (NVL) THERMAL VIEWING SYSTEM STATIC PERFORMANCE MODEL TO THE VISUAL SPECTRUM VARVS

It was suggested that the NVL Thermal Viewing System Static Performance Model be used to evaluate the performance of the Remote Viewing System (RVS). However, repeated attempts to convert the RVS parameters directly to the NVL model have led to the following problem. The radial distortion function of the foveal lens does not lend itself to an MTF analysis as a function of object field angular spatial frequency as called for in the NVL model. All parameters can be converted successfully except for the scan velocity term because a linear raster scan on the lens image plane will create a variable angular velocity and variable direction scan in the object field. This is depicted in Figure A-1. Extreme complexity results when attempts are made to convert spatial into temporal frequency. This is illustrated by the rotation of the f_x bar pattern in the lens image plane shown in Figure A-1. Given enough time, an analysis could be made in a manner compatible with the NVL model. However, the analysis is much simpler if performed, not in object field angular frequency (cycles/milliradian) but in spatial frequency terms (lines/millimeter). For our purpose of optimizing the RVS lens, it is simpler to work in terms of spatial frequency on the foveal lens focal plane.

This simplicity arises because seven of the nine MTF's are independent of object field angle at this foveal lens focal plane location, and the scan velocity is undirectional and uniform at this location, thereby making easy conversions from spatial to temporal parameters. The only non-linear conversions necessary are simple geometrical ones which translate from focal plane to object field and display space. The advantages of working in the spatial frequency terms will become clear as the analysis is developed. In the following development, the NVL model approach will be used precisely but will be applied in the foveal lens focal plane as a function of linear spatial frequency (1/mm). Parameters will be covered in the same order as they are in the NVL Report (4), which describes the model in detail.

1. MTF'S

a. Optical MTF

The optical MTF's consist of a diffraction MTF and a Gaussian MTF.

(1) Diffraction

In angular terms, the diffraction MTF is reference as Equations (9) and (10) of the NVL report:

$$H_{opt}(f_x,\theta) = \frac{2}{\pi}\left[\cos^{-1} A - A(1 - A^2)^{1/2}\right] \qquad \text{(A-1)}$$

where $$A = \lambda F_{\#} f_x / L(\theta) \qquad \text{(A-2)}$$

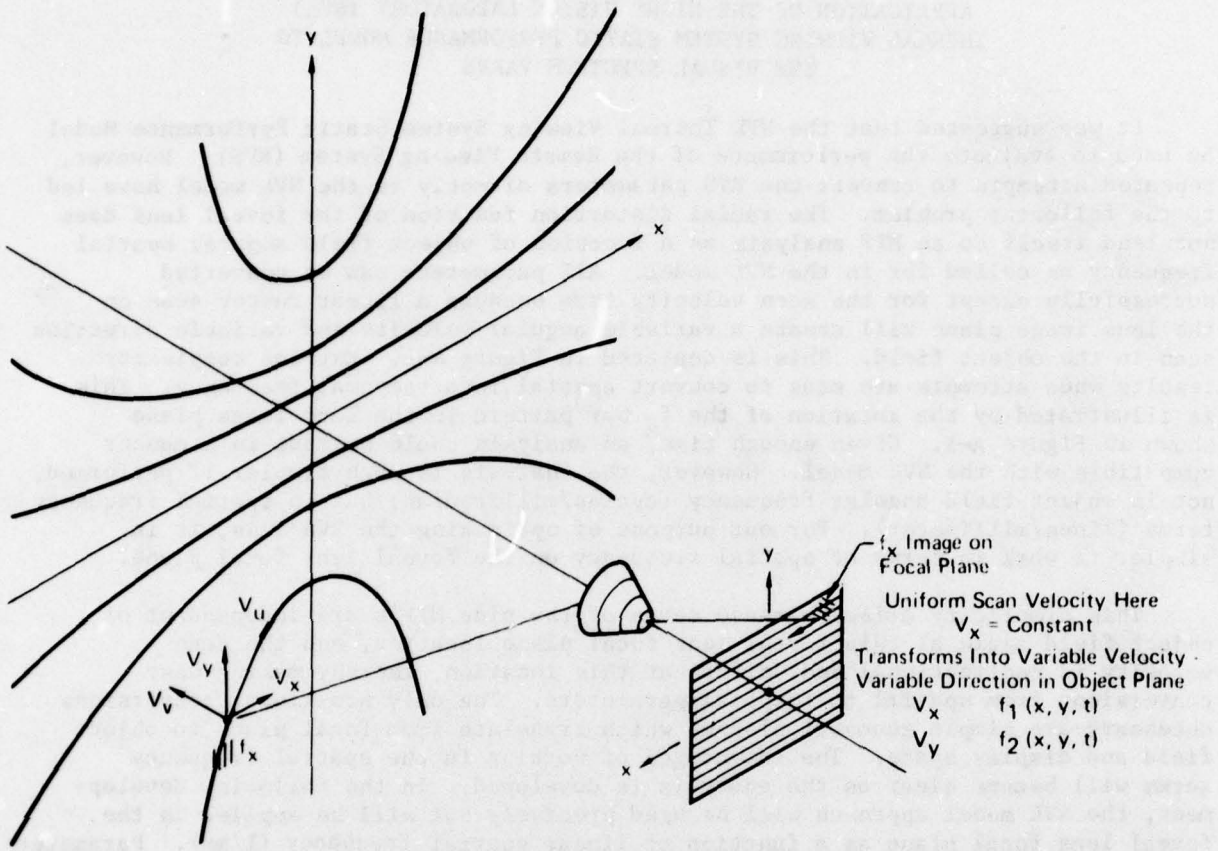

GP76-1037-109

Figure A-1 Scan distortion introduced for foveal lens

where $L(\theta)$ is the equivalent focal length which changes over a 50/1 range as object field angle θ changes. The angle θ is the absolute angle between the point of interest and the lens optical axis. At the foveal lens image plane

$$S_x = \frac{f_\mu}{L(\theta)} \tag{A-3}$$

where S_x is the image plane spatial frequency and f_μ is its object field angular equivalent measured along the scan line projection in the object field (μ direction on Figure A-1). Solving for f_μ in Equation (A-3) and substituting this for f_x in Equation (A-2).

$$A = \lambda F_{\#} S_x \tag{A-4}$$

Since the F/number of our lens is constant, the diffraction MTF is no longer a function of object field angle. Thus we may write $H_{opt}(S_x)$ which indicates that the MTF is a function of the independent variable S_x only. Note, however,

that conversion to object field angular spatial frequency is very simple because focal length is constant over small angular increments and may be determined from

$$f_{\mu} = S_x L(\theta) \tag{A-5}$$

where μ is along the scan line projection in the object field

likewise

$$f_w = S_y L(\theta) \tag{A-6}$$

where w is normal to the scan direction in the object field

(2) Blur

A similar simplicity exists here. The MTF equation with the angular term b of Equation (11) of Reference (4) replaced with its equivalent is:

$$H_{blur}(f_x,\theta) = \exp\left[-\frac{2\pi^2\sigma^2}{L(\theta)^2} f_x^2\right] \tag{A-7}$$

The foveal lens inherently has a constant spatial blur over its entire focal plane, so that the sigma (σ) of Equation(A-7)is a constant. Substituting Equation(A-5)into (A-7) we see the blur MTF simplifies to

$$H_{blur}(S_x) = \exp\left[-2\pi^2\sigma^2 S_x^2\right] \tag{A-8}$$

Thus this MTF like the diffraction MTF, is no longer a function of object field angle because the focal length variable has been removed.

b. Detection MTF

The spatial filter MTF of the detector is defined as:

$$H_{Det}(f_x,\theta) = \frac{\mathrm{Sin}(\pi f_x \Delta x)}{\pi f_x \Delta x} \triangleq \mathrm{Sinc}(f_x \Delta x) \tag{A-9}$$

It is also complex in our system because the angular projection of the detector into the object field (Δx) in this equation varies with absolute object field angle (θ). Since the detector height is still uniform at the lens focal plane, shown in Figure(A-2)as Δh, Equation(A-9)can be restated as:

$$H_{Det}(S_x) = \frac{\mathrm{Sin}(\pi S_x \Delta h_x)}{\pi S_x \Delta h_x} \tag{A-10}$$

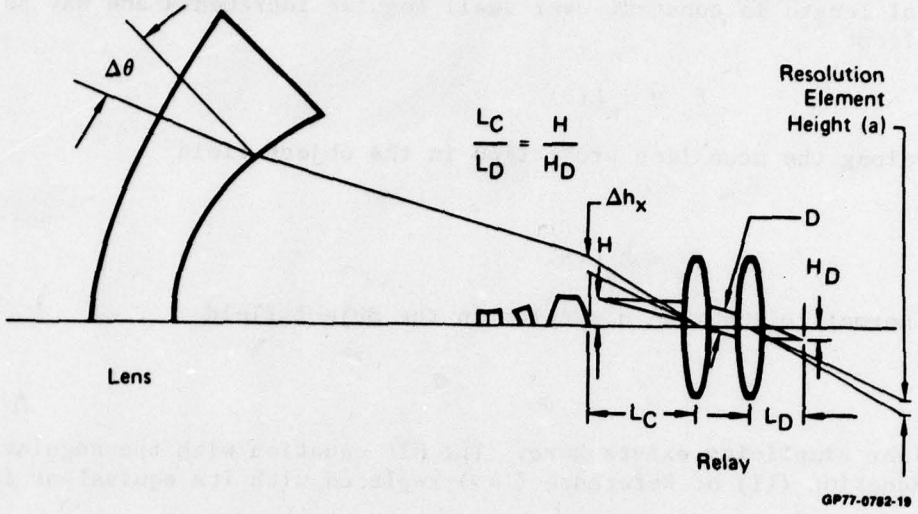

Figure A-2 Optical relay parameters

Again the MTF becomes independent of object field angle. Note from Figure (A-2) that the detector height (Δh_x) is a function of detector size(a), detector system focal length (L_D), and relay focal length (L_C), viz:

$$\Delta h_x \simeq a_x \frac{L_C}{L_D} \tag{A-11}$$

If the detector characteristics are known, the focal lengths are a function of detector size (Δh) projected unto the image plane as shown in Figure (A-2). Detector size Δh can be computed directly from either the on-axis resolution required, the number of scan lines required across the vertical FOV, or bandwidth/response restrictions and frame rate requirements. The focal lengths, L_C and L_D, are then selected to make the detector dimension appear as the required Δh at the foveal lens focal plane.

MTF becomes:

$$H_{Det}(S_x) = \text{Sinc} \frac{a_x L_C}{S_x L_D} \tag{A-12}$$

Again this MTF is independent of object field angle.

c. Detector Electronics MTF

It is in the MTF, the detector electrical response, that we get into real trouble trying to work in object field angular space. For a conventional linear optical system, a linear detector scan velocity converts into a scaled but linear angular scan in the object field. This is not true in our system as was shown in Figure A-1. A linear scan in the x direction on the image plane results in angular velocities in both θ_x and θ_y directions in the angular object field. Both of these angular components are nonlinear functions of both x and y position on the image plane. Thus, converting from spatial frequency to temporal frequency becomes very complex. All of this can be avoided by working in linear spatial plane terms. If the scanner has an angular scan velocity β, then the linear motion of the instantaneous FOV on the foveal lens image is

$$V_x = \beta L_C \tag{A-13}$$

The conversion to temporal frequency (f) is therefore

$$f = V_x S_x \tag{A-14}$$

This is a constant conversion and not a function of time. Therefore, all electronic MTF's of the NVL model are valid. These are

$$H'_{Det}(f)$$

$$H_{Elect}(f)$$

$$H_B(f)$$

d. Display

The RVS display is the inverse of the foveal lens, which results in a conventional linear raster generated on the CRT. The CRT has a constant spot size and the expansion optics has a constant blur at the object focal plane. Again this MTF, if derived in the linear spatial plane, will not be a function of object angle. If the optical blur and CRT spot size are combined and assumed to have a Gaussian MTF, a composite sigma (σ_d) results and the MTF is:

$$H_{Disp}(S_x) = \exp\left[-2\pi^2 (r\sigma_d)^2 S_x^2\right] \tag{A-15}$$

where r is the physical ratio of format sizes; viz

$$r = \frac{H_{LENS\ IMAGE}}{H_{DISPLAY\ CRT}} \tag{A-16}$$

By contrast, if this were accomplished in the object angular plane, the MTF would be much more complex, viz

$$H_{Disp}(f_x,\theta,M) = \exp\left[-\frac{2\pi^2(r\sigma_d)^2 f_x^2}{L(\theta)^2 M^2}\right] \quad \text{(A-17)}$$

where M is any system angular magnification from object field to the viewer. Again the simplicity is obvious.

e. & f. Stabilization and Eyeball

The remaining two MTF's are the only two that are not simplified by working in linear spatial rather than angular terms. First, stabilization tends to be angular input to the system. Using the MTF from the NVL report:

$$H_{Los}(f_x) = \exp(-Pf_x^2) \quad \text{(A-18)}$$

Converting to the foveal lens image plane results in

$$H_{Los}(S_x,\theta) = \exp\left[-PS_x^2 L(\theta)^2\right] \quad \text{(A-19)}$$

Similarly, the eye views the display in angular terms. The NVL MTF is

$$H_{Eye}(f_x) = \exp\left[-\frac{\Gamma f_x}{M}\right] \quad \text{(A-20)}$$

Equation (A-20) must be converted to the foveal lens image plane

$$H_{Eye}(S_x,\theta) = \exp\left[-\frac{\Gamma S_x L(\theta)}{M}\right] \quad \text{(A-21)}$$

In conclusion, seven MTF's have been simplified at the expense of two that have been made slightly more complex by the conversion to linear spatial frequency.

2. NOISE EQUIVALENT MODULATION (NEM)

For visual spectrum applications noise equivalent modulation must replace NEΔT in the NVL model. In the visual model, the primary noise source is the detector which is a silicon vidicon. Its NEM was extracted from data of Reference (7). These data show vidicon S/N as a function of faceplate illumination for a specific bandwidth. The basic function is approximately

$$\frac{\text{Peak-to-peak signal}}{\text{noise (rms)}} = 100\,E \quad \text{(A-22)}$$

where E is faceplate illumination in LUX. The noise equivalent signal is (signal input that just equal noise)

$$NEM = \frac{\text{noise}}{\text{signal}} = \frac{1}{100E} \quad \text{(A-23)}$$

assuming that the noise is proportional to the square root of the bandwidth

(Δf) of $4(10^8)$ Hz. For data given:

$$NEM = \frac{\Delta f}{100E \quad 4X\ 10^6} = 5 \times 10^{-6} \frac{\Delta f}{E} \text{ (E in LUX)} \qquad \text{(A-24)}$$

For E in footcandles:

$$NEM = \frac{4.64 \times 10^{-7}}{E} \Delta f \text{ (E in Foot-Candles)} \qquad \text{(A-25)}$$

The faceplate illumination can be calculated from system geometry as follows:

$$E_f = \frac{B T_a T_o}{4 F^2_{No}} \qquad \text{(A-26)}$$

Where

B = Scene brightness in footlamberts

T_a = Atmospheric transmission

T_a = Optical transmission with sensor

F_{no} = The equivalent F/number or F/number actually supplying the vidicon. This is the lens F/number modified by the relay and from basic geometrical optical theory is:

$$F_{noe} = F_{no} \frac{L_D}{L_c} \qquad \text{(A-27)}$$

If the sensor employs an automatic light level control which operates on vidicon target current, E will be accurately maintained. Therefore, Equation (A-25) applies as written for the level of E which is preset. For the silicon vidon under study, best performance is obtained when the level is about 0.1 lumens/ft^2. Equation (A-24) then becomes:

$$NEM = 4.64 \times 10^{-6} \quad \Delta f \qquad \text{(A-28)}$$

3. MRT CALCULATIONS

The following MRT equation modifications are required so that the computation may be performed in linear spatial frequency terms. First, in the NVL MRT equation, Δy must be replaced by the apparent detector size at the foveal lens image plane, i.e., it must be the Δh defined on Figure (A-2). As previously demonstrated in Equation (A-11).

$$\Delta h_y = a_y \frac{L_C}{L_D} \tag{A-29}$$

Also, in the MRT equation, it is best to compute the Q integral in terms of temporal frequency. This eliminates the velocity term in the MRT equation and makes the Q integral easier to compute. The Q integral is therefore

$$Q(f,\theta) = \int_o^\infty \frac{S(f)}{S(f_o)} H_N^2(f) H_w\left(\frac{f}{V_x}\right)^2 H_{Eye}\left(\frac{f}{V_x}\right) df \tag{A-30}$$

Of these terms, only H_w, the transfer function for a rectangular bar of width w, has not been defined. This transfer function is in linear rather than angular dimensions, i.e.,

$$H_w\left(\frac{f_x}{V_x}\right) = \text{Sinc}\left(W \frac{f_x}{V_x}\right) = \text{Sinc}\left(WS_x\right) \tag{A-31}$$

where

$$W \triangleq \frac{1}{2S_x} \tag{A-32}$$

The MRT equation written to show the dependency of two variables is

$$MRT(S_x,\theta) = \frac{SNR\pi^2 NE\Delta T}{4\sqrt{14}\ MTF_{TOTAL}(S_x,\theta)} \left[\frac{\Delta h_y\ S_x Q(f,\theta)}{\Delta f_N F_R\ t_e\ \eta_{OVSC}}\right]^{1/2} \tag{A-33}$$

This equation results in an MRT very weakly dependent on θ. To obtain the MRT for any field angle θ we convert the spatial frequency term S_x into an angular frequency term by using Equation (A-5) containing the focal length function:

$$f_\mu = S_x L(\theta) \tag{A-5}$$

Note this will be the angular spatial frequency in the scan direction (target bars normal to the scan direction). It could be related to f_x and f_y but this does not appear to be required at this point.

4. CONCLUSIONS

To conclude this effort, a block diagram of the NVL model converted to the VARVS Concept in the visual spectrum is shown in Figure A-3. This model was used in the study to compute Minimum Resolvable Modulation to predict performance.

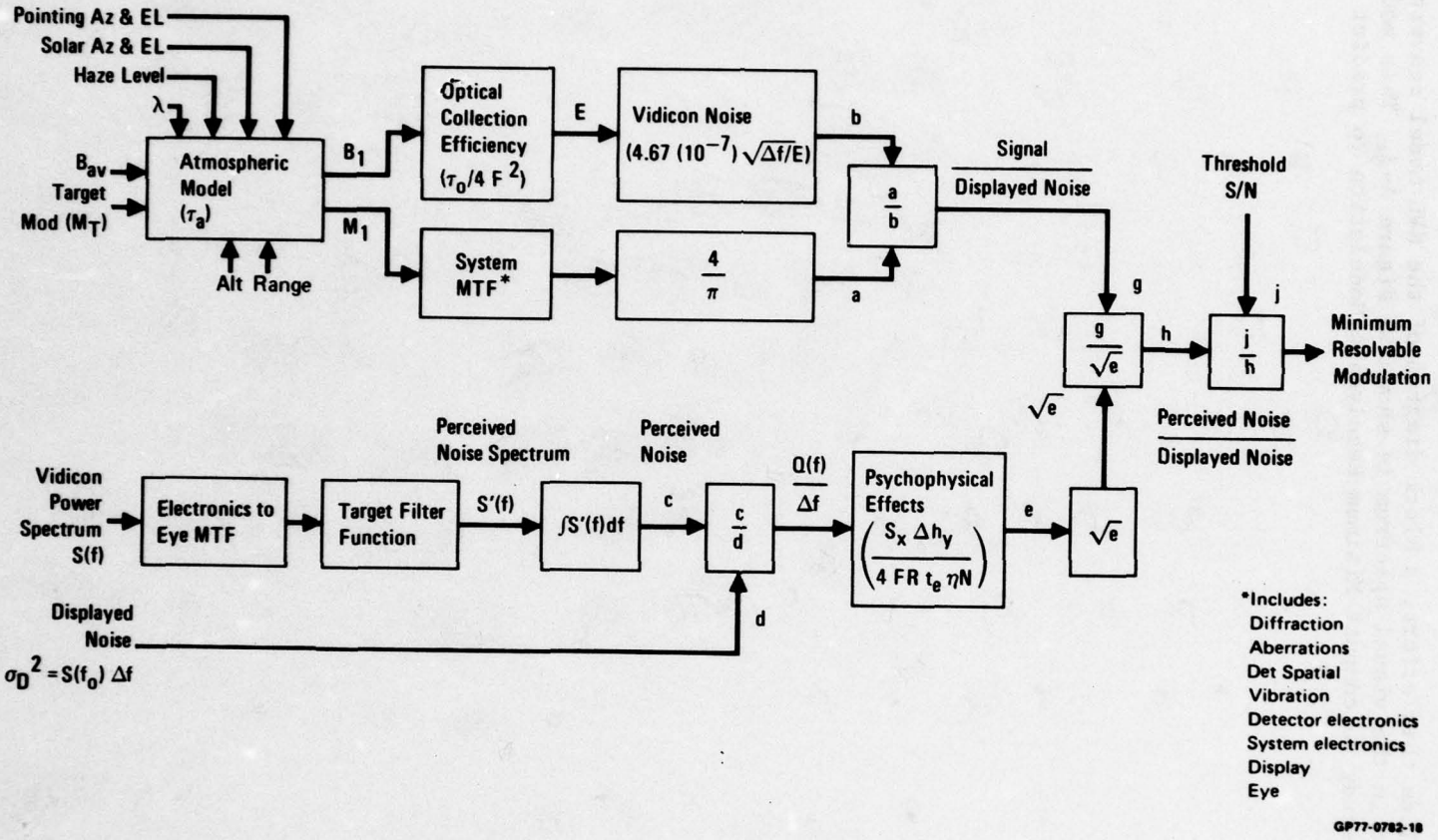

Figure A-3 NVL model adapted to VARVS for visual spectrum

APPENDIX B

LINEAR SENSOR ACQUISITION MODEL

The linear sensor acquisition model development was performed with IRAD funds and is included in this report for reference. The reader will find the model framework similar to that of the VARVS search model. The main differences lie in the linear sensor's relatively constant resolution over the field-of-view thus enabling the observer to make better use of his time by eliminating the need to slew the sensor for target identification.

This model was designed to evaluate the use of TV sensors for target acquisition and computes the probability of cue detection, target detection, recognition, and probability that the target is within the search area. The model requires input parameters defining the mission geometry, search area requirements and sensor and sensor system characteristics. The model assumes a cue oriented systematic search which is one where targets are found by first detecting a cue and then using the cue to search for a target. For example, a tank or personnel carrier may be located by finding a cluster of vehicles. The probability of detecting a cue or target has been modeled as an exponential as a function of resolution elements across the critical (smallest) dimension of the cue or target. The model allocates the time available for search so that the combination of tasks performed to acquire a target is optimized.

The main parameters controlling the search process are derived from the TV sensor's footprint which is a description of the ground resolution of the sensor referenced to the detector plane. The resolution measurement has units of line pairs per millimeter. Characterization of the footprint is accomplished by calculating system resolution at uniform increments (ΔA) on the detector face. An adaptation of the NVL model is used for this calculation. The quality of the footprint affects the methods and use of the footprint during search. The resolution will vary throughout the footprint which is a result of: 1) the slant range to each ΔA, 2) the image degradation due to the forward velocity of the aircraft, 3) atmosphere, and 4) viewing geometry.

The user may determine that parts of the display are unsuitable for his search. Examples of this include information displayed above the horizon, ground covered by sensor which has too long of a slant range so that target resolution is below the threshold, and other imagery which is below the resolution threshold due to image motion or masking problems. Thus, the user may decide to ignore portions of the display for reasons stated above or other reasons which become significant in particular applications. The net effect of ignoring parts of the display is to limit the "real" coverage of the sensor.

The size and shape of the real coverage of the sensor plays a major part in its dynamic search capabilities. As the size of the sensor's useable footprint is decreased, the demands of the dynamic characteristics of the sensor's servo and search process is increased. This suggests that a tradeoff exists for the optimum choice of the portion of the footprint used. This choice may vary with the specific mission parameters. An examination of the dynamic systematic search process will give some insight

into the necessary parameters to consider in this tradeoff. A typical linear sensor is shown in Figure B-1. The outer edges of the footprint are determined by the viewing geometry and sensor FOV. If the user determines that the lower portion of the footprint is to be used in search, the real coverage can be characterized by the length along the flight line X_p and the mean width $2Y_p$. In a systematic search, the sensor will typically be slewed in a snapshot fashion across the total search area. The term "snapshot" indicates that the sensor is slewed quickly to its destination and then held stationary while the user searches the display. This type of slewing is used to eliminate smearing on the detector due to the angular velocity of the sensor.

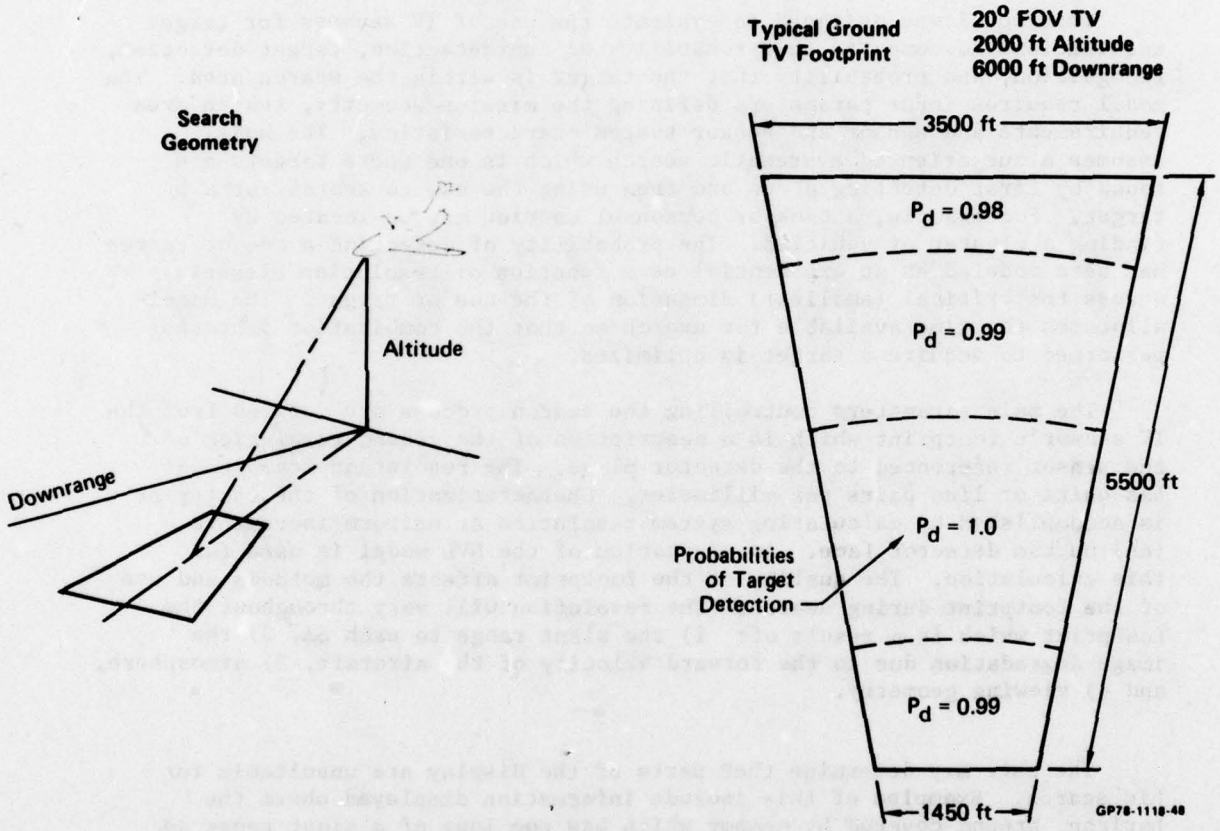

Figure B-1 Linear sensor search geometry

To assure full coverage, the footprints must fill the required lateral coverage $2Y_T$ during the time the sensor platform moves X_p along the flight line is illustrated in Figure B-2. The number of slews (n_{sl}) required to cover the required offset $2Y_T$ is defined as:

$$n_{sl} = [\frac{Y_T}{Y_p}] - 1 \qquad \text{(B-1)}$$

where [] indicates rounding up the next whole number. The time available (t_a) to find a particular target is calculated in terms of the sensor platform velocity (V_x),

$$t_a = \frac{X_p}{V_x} \tag{B-2}$$

The time it takes the sensor to move to the new position and settle to its steady state value will be called sensor slew time (t_{sl}). The amount of time the observer will spend "searching" during a particular "snapshot" is related to his glimpse rate. The time per glimpse (t_g) has been measured to be between 0.25 to 0.3 seconds.

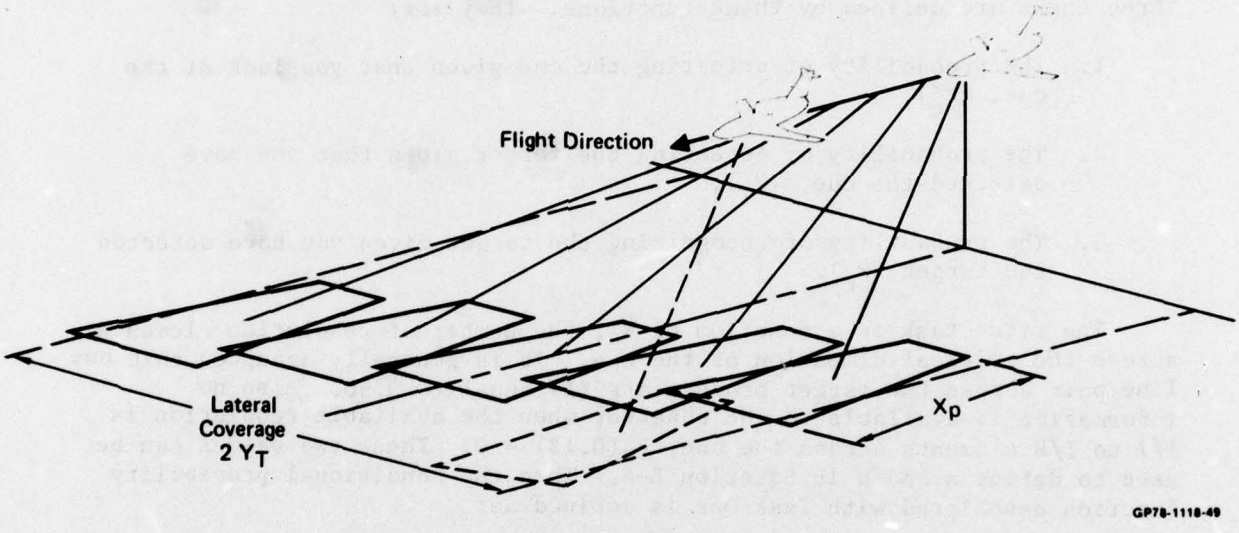

Figure B-2 Linear sensor snapshot geometry

The time (t_a') required for a complete swath of the acquisition process is:

$$t_a' = n_{sl} \, (t_{sl} + n_g \cdot t_g) \tag{B-3}$$

where n_g is the number of glimpses per slew and n_{sl} is the number of slews.

If the user is required to keep a constant nominal depression angle it is apparent that

$$t_a' \leq t_a$$

If $t_a' > t_a$, the user must be "tracking" the search area. This restriction brings to light a second tradeoff or optimization that must be made. The user may elect to spend more time searching each "snapshot" and not cover the total search width. This strategy becomes important when the total slew time ($n_{sl} \cdot t_{sl}$) becomes significant with respect to the pure search time, ($n_{sl} \cdot n_g \cdot t_g$).

The time allocation tradeoff and the footprint coverage compromise constitutes the basic mechanics of the model. The performance measure which determines how the two tradeoffs will be made is a function of conditional probability functions. These functions define the probabilistic description of the particular tasks in terms of the number of resolution elements across the critical dimension of the cue or target.

The probability functions are exponential of the general form

$$P(\gamma) = 1 - \exp\left[-(a\,\gamma + b)^2\right] \tag{B-4}$$

where γ = no. of resolution elements across the target
a,b = constants

Three tasks are defined by these functions. They are:

1. The probability of detecting the cue given that you look at the cue, (P_c'),

2. The probability of detecting the target given that you have detected the cue, (P_T),

3. The probability of recognizing the target given you have detected the target (P_r).

The first task is a function of N_c, the number of resolution elements across the critical dimension of the cue. It is generally accepted that one line pair across the target produce a $P_c'(1)$ equal to 0.90. Also no information is available to the observer when the available resolution is 1/7 to 1/8 elements across the cue, $P_c(0.13) = 0$. These two values can be used to define a and b in Equation B-4. Then the conditional probability function associated with Task One is defined as:

$$P_c'(N_c) = 1 - \exp\left[-(1.75 \cdot N_c - .23)^2\right] \tag{B-5}$$

Task two has a similar derivation and the only difference is that N_t, the number of resolution elements across the target is used for its argument. Thus:

$$P_T(N_t) = 1 - \exp\left[-(1.75\,N_t - .23)^2\right] \tag{B-6}$$

The probabilistic description of Task Three is taken directly from Bailey's paper (6) and is defined:

$$P_r(N_t) = 1 - \exp\left[-\left(\frac{N_t}{2} - 1\right)^2\right] \tag{B-7}$$

Equation B-5 defines the conditional probability of cue detection for one cue and one glimpse, and does not take into account the possibility of multiple glimpses.

The effect of multiple glimpses and multiple targets was studied in detail before deciding on the type of model to be used. The performance of the observer can best be analyzed by answering the question, "What is the probability of finding exactly K targets in n_g glimpses?". This question is usually associated with Bernoulli Trials.

$$P(K) = \binom{N}{K} p^K (1 - p)^{N-K} \tag{B-8}$$

where

$$\binom{N}{K} = \frac{N!}{(N-K)!\ K!}$$

In the multiple target acquisition case the probability of finding a cue is a function of the number of unfound cues in the display. Therefore as the observer detects cues, the probability of finding another cue changes. If the probability of finding a cue per glimpse is (P_c') for one cue contained within the display, then the probability (P(NT)) of finding a cue where multiple (NT) cues exist is:

$$P(NT) = 1 - (1 - P_c')^{NT} \tag{B-9}$$

Where NT is the number of independent cues contained within the display. As the observer detects and checks out possible cues, P(NT) decreases because the number of unfound cues is decreasing. Due to this non-stationary characteristic of P(NT), the expected number of cues E(NT) found during K glimpses cannot be calculated using compact methods such as Bernoulli trials (a form of the Binomial expansion). In the target acquisition application considered here, the probability density function defines the probability of finding K cues in n_g glimpses for constant n_g and all K such that K is whole number $0 \leq K \leq n_g$. Then one must determine all possible ways to detect K cues in n_g glimpses (all permutations), find the probability associated with each permutation and sum these probabilities. With the use of a digital computer and its memory capabilities this process may be somewhat simplified. Consider the state diagram in Figure B-3. The circles represents specific states as defined by the two axes, number of glimpses made (trials) and cues detected (successful results).

Each state has associated with it a probability of being in that state given the number of glimpses made. The probability of traveling from one state to another state is denoted by the flag on the arrow joining the two states. Each node defines the discrete probability density function of finding exactly K cues in n_g glimpses.

To determine the probability associated with any specific state, $P_c(n_g,K)$, one must determine all possible paths from (0,0) to the state in question. The probability of traveling down a specific path is the product of all the flags along that path. The summation of all possible probabilities associated with various path ways defines $P_c(n_g,K)$. The probability of being in state (0,0) is P(0,0)=1.

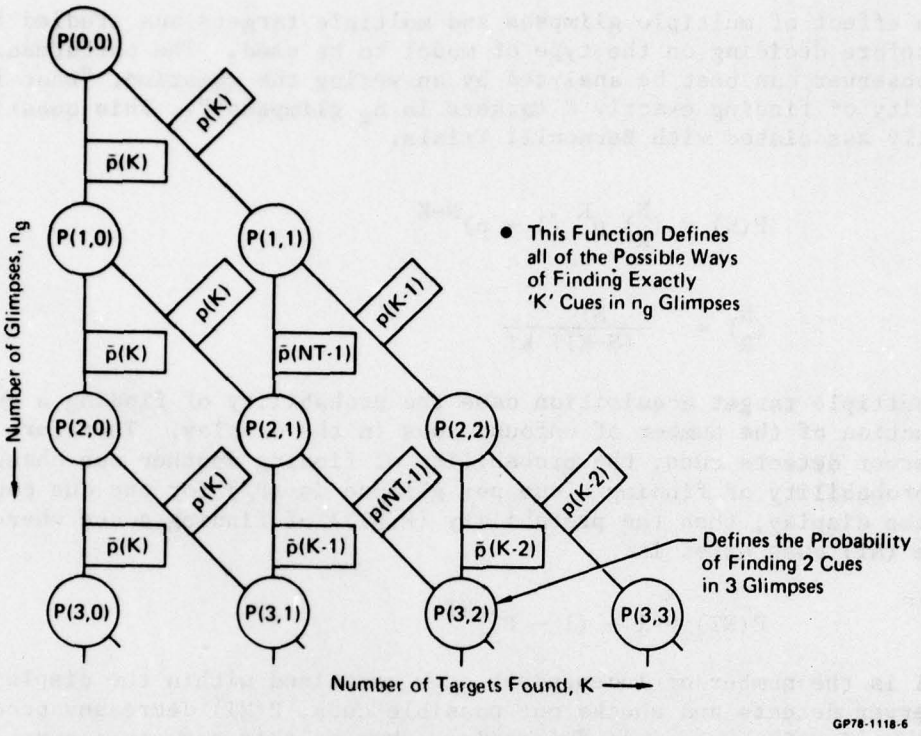

Figure B-3 Acquisition probability density function

The calculations required to generate the density distribution can be simplified if one makes the observation that each state $P_c(n_g,K)$ is a function of at most two previous states, for example:

$$P_c(3,2) = P_c(2,2) \cdot \bar{p}(NK - 2) + P_c(2,1) \cdot p(K-1) \qquad \text{(B-10)}$$

or

$$P_c(1,0) = P_c(0,0) \cdot \bar{p}(K)$$

Using a digital computer and saving the appropriate information, the trials matrix can be built up with a reasonable number of calculations.

The expected number $(E[K(n_g)]$ of possible cues found is by definition

$$E[K(n_g)] \triangleq \int_{-\infty}^{\infty} K\, P(n_g)dK \qquad \text{(B-11)}$$

or because of the discrete nature of this function.

$$E[K(n_g)] = \sum_{i=1}^{NG} i \cdot P(n_g,i) \qquad \text{(B-12)}$$

If all possible cues have equal probability of being the true cue, the probability of finding the right cue P_c is simply

$$P_c = \frac{E[K(n_g)]}{NT} \tag{B-13}$$

The number of glimpses the user is able to make is both a function of the average glimpse rate, the sensor slew time and the number of targets within the display on average, as shown in Equation B-3. The maximum number of glimpses the observer can make is:

$$N_g = t_a / t_g \tag{B-14}$$

The final probability (P_s) to be calculated is the probability that the cue (target) was at the same point in the search within the field of view. Assuming the probability of target location is uniform over the search area, P_s can be calculated:

$$P_s = \frac{\text{Area covered}}{\text{Total Search Area}} = \frac{A_c}{A_T} \tag{B-15}$$

The area covered (A_c) in an efficient systematic search is proportional to the total number of slews (N^T_{sl}) made:

$$A_c = N^T_{sl} \cdot A_{fp} \tag{B-16}$$

The term A_{fp} represents the area of the footprint. The total search area (A_T) is assumed to be a rectangle of length X_T along flight path and width $2Y_T$. The total area is:

$$A_T = 2 \cdot Y_T \cdot X_T \tag{B-17}$$

The number of slews the operator is able to make during the total search process is defined in terms of the platform velocity, search area length, and time taken per "snapshot" and is:

$$N^T_{sl} = \frac{X_T}{V_x \cdot (t_{sl} + n_g \cdot t_g)} \tag{B-18}$$

Substituting into Equation (B-15):

$$P_S = \frac{A_{fp}}{2\, V_x\, (t_{sl} + n_g\, t_g)\, Y_T} \tag{B-19}$$

Equation (B-19) shows that under the assumption made, systematic search with a constant depression angle, the length of the search area has no effect on the optimum search performance. In a specific mission with

constant n_g glimpses per slew, as Y_T increases P_s will decrease. This decrease in P_s may be offset by decreasing n_g thus increasing P_s, and decreasing the calculated value of P_c. The model adjusts these terms for best results. In light load situations, for example low aircraft velocity and "fast" slew time, the upper bound of Y_T may be the geometric crossrange capability of the sensor due to depression angle specifications, and not restricted by operator bandwidth.

A overview of the acquisition model's implementation is shown in the flow chart in Figure B-4.

The model's first task is to generate the sensor footprint. The user is required to designate the sensor's geometric location, velocity, atmospheric conditions, masking parameters and sensor field-of-view. Parameters defining the internal characteristics of the sensor are internal to the model and are adjusted by modifications to the actual program.

The next step is to define the portion of the footprint that is to be used in search. The model requests from the user the number of resolution elements across the cues to be used as a threshold for the augmented footprint choice. The augmented footprint is then characterized in terms of length, width, and average resolution. These characteristics are used to calculate the time available for search, the conditional probability of detecting the cue in a single glimpse (P_c'). The allocation of time for search and sensor slewing is adjusted for optimum search performance. Upon completion of this task the model calculates the conditional probabilities of target detection (P_t) and target recognition (P_r). The probabilities of mission success are evaluated in terms of the probability of detecting the target

$$P_{det} = P_c \cdot P_d \cdot P_s \tag{B-20}$$

and the probability of recognizing the target

$$P_t = P_{det} \cdot P_r \tag{B-21}$$

The probabilities of mission success are outputs for the users evaluation. The user may now elect to use these results of search, or select an alternate definition of the augmented footprint. The program calculates the optimum probabilities of target detection and recognition for a given mission geometry. It was recognized that a great deal of information can be reused to describe mission geometries varying only in depression angle. This concept has been implemented in the linear sensor model. The model is able to output predicted mission results for depression angles in degree increments over the total useful range of the sensor for very little increased computation cost.

To do this the actual computer model is broken up into two programs. The first generates the resolution capabilities for the indicated sensors over the total useful sensor range. The second exercises the search model and optimizations described.

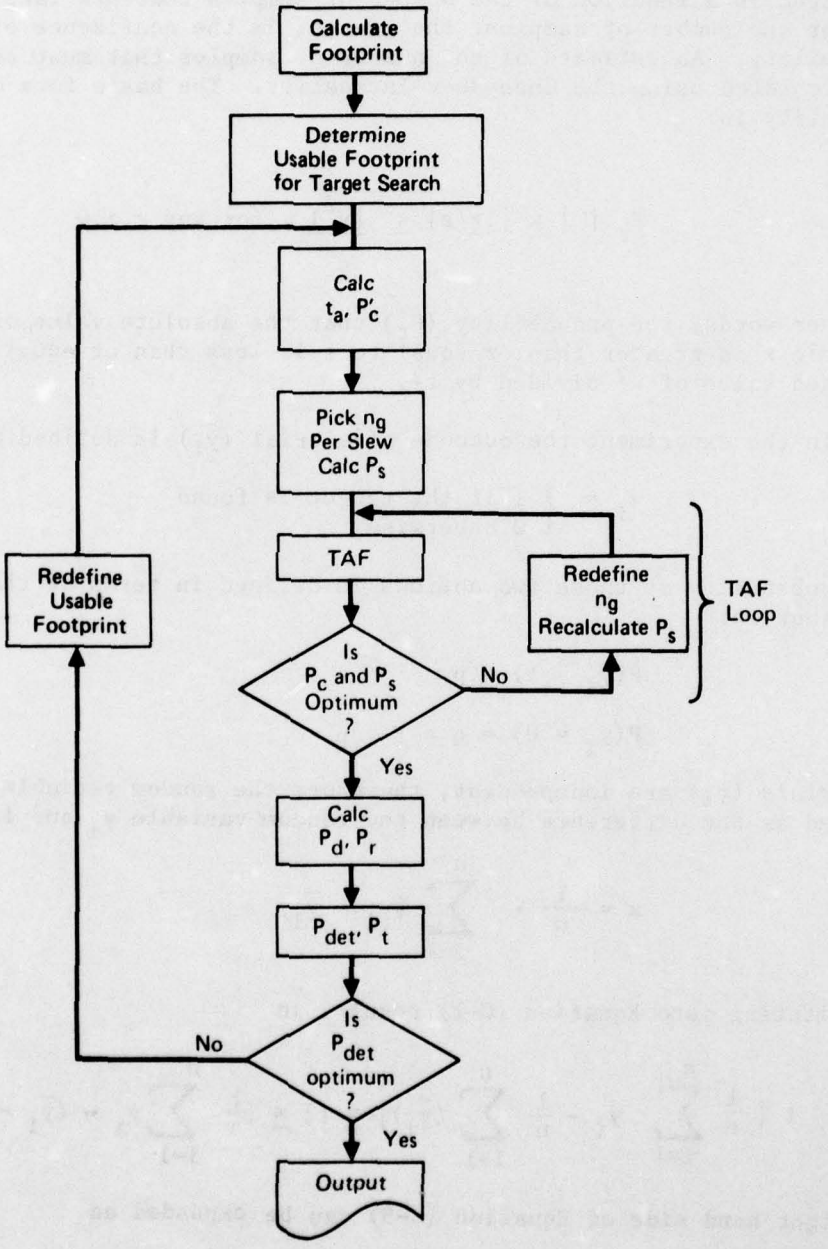

Figure B-4 Computer flow diagram for linear sensor target acquisition

APPENDIX C

THE EFFECT OF NUMBER OF MEASUREMENTS ON SAMPLE PROBABILITY ACCURACY

The accuracy with which the performance of an experiment can be predicted is a function of the number of samples that are taken. The greater the number of samples, the greater is the confidence of the computed probability. An estimate of the number of samples that must be taken can be calculated using the Chebyshev Inequality. The basic form of the inequality is:

$$P_r [| x | \geq \varepsilon] \leq \frac{\overline{[x^2]}}{\varepsilon^2} , \text{ for any } \varepsilon > 0 \qquad \text{(C-1)}$$

In other words, the probability (P_r) that the absolute value of the random variable x is greater than or equal to ε is less than or equal to the expected value of x^2 divided by ε^2.

In the experiment the outcome of a trial (y_i) is defined as:

$$y_i = \begin{cases} 1 \text{ if the target is found} \\ 0 \text{ otherwise} \end{cases} \qquad \text{(C-2)}$$

The probability of these two actions is defined in terms of the binominal distribution:

$$\text{and} \qquad P(y_i = 1) = p$$
$$P(y_i = 0) = q = 1 - p \qquad \text{(C-3)}$$

All trials (y_i) are independent, therefore the random variable x can be defined as the difference between the random variable y_i and its mean

$$x = \frac{1}{n} \cdot \sum_{i=1}^{n} [y_i - \bar{y}_i] \qquad \text{(C-4)}$$

Substituting into Equation (C-1) results in

$$P_r [| \frac{1}{n} \sum_{i=1}^{n} y_i - \frac{1}{n} \sum_{i=1}^{n} (\bar{y}_i) | \geq \varepsilon] \leq [\frac{1}{n} \sum_{i=1}^{n} y_i - (\bar{y}_i - (\bar{y}_i)]^2$$

The right hand side of Equation (C-5) can be expanded as

$$\frac{1}{nm} \sum_{i=1}^{n} \sum_{j=1}^{m} \overline{[y_i y_j - y_i(\bar{y}_j) - y_j(\bar{y}_i) + \bar{y}_i^2]} \qquad \text{(C-6)}$$

The average of any product where the subscripts are not the same is zero because all the y_i's are independent. This Equation (C-6) becomes

$$\frac{1}{n^2} \sum_{i=1}^{n} (\overline{y_i^2} - \overline{y}_i^2) \triangleq \sum_{i=1}^{n} \sigma_{y_i}^2 \tag{C-7}$$

Since all y_i are identically distributed:

$$\sum_{i=1}^{n} \sigma_{y_i}^2 = n \cdot \sigma_y^2 \tag{C-8}$$

The variance of a binomial distrubtion is:

$$\sigma_y^2 = p \cdot q \tag{C-9}$$

Substituting Equations (C-7) and (C-8) into (C-5) gives:

$$P_r [\, |x| \geq \varepsilon] \leq \frac{p \cdot q}{n \varepsilon^2} \tag{C-10}$$

If we define the left side of Equation (C-10) as γ we find that

$$\gamma \leq \frac{p \cdot q}{n \varepsilon^2} \tag{C-11}$$

Then by rearranging terms, the number of trials n is defined as

$$n \geq \frac{p \cdot q}{\gamma \cdot \varepsilon^2} = \frac{p(1 - p)}{\gamma \cdot \varepsilon^2} \tag{C-12}$$

Thus, the number of trials (n) is defined in terms of the probability of a successful mission (p), the tolerance of the measurement (ε) and the probability of being within the tolerance. Equation (C-11) is graphed on Figure 14 for two values of ε, the measurement tolerance. An interesting observation is that the number of trials required to predict Y increases to a maximum as the probability of $\overline{Y}$ (p) tends toward 0.5.

APPENDIX D

APPLICATION OF THE NIGHT VISION LABORATORY (NVL) THERMAL VIEWING SYSTEM STATIC PERFORMANCE MODEL TO THE IR VARVS

It was suggested that the NVL Thermal Viewing System Static Performance Model D-1 be used to evaluate the performance of the RVS. However, repeated attempts to convert the RVS parameters directly to the NVL model have led to the following problem. The radial distortion function of the foveal lens does not lend itself to an MTF analysis as a function of object field angular spatial frequency as called for in the NVL model. All parameters can be converted successfully except for the scan velocity term because a linear raster scan on the lens image plane will create a variable angular velocity and variable direction scan in the object field. This is depicted in Figure D-1. Extreme complexity results when attempts are made to convert spatial into temporal frequency. This is illustrated by the rotation of the f_x bar pattern in the lens image plane shown in Figure D-1. Given enough time, an analysis could be made in a manner compatible with the NVL model. However, the analysis is much simpler if performed, not in object field angular frequency (cycles/milliradian) but in spatial frequency terms (lines/millimeter). For our purpose of optimizing the RVS lens, it is simpler to work in terms of spatial frequency on the foveal lens focal plane.

This simplicity arises because seven of the nine MTF's are independent of object field angle at this foveal lens focal plane location, and the scan velocity is undirectional and uniform at this location, thereby making easy conversions from spatial to temporal parameters. The only non-linear conversions necessary are simple geometrical ones which translate from focal plane to object field and display space. The advantages of working in the spatial frequency terms will become clear as the analysis is developed. In the following development, the NVL model approach will be used precisely but will be applied in the foveal lens focal plane as a function of linear spatial frequency (1/mm). Parameters will be covered in the same order as they are in the NVL Report (4), which describes the model in detail.

1. MTF'S

a. Optical MTF

The optical MTF's consist of a diffraction MTF and a Gaussian MTF.

(1) Diffraction

In angular terms, the diffraction MTF is referenced as Equations (9) and (10) of the NVL report:

$$H_{opt}(f_x,\theta) = \frac{2}{\pi}\left[\cos^{-1} A - A(1 - A^2)^{1/2}\right] \qquad \text{(D-1)}$$

where $$A = \lambda F_{\#} f_x / L(\theta) \qquad \text{(D-2)}$$

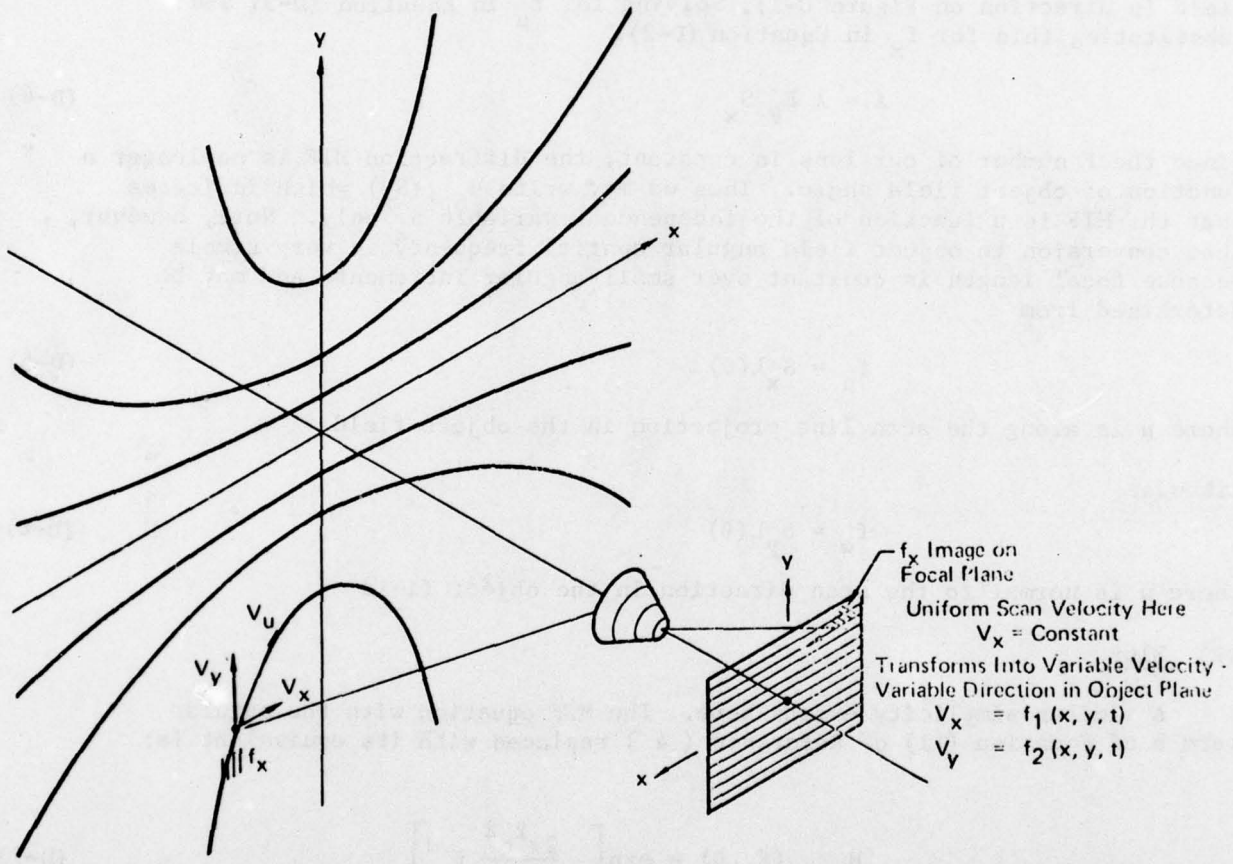

Figure D-1 Scan distortion introduced by foveal lens

GP76 0773 1

where L(θ) is the equivalent focal length which changes over a 50/1 range as object field angle θ changes. The angle θ is the absolute angle between the point of interest and the lens optical axis. At the foveal lens image plane

$$S_x = \frac{f_\mu}{L(\theta)} \tag{D-3}$$

where S_x is the image plane spatial frequency and f_μ is its object field angular equivalent measured along the scan line projection in the object field (μ direction on Figure D-1). Solving for f_μ in Equation (D-3) and substituting this for f_x in Equation (D-2).

$$A = \lambda F_{\#} S_x \tag{D-4}$$

Since the F number of our lens is constant, the diffraction MTF is no longer a function of object field angle. Thus we may write $H_{opt}(S_x)$ which indicates that the MTF is a function of the independent variable S_x only. Note, however, that conversion to object field angular spatial frequency is very simple because focal length is constant over small angular increments and may be determined from

$$f_\mu = S_x L(\theta) \tag{D-5}$$

where μ is along the scan line projection in the object field

likewise

$$f_w = S_y L(\theta) \tag{D-6}$$

where w is normal to the scan direction in the object field

(2) Blur

A similar simplicity exists here. The MTF equation with the angular term b of Equation (11) of Reference (4) replaced with its equivalent is:

$$H_{blur}(f_x, \theta) = \exp\left[-\frac{2\pi^2\sigma^2}{L(\theta)^2} f_x^2\right] \tag{D-7}$$

The foveal lens inherently has a constant spatial blur over its entire focal plane, so that the sigma (σ) of Equation (D-7) is a constant. Substituting Equation (D-5) into (D-7) we see the blur MTF simplifies to

$$H_{blur}(S_x) = \exp\left[-2\pi^2 \sigma^2 S_x^2\right] \tag{D-8}$$

Thus this MTF like the diffraction MTF, is no longer a function of object field angle because the focal length variable has been removed.

b. Detection MTF

The spatial filter MTF of the detector is defined as:

$$H_{Det}(f_x,\theta) = \frac{\mathrm{Sin}(\pi f_x \Delta x)}{\pi f_x \Delta x} \triangleq \mathrm{Sinc}(f_x \Delta x) \qquad \text{(D-9)}$$

It is also complex in our system because the angular projection of the detector into the object field (Δx) in this equation varies with absolute object field angle (θ). Since the detector height is still uniform at the lens focal plane, shown in Figure D-2 as Δh, Equation (D-9) can be restated as:

$$H_{Det}(S_x) = \frac{\mathrm{Sin}(\pi S_x \Delta h_x)}{\pi S_x \Delta h_x} \qquad \text{(D-10)}$$

Again the MTF becomes independent of object field angle. Note from Figure D-2 that the detector height (Δh_x) is a function of detector size(a), detector system focal length (L_D), and relay focal length (L_C), viz:

$$\Delta h_x \simeq a_x \frac{L_C}{L_D} \qquad \text{(D-11)}$$

There are two ways to arrive at the required L_C and L_D based upon whether the scanner or detector characteristics are known. If the scanner is available, horizontal FOV (θ_s) and instantaneous FOV (α) are known. Then the detector focal length is

$$L_D = \frac{a_x}{\alpha_x} = \frac{a_y}{\alpha_y} \qquad \text{(D-12)}$$

On the forward end of the scanner we must cover the foveal lens image plane height of $2h(\theta_{max})$ which subtends the angle θ_s. Thus,

$$\frac{h(\theta_{max})}{L_C} = \tan\frac{\theta_s}{2} \qquad \text{(D-13)}$$

Solving for L_C

$$L_C = \frac{h(\theta_{max})}{\tan \theta_s/2} \qquad \text{(D-14)}$$

If the detector characteristics are known, the focal lengths are a function of detector size (Δh) projected unto the image plane as shown in Figure D-2. Detector size Δh can be computed directly from either the on-axis resolution required, the number of scan lines required across the vertical FOV, or bandwidth/response restrictions and frame rate requirements. The focal lengths, L_C and L_D, are then selected to make the detector dimension appear as the required Δh at the foveal lens focal plane. The scanner horizontal FOV given by scanner mechanics must cover the total image plane height ($2h(\theta_{max})$). In either case the detector

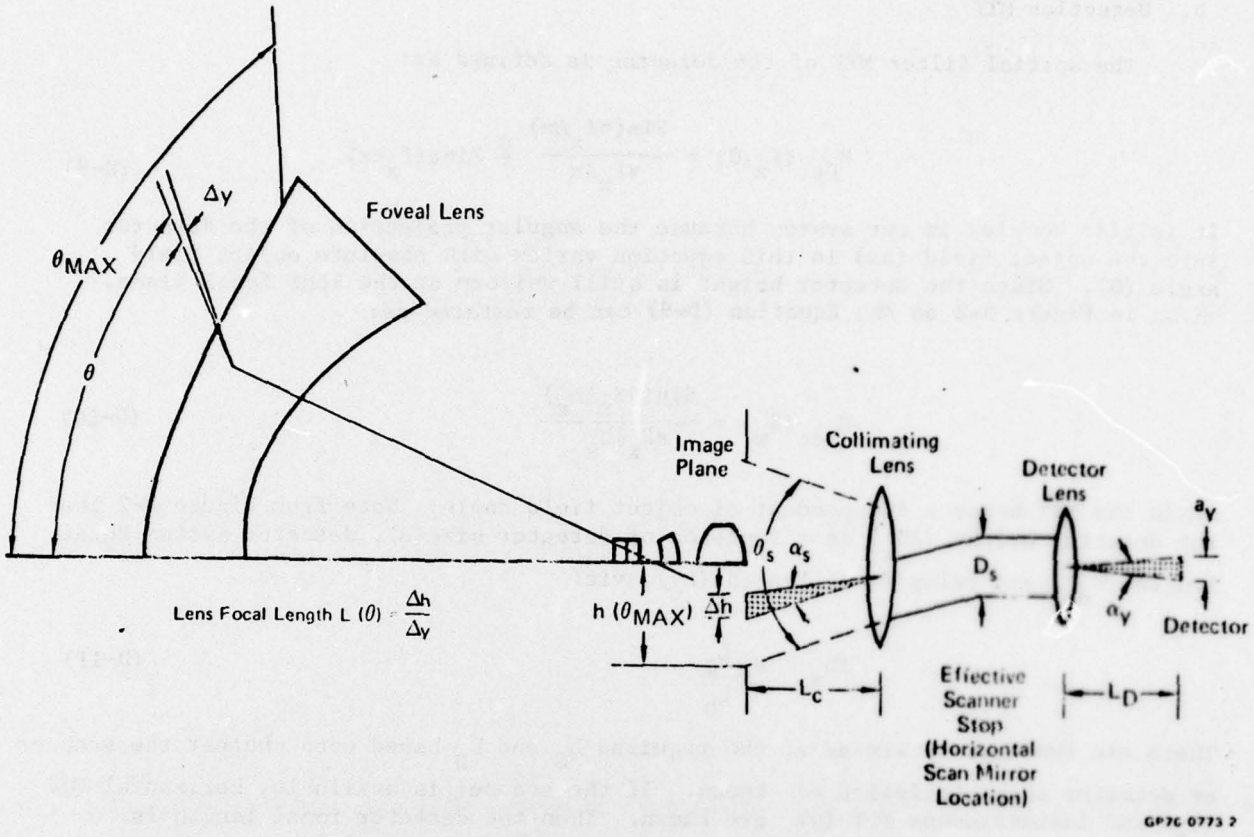

Figure D-2 Scanner resolution element geometry

MTF becomes:

$$H_{Det}(S_x) = \text{Sinc}\ \frac{a_x L_C}{S_x L_D} \qquad \text{(D-15)}$$

Again this MTF is independent of object field angle.

e. Detector Electronics MTF

It is in this MTF, the detector electrical response, that we get into real trouble trying to work in object field angular space. For a conventional linear optical system, a linear detector scan velocity converts into a scaled but linear angular scan in the object field. This is not true in our system as was shown in Figure D-1. A linear scan in the x direction on the image plane results in angular velocities in both θ_x and θ_y directions in the angular object field. Both of these angular components are non-linear functions of both x and y position on the image plane. Thus, converting from spatial frequency to temporal frequency becomes very complex.

All of this can be avoided by working in linear spatial plane terms. If the scanner has an angular scan velocity β, then the linear motion of the instantaneous FOV on the foveal lens image is

$$V_x = \beta L_C \tag{D-16}$$

The conversion to temporal frequency (f) is therefore

$$f = V_x S_x \tag{D-17}$$

This is a constant conversion and not a function of time. Therefore, all electronic MTF's of the NVL model are valid. These are

$$H'_{Det}(f)$$

$$H_{Elect}(f)$$

$$H_B(f)$$

d. Display

The RVS display is the inverse of the foveal lens, which results in a conventional linear raster generated on the CRT. The CRT has a constant spot size and the expansion optics has a constant blur at the object focal plane. Again this MTF, if derived in the linear spatial plane, will not be a function of object angle. If the optical blur and CRT spot size are combined and assumed to have a Gaussian MTF, a composite sigma (σ_d) results and the MTF is:

$$H_{Disp}(S_x) = \exp\left[-2\pi^2(r\sigma_d)^2 S_x^{\,2}\right] \tag{D-18}$$

where r is the physical ratio of format sizes; viz

$$r = \frac{H_{LENS\ IMAGE}}{H_{DISPLAY\ CRT}} \tag{D-19}$$

By contrast, if this were accomplished in the object angular plane, the MTF would be much more complex, viz

$$H_{Disp}(f_{x,0,M}) = \exp\left[-\frac{2\pi^2(r\sigma_d)^2 f_x^{\,2}}{L(\theta)^2 M^2}\right]$$

where M is any system angular magnification from object field to the viewer. Again the simplicity is obvious.

e. & f. Stabilization and Eyeball

The remaining two MTF's are the only two that are not simplified by working in linear spatial rather than angular terms. First, stabilization tends to be angular input to the system. Using the MTF from the NVL report:

$$H_{Los}(f_x) = \exp\ (-Pf_x^{\ 2}) \qquad \text{(D-20)}$$

Converting to the foveal lens image plane results in

$$H_{Los}(S_x, \theta) - \exp\left[-PS_x^{\ 2}L(\theta)^2\right] \qquad \text{(D-21)}$$

Similarly, the eye views the display in angular terms. The NVL MTF is

$$H_{Eye}(f_x) = \exp\left[-\frac{\Gamma f_x}{M}\right] \qquad \text{(D-22)}$$

Equation (D-22) must be converted to the foveal lens image plane

$$H_{Eye}(S_x, \theta) = \exp\left[-\frac{\Gamma S_x L(\theta)}{M}\right] \qquad \text{(D-23)}$$

In conclusion, seven MTF's have been simplified at the expense of two that have been made slightly more complex by the conversion to linear spatial frequency.

2. NEΔT

NEΔT can be used as defined in the NVL document since it is independent of spatial frequency, therefore no changes are required. However, it is a function of F number and a discussion is in order concerning which is the correct F number to use in the calculation. It is not simply the foveal lens F number or objective lens F number as stated in the NVL document. For NEΔT calculations, the F number must represent the actual ray cone supplying the detector.

In general our lens will be limited to a fixed image height $h(\theta_{max})$ that is based on fabrication considerations. The scanner must cover this total image in the most efficient manner. The optical geometry of the lens and scanner can be reduced to the basic arrangement shown in Figure D-3. On this figure the ray cone that supplies the detector is ϕ_4. Note that a maximum ray cone (ϕ_3) that the detector can utilize exists. Obviously, the best design would have $\phi_3=\phi_4$. This is not always possible, however, because the lens may be required to operate with available scanners. Therefore, it will be necessary to define both of these ray cones and utilize the smallest for NEΔT and diffraction MTF calculations. Before processing, note that ray cones may also be defined by F numbers as shown in Figure D-4.

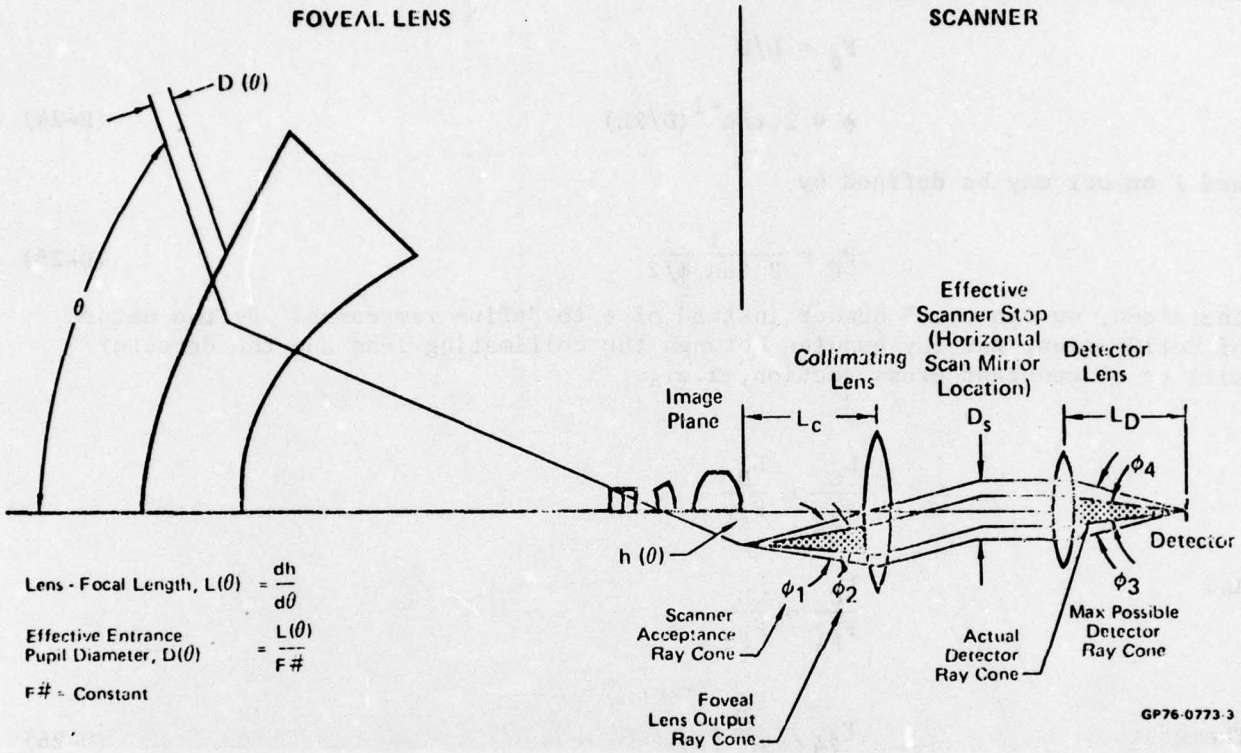

Figure D-3 General lens/scanner geometry

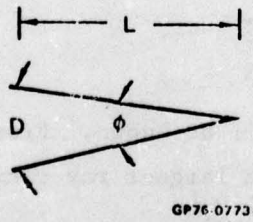

Figure D-4 Ray cone parameters

Since anywhere along the ray bundle

$$F_{\#} = L/D$$

$$\phi = 2 \tan^{-1}(D/2L) \qquad \text{(D-24)}$$

and F number may be defined by

$$F_{\#} = \frac{1}{2 \tan \phi/2} \qquad \text{(D-25)}$$

Therefore, we can use F number instead of ϕ to define ray cones. By the nature of collimation, the ray bundles between the collimating lens and the detector will be of constant cross section, i.e.,

$$\frac{L_C}{F_{\#2}} = \frac{L_D}{F_{\#4}}$$

And

$$\frac{L_C}{F_{\#1}} = \frac{L_D}{F_{\#3}}$$

Therefore

$$F_{\#4} = \frac{L_D}{L_C} F_{\#2} \qquad \text{(D-26)}$$

And

$$F_{\#3} = \frac{L_D}{L_C} F_{\#1} \qquad \text{(D-27)}$$

The larger of these two F numbers must be used for both diffraction and NEΔT calculations. Now note that $F_{\#2}$ is the F number of the foveal lens while $F_{\#1}$ is that generated by the scanner internal aperture stop (D_s) and we may write:

$$F_{\#1} = \frac{L_C}{D_S} \qquad \text{(D-28)}$$

For any particular scanner, D_s will be known. From Equation (D-27) the smallest F number which translates into the largest ray cone we can supply the detector with is:

$$F_{\#3} = \frac{L_D}{L_C} \frac{L_C}{D_s} = \frac{L_D}{D_s} \qquad \text{(D-29)}$$

which is also obvious from inspection.

For our ONR work, a scanner has been specified while for the USAF effort only a detector geometry is available. The following derivations will try to accommodate both arrangements. If the scanner is specified, D_s and L_D will be known. If L_D is not given it can be calculated from the scanner instantaneous FOV (α) and detector size (a) in the same plane. Then

$$L_D = \frac{a_y}{\alpha_y} \tag{D-30}$$

Also, if the scanner is specified, its maximum scan angle (θ_s) shown in Figure D-2, is known. Since the scanner must scan the entire image, θ_s must cover $2h(\theta_{max})$. Then

$$L_C = \frac{h(\theta_{max})}{\tan \frac{\theta_s}{2}} \tag{D-31}$$

It is now possible to compute $F_{\#4}$ from Equation (D-26).

$$F_{\#4} = \frac{a_y \tan \theta_s/2}{\alpha_y h(\theta_{max})} = F_{\#2} \tag{D-32}$$

where $F_{\#2}$ is the foveal lens F number. Remember, for the diffraction MTF and NEΔT calculations, we use the larger of $F_{\#4}$ or $F_{\#3}$.

If a scanner is not defined, one must be theorized. This can easily be accomplished by procedures outlined in Lloyd (8). Generally, scanning hardware (mirror, drum, etc.) are selected to accomplish a given scan angle θ_s (number of facets). Collimation lens focal length (L_C) can then be computed by Equation (D-31). From the required scan lines across the maximum image height $h(\theta_{max})$, the apparent detector size (Δh) at the image can be calculated. The angular instantaneous FOV of the scanner can be calculated as follows, using the on-axis geometry of Figure D-2:

$$\alpha_y = \frac{\Delta h}{L_C} \tag{D-33}$$

L_D can then be calculated by

$$L_D = \frac{a_y}{\alpha_y} \tag{D-34}$$

D_s can then be defined by matching the lens F number

$$D_s = \frac{L_C}{F_\#} \tag{D-35}$$

3. MRT CALCULATIONS

The following MRT equation modifications are required so that the computation may be performed in linear spatial frequency terms. First, in the NVL MRT equation, Δy must be replaced by the apparent detector size at the foveal lens image plane, i.e., it must be the Δh defined on Figure D-2. As previously demonstrated in Equation (D-11).

$$\Delta h_y = \theta_y \frac{L_C}{L_D} \tag{D-36}$$

Also, in the MRT equation, it is best to compute the Q integral in terms of temporal frequency. This eliminates the velocity term in the MRT equation and makes the Q integral easier to compute. The Q integral is therefore

$$Q(f,\theta) = \int_o^\infty \frac{S(f)}{S(f_o)} H_N^2(f) H_w\left(\frac{f}{V_x}\right)^2 H_{Eye}\left(\frac{f}{V_x}\right) df \tag{D-37}$$

Of these terms, only H_w, the transfer function for a rectangular bar of width w, has not been defined. This transfer function is in linear rather than angular dimensions, i.e.,

$$H_w\left(\frac{f_x}{V_x}\right) = \text{Sinc}\left(W \frac{f_x}{V_x}\right) = \text{Sinc}\left(WS_x\right) \tag{D-38}$$

where

$$W \triangleq \frac{1}{2S_x} \tag{D-39}$$

The MRT equation written to show the dependency of two variables is

$$MRT(S_x,\theta) = \frac{SNR\pi^2 NE\Delta T}{4\sqrt{14}\ MTF_{TOTAL}(S_x,\theta)} \left[\frac{\Delta h_y\ S_x Q(f,\theta)}{\Delta f_N F_R\ t_e\ \eta_{OVSC}}\right]^{1/2} \tag{D-40}$$

This equation results in an MRT very weakly dependent on θ. To obtain the MRT for any field angle θ we convert the spatial frequency term S_x into an angular frequency term by using Equation (D-5) containing the focal length function:

$$f_\mu \approx S_x L(\theta) \qquad \text{(D-5)}$$

Note this will be the angular spatial frequency in the scan direction (target bars normal to the scan direction). It could be related to f_x and f_y but this does not appear to be required at this point.

AD-A068 594 MCDONNELL AIRCRAFT CO ST LOUIS MO F/G 17/5
INFRARED NON-LINEAR LENS.(U)
DEC 78 R W FISHER, R D HELMICK, R A KUPFERER F33615-77-C-1113
UNCLASSIFIED AFAL-TR-78-204 NL

2 OF 2
AD
A068 594

END
DATE
FILMED
6-79
DDC

REFERENCES

1. 1979 Independent Research and Development, "Advanced Aircraft Reconnaissance Systems", Project Number 97470, McDonnell Aircraft Co., St. Louis, MO

2. Fisher, R.W., et al, Variable Acuity Display Development, Infrared Lens Feasibility Study, USAF (AFAL) TR 77-156, Vol. II, McDonnell Aircraft Co., St. Louis, MO, August 1977

3. 1977 Independent Research and Development, "Remote Viewing System", Project Number 77520, McDonnell Aircraft Co., St. Louis, MO

4. Ratches, James, et al, Night Vision Laboratory Static Performance Model For Thermal Viewing Systems, Army Electronics Cmd., Fort Monmouth, N.J., Report No. 7043, April 1975.

5. Johnson, J., "Analysis of Image-Forming Systems," Proceedings of the Image Intensified Symposium, U.S. Army Engineers Research and Development Laboratory, Fort Belvoir, Va., October 1958.

6. Bailey, H.H., "Target Detection Through Visual Recognition: A Quantitative Model and Two Applications", Journal of Defense Research, Vol. 3B, No. I, Spring 1971, p. 54

7. RCA, Inc., 4532A Camera Tube Specification Sheet, RCA Corp. Harrison, N.J., June 1973.

8. Lloyd, J.M., Thermal Imaging Systems, Plenum Press, New York 1975

*U.S.Government Printing Office: 1979 — 657-002/551